UNIVERSITY OF CALIFORNIA SAN DIEGO

On corticocortical connectivity and its contribution to extracranial potentials

A dissertation submitted in partial satisfaction of the requirements
for the degree Doctor of Philosophy

in

Neurosciences

with a specialization in Computational Neurosciences

by

Burke Quartman Rosen

Committee in charge:

Professor Eric Halgren, Chair
Professor Maxim Bazhenov
Professor Anders Dale
Professor Virginia De Sa
Professor Mingxiong Huang

2023

The Dissertation of Burke Quartman Rosen is approved, and it is acceptable in quality and form for publication on microfilm and electronically.

University of California San Diego

2023

DEDICATION

In memory of my father, who bound the same lightning with his hands that I observe in the brain and who first taught me how to troubleshoot a circuit.

EPIGRAPH

In addition to the long, better-delineated association bundles, there is an almost infinite number of shorter and very short association fibers.

- Elizabeth C. Crosby, Tryphena Humphrey, & Edward W. Lauer
Correlative Anatomy of the Nervous System, 1962

EEG could be a much more powerful and insightful brain measurement tool if only we could identify one-to-one mappings between EEG feature and neural microcircuit configuration.

- Michael X. Cohen
Trends in Neurosciences, 2017

The actual correlation of dipole strength as a function of distance on the cortical surface could be estimated by invasive recordings on animals or human patients.

- Anders M. Dale & Martin I. Sereno
Improved Localization of Cortical Activity by Combining EEG and MEG with MRI Cortical Surface Reconstruction: A Linear Approach. *Journal of Cognitive Neuroscience*, 1993

TABLE OF CONTENTS

LIST OF FIGURES

LIST OF TABLES

ACKNOWLEDGEMENTS

I would first like to acknowledge my advisor Eric Halgren, his for invaluable mentorship and guidance though all stages of the analyses and experiments reported in this dissertation. I wish to express particular gratitude for his dedication to rigor, his deep knowledge and appreciation of the full history of neuroscientific endeavor, and his indominable optimism. Rarely perhaps do the sundry idiosyncrasies of student and advisor so align and complement. We occupy tilted orbits.

I am grateful also for the many fruitful conversations, ideas, and contributions of my colleagues throughout my studies. I thank especially my fellow students Chris Gonzalez, Xi Jiang, Charly Dickey, Zarek Siegel, Jacob Garret, and Ilya Verzhbinsky for being indispensable sounding boards, strategists, and second pairs-of-eyes. We struggle and strive together. I thank my mentees for giving me the opportunity to pay froward, in modest measure, the sustained mentorship I have received in my career and particularly Sophie Kajfez for her hard work and contributions to this dissertation. I thank my graduate cohort-mates and partners for their support, friendship, compassion, and tolerance. You helped me grow.

I also acknowledge the people that who helped prepare me for this journey. I thank Petr Janata for first offering me an opportunity to do research, and Fred Barrett for first teaching me how to code. I thank Mark Goldman for impressing quantitative principles upon me and allowing me a small project of my own. And I especially express gratitude to Ksenija Marinkovic for providing me an excellent environment to mentor and be mentored and for first teaching me to write scientifically.

I am profoundly grateful for my parents, who always encouraged and nourished my curiosity, and who always supported my aspirations.

I would also like to thank the NIMH and Institute for Neural Computation predoctoral training program in cognitive neuroscience, the NINDS and neuroscience graduate training program, and the Kavli Institute for Brain and Mind for support.

Chapter 1, in full, is a reprint of the material as it appears in Rosen BQ, Halgren E. 2021. A whole-cortex probabilistic tractography connectome. *eNeuro*, 8 (1). The dissertation author was the primary investigator and author of this paper.

Chapter 2, in full, is a reprint of the material as it appears in Rosen BQ, Halgren E. 2022. An estimation of the absolute number of axons indicates that human cortical areas a sparsely connected. *PLOS Biol*, 20 (3) e3001575. The dissertation author was the primary investigator and author of this paper.

Chapter 3, in part, is a reprint of the material as it appears in Rosen BQ, Krishnan GP, Sanda P, Komarov M, Sejnowski TJ, Rulkov N, Ulbert I, Eross L, Madsen J, Devinsky O, Doyle W, Fabo D, Cash S, Bazhenov M, Halgren E. 2019. Simulating human sleep spindle MEG and EEG from ion channel and circuit level dynamics. *J. Neurosci. Methods*, 316 46-57. The dissertation author was the primary investigator and author of this paper. In addition, chapter 3, in part, contains unpublished material coauthored with Yuri Sokolov, Jean Erik Delonois, Oscar Gonzalez, Giri Krisnan, and Maksim Bazhenov. The dissertation author was the primary author of this chapter.

Chapter 4, in part, is currently being prepared for submission for publication of the material coauthored with Sophie Kajfez, Jacob Garret, Charles Dickey, Caleb Nerison, Brittany Stedelin, Ahmed Raslan, Sydney Cash, Kathryn Davis, Sandip Pati, Jorge Gonzalez-Martinez, Sharona Ben-Haim, Jerry Shih, and Eric Halgren. The dissertation author was the primary author of this chapter.

VITA

2006-10 Bachelor of Science, Neurobiology, Physiology, and Behavior, University of California Davis

2010-14 Staff Research Associate, University of California San Diego

2014-15 Research Specialist, San Diego State University

2015-23 Doctor of Philosophy, Neurosciences with a Specialization in Computational Neurosciences, University of California San Diego

PUBLICATIONS

Dickey CW, Verzhbinsky IA, Jiang X, Rosen BQ, Kajfez S, Ben-Haim S, Raslan AM, Eskandar EN, Gonzalez-Martinez J, Cash SS, Halgren E. 2022. J Neurosci 42 (42) 7931-7946.

Dickey CW, Verzhbinsky IA, Jiang X, Rosen BQ, Kajfez S, Stedelin B, Ben-Haim S, Raslan AM, Eskandar EN, Gonzalez-Martinez J, Cash SS, Halgren E. 2022. Proc Natl Acad Sci119 (28) e2107797119.

Chen Y, Rosen BQ, Sejnowski T. 2022. Dynamical differential covariance recovers directional network structure in multiscale neural systems. Proc Natl Acad Sci 119 (24) e2117234119.

Marinkovic K, Rosen BQ. 2022. Theta oscillatory dynamics of inhibitory control, error processing, and post-error adjustments: Neural underpinnings and alcohol-induced dysregulation. Alcohol Clin Exp Res 46 (7), 1220-1232.

Rosen BQ, Halgren E. 2022. An estimation of the absolute number of axons indicates that human cortical areas a sparsely connected. PLOS Biol 20 (3) e3001575.

Dickey CW, Verzhbinsky IA, Jiang X, Rosen BQ, Kajfez S, Pati S, Halgren E. 2022. Cortico-cortical and hippocampo-cortical co-rippling are facilitated by thalamo-cortical spindles and upstates, but not by thalamic ripples. BioRxiv.

Peterson EJ, Rosen BQ, Belger A, Voytek B, Campbell AM. 2021. Aperiodic neural activity is a better predictor of schizophrenia than neural oscillations. bioRxiv.

Happer JP, Wagner LC, Beaton LE, Rosen BQ, Marinkovic K. 2021. The "when" and "where" of the interplay between attentional capture and response inhibition during a Go/NoGo variant. NeuroImage 231 117837.

Correas A, Cuesta P, Rosen BQ, Maestu F, Marinkovic K. 2021. Compensatory neuroadaptation to binge drinking: Human evidence for allostasis. Addict Biol 26 (3) e12960.

You Y, Correas A, Keehn RJJ, Wagner LC, Rosen BQ, Beaton LE, Gao Y, Brocklehurst WT, Fishman I, Müller R-A, Marinkovic K. 2021. MEG Theta during Lexico-Semantic and Executive Processing Is Altered in High-Functioning Adolescents with Autism. Cereb Cortex 31 (2) 1116-1130.

Rosen BQ, Halgren E. 2021. A whole-cortex probabilistic tractography connectome. eNeuro 8 (1).

Rosen BQ, Krishnan GP, Sanda P, Komarov M, Sejnowski TJ, Rulkov N, Ulbert I, Eross L, Madsen J, Devinsky O, Doyle W, Fabo D, Cash S, Bazhenov M, Halgren E. 2019. Simulating human sleep spindle MEG and EEG from ion channel and circuit level dynamics. J Neurosci Methods 316 46-57.

Marinkovic K, Beaton LE, Rosen BQ, Happer JP, Wagner LC. 2019. Disruption of frontal lobe neural synchrony during cognitive control by alcohol intoxication. JoVE e58839.

Gonzalez CE, Mak-McCully RA, Rosen BQ, Cash SS, Chauvel PY, Bastuji H, Rey M, Halgren E. 2018. Theta bursts precede, and spindles follow, cortical and thalamic downstates in human NREM sleep. J Neurosci 38 (46) 9989-10001.

Krishnan GP, Rosen BQ, Chen J-Y, Muller L, Sejnowski TJ, Cash S, Halgren E, Bazhenov M. 2018. Thalamocortical and intracortical laminar connectivity determines sleep spindle properties. PLOS Comput Biol 14 (6) e1006171.

Rosen BQ, Padovan N, Marinkovic K. 2016. Alcohol hits you when it is hard: Intoxication, task difficulty, and theta brain oscillations. Alcohol Clin Exp Res 40 (4), 743-752.

Mak-McCully RA, Rosen BQ, Rolland M, Regis J, Bartolomei F, Rey M, Chauvel P, Cash SS, Halgren E. 2015. Distribution, amplitude, incidence, co-occurrence, and propagation of human K-complexes in focal transcortical recordings. eNeuro, 2 (4).

Mak-McCully RA, Deiss SR, Rosen BQ, Ki-Young J, Sejnowski TJ, Bastuji H, Rey M, Cash SS, Bazhenov M, Halgren E. 2014. Synchronization of isolated downstates (K-complexes) may be caused by cortically-induced disruption of thalamic spindling. PLOS Comput Biol 10 (9) e1003855.

Marinkovic K, Rosen BQ, Cox B, Halger DJ. 2014. Spatio-temporal processing of words and nonwords: Hemispheric laterality and acute alcohol intoxication. Brain Res 1558 18-32.

Rosen BQ, O'Hara R, Kovacevic S, Schulman A, Padovan N Marinkovic K. 2014. Oscillatory spatial profile of alcohol's effects on the resting state: Anatomically-constrained MEG. Alcohol 48 (2), 89-97.

Marinkovic K, Rosen BQ, Cox B, Kovacevic S. 2012. Event-related theta power during lexical-semantic retrieval and decision conflict is modulated by alcohol intoxication: anatomically constrained MEG. Front Psychol 3 121.

FIELDS OF STUDY

Major Field: Neurosciences
Specialization: Computational Neurosciences

ABSTRACT OF THE DISSERTATION

On corticocortical connectivity and its contribution to extracranial potentials

by

Burke Quartman Rosen

Doctor of Philosophy in Neurosciences with a Specialization in Computational Neurosciences

University of California San Diego, 2023

Professor Eric Halgren, Chair

Although rarely quantitatively considered together, extracranially recorded electric potentials, or their complementary magnetic gradients, and the underlying neuronal transmembrane ion flows form a unitary phenomenon. Because the conduction of these fields through the tissues of the head are for all biologically relevant intents and purposes instantaneous and additive, the variance and covariance of signals recorded by extracranial sensors are a weighted linear combination of the variance and covariance of current density fluctuations in the gray matter of the cortex. However, for a given sensor variance-covariance matrix, or complex cross-spectral matrix in the frequency domain, there are infinite number of valid cortical source configurations. In order to accurately distinguish between these possibilities assumptions must be made about the true patterns of correlativity, or functional connectivity,

among sources which is in turn constrained by the anatomical connectivity of the cortex. In this dissertation, I investigated the structural and functional connectivity of the human cortex and developed computational models informed by these measures that quantitatively link intra- and extra-cranial activity.

Chapter 1 examines relative human corticocortical structural connectivity using publicly available diffusion MRI data from the human connectome project. Chapter 2 refines these results by scaling relative connectivity in arbitrary units to absolute connectivity in physical units by taking advantage of the unique properties of the corpus callosum, and in which we find finds that the resulting connectivity is sparse. In chapter 3 the anatomical connectivity is used to inform a whole brain model of non-REM sleep capable of producing synthetic intra- and extra-cranial sensor activity, and in Chapter 4 the composited human invasive stereo-EEG data from epilepsy patients to estimate the spatial dependence of spontaneous cortical functional connectivity in a frequency-resolved manner.

CHAPTER 1: A WHOLE-CORTEX PROBABILISTIC DIFFUSION TRACTOGRAPHY CONNECTOME

Abstract

The WU-Minn Human Connectome Project (HCP) is a publicly-available dataset containing state-of-art structural, functional, and diffusion-MRI for over a thousand healthy subjects. While the planned scope of the HCP included an anatomical connectome, resting-state functional-MRI forms the bulk of the HCP's current connectomic output. We address this by presenting a full-cortex connectome derived from probabilistic diffusion tractography and organized into the HCP-MMP1.0 atlas. Probabilistic methods and large sample sizes are preferable for whole-connectome mapping as they increase the fidelity of traced low-probability connections. We find that overall, connection strengths are lognormally distributed and decay exponentially with tract length, that connectivity reasonably matches macaque histological tracing in homologous areas, that contralateral homologs and left-lateralized language areas are hyperconnected, and that hierarchical similarity influences connectivity. We compare the diffusion-MRI connectome to existing resting-state fMRI and cortico-cortico evoked potential connectivity matrices and find that it is more similar to the latter. This work helps fulfill the promise of the HCP and will make possible comparisons between the underlying structural connectome and functional connectomes of various modalities, brain states, and clinical conditions.

Introduction

In the 21st century, advances in computation, theory, and neuroimaging have spurred a broad and intense interest in the anatomical connections and physiological correlations among human brain areas. Bivariate functional connectivity has given way to full functional connectomes, the most comprehensive of which may be the WU-Minn Human Connectome Project's (HCP) resting-state fMRI dense connectome (Van Essen et al., 2013). The planned

scope of WU-Minn HCP also included a full anatomical connectome (Van Essen and Ugurbil, 2017), and the project has collected, curated, and preprocessed diffusion imaging (dMRI) data for 1,065 subjects. However, a structural connectome has to-date not been released for these data. This report seeks to address this omission by presenting a full-cortex anatomical connectome derived from local, probabilistic tractography.

dMRI techniques detect white matter by registering the orientation biases of water molecule diffusion within myelinated axons. The majority of dMRI studies focus on differences in specific connections between treatment groups. In contrast, we seek here to present a robust, densely populated average connectivity matrix for the entire cortex using data from a large, healthy sample. Local dMRI fiber tract tracing algorithms can be broadly organized into two classes: deterministic e.g. dsi-studio (Yeh et al., 2013), and probabilistic e.g. probtrackX (Behrens et al., 2007). Deterministic tractography considers the most likely orientation at each voxel yielding the maximum likelihood tracts whereas probabilistic tractography considers the entire distribution of possible orientations, yielding a probability cloud of connections. As our goal is instead to explore all possible connections between regions, we employed local, probabilistic tractography (Behrens et al., 2007). This method has been validated against macaque retrograde tracers within-species (Donahue et al., 2016) and the dMRI protocol and equipment used for the WU-Minn HCP database were optimized in anticipation of this analysis (Sotiropoulos et al., 2013).

The physiological relevance of a connectome is maximized if its nodes form functionally distinct areas. Within the scope of cortex, this amounts to selecting a parcellation scheme. The HCP multi-modal parcellation (HCP-MMP1.0) (Glasser et al., 2016) has several advantages: it's boundaries are both functionally and anatomically guided, it has sufficient parcels (360) to generate a rich connectome while few enough that the parcels' extents comfortably exceed the dMRI voxel size, and mechanisms exist (Fischl et al., 2004) for it to be readily applied to individuals. Most importantly, the HCP-MMP1.0 parcellation is publicly available and widely

adopted, facilitating the comparison of the generated matrices to other structural and functional connectomes.

Given the computational intensity of dMRI fiber tractography and the field's inclination towards elucidating specific connections, it is not surprising that the number of existing publicly available dMRI datasets exceeds that of finished, readily applicable connectivity matrices. However, there do exist some prior examples. The USC Multimodal connectivity database (http://umcd.humanconnectomeproject.org), contains two dMRI tractography connectomes with standard surface-based parcellations: Hagmann (Hagmann et al., 2008) and ICBM (Mori et al., 2008), with sample-sizes of 5 and 138, respectively. A third is available at http://www.dutchconnectomelab.nl which contains 114 controls. All of these use the Desikan-Killiany atlas (Desikan et al., 2006) which consists of 68 cortical parcels and were produced with deterministic tractography. An atlas of major fiber tracts for the HCP 1200 cohort has recently released at http://brain.labsolver.org, (Yeh et al., 2018). However, this deterministic tractography connectome is spatially coarse, consisting of only 54 cortical parcels, and lacks dynamic range and statistical dispersion, as weaker connections are unrepresented, rendering the connectivity matrix nearly binary. The HCP-MMP1.0 atlas employed here has more than five times as many parcels while retaining the functional distinctness of areas. In contrast to the relatively sparse existing deterministic matrices, the probabilistic approach may better resolve weak or low probability connections leading to densely populated connectivity matrices like those found non-human primate tracing studies (Markov et al., 2014). Furthermore, the cohort studied is large and many other types of data are available for the same individuals including the NIH neuropsychological toolbox (Gershon et al., 2013), as well as fMRI and MEG data for resting-state and cognitive tasks, permitting within-cohort comparison to functional connectivity.

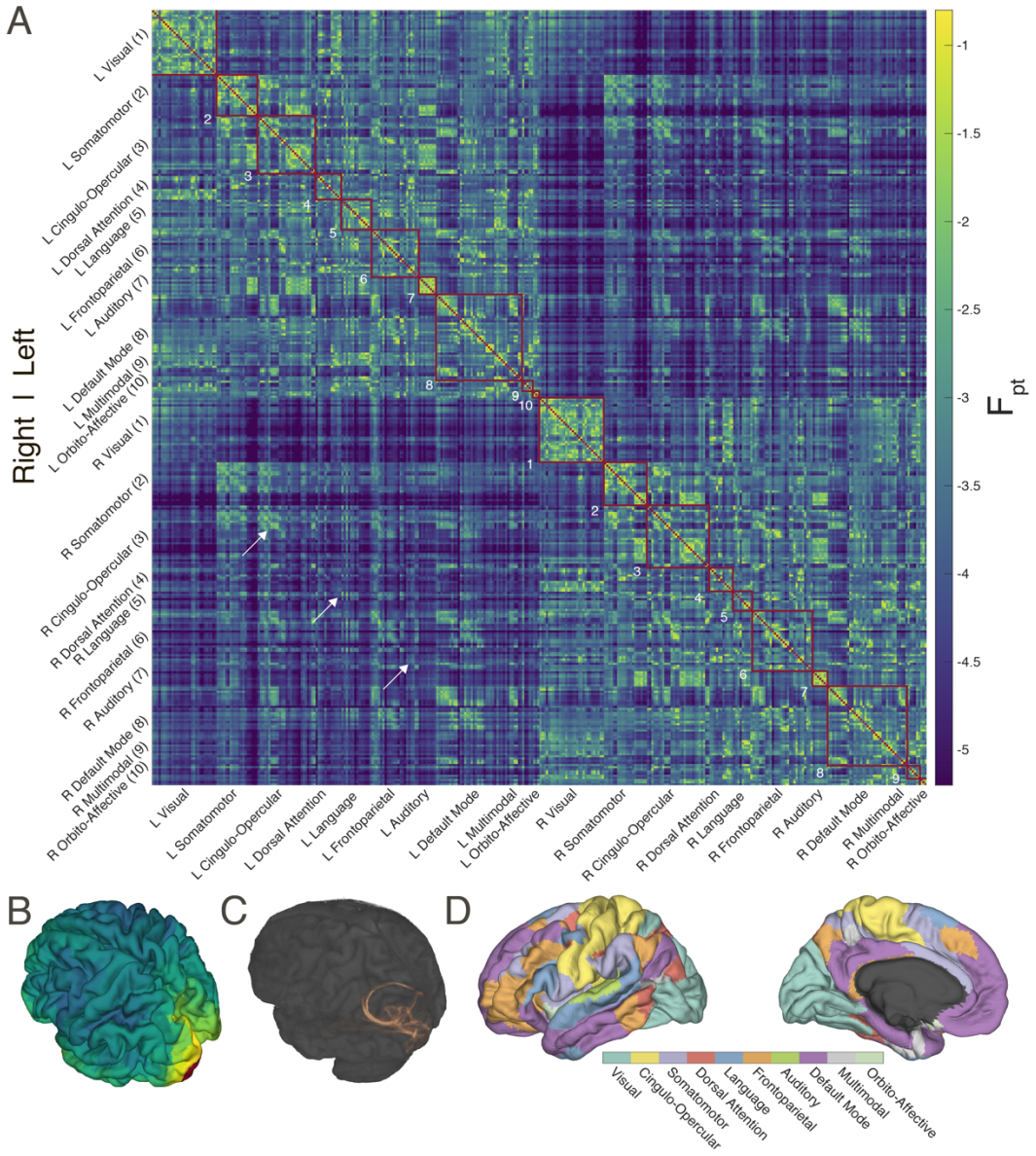

Figure 1.1 Probabilistic diffusion tractography structural connectome of the human cortex. (A) Group average (N = 1065) structural connectivity matrix consisting of the 360 HCP-MMPS1.0 atlas parcels organized into ten functional networks. Raw streamline counts are fractionally scaled yielding the log probability Fpt. The white arrows highlight the diagonal which contains contralateral homologs. (B) The first row of the connectivity matrix, showing connection probabilities from left V1 to all other parcels, projected onto the fsaverage template cortex. (C) Single subject (100307) volume ray casting visualization of left V1-originating streamline probabilities within the skull-stripped T1-weighted structural MR volume. (D) Ten functional networks, adapted from (Ji et al., 2019), within HCP-MMPS1.0 atlas. These are indicated by red boxes in panel A.

Table 1.1. Parcel order and network assignment. The emboldened indices refer to the parcel order in Figure 1A. The Orig. indices refer to the original parcel order presented in (Glasser et al., 2016). All indices refer to the left hemisphere, adding 180 yields the homologous right hemisphere indices.

Idx.	Parcel	Orig.	Network	Idx.	Parcel	Orig.	Network	Idx.	Parcel	Orig.	Network
1	V1	1	Cingulo-Opercular	**61**	46	84	Cingulo-Opercular	**121**	IP1	145	Frontoparietal
2	ProS	121	Visual	**62**	9-46d	86	Cingulo-Opercular	**122**	PFm	149	Frontoparietal
3	DVT	142	Visual	**63**	43	99	Cingulo-Opercular	**123**	p10p	170	Frontoparietal
4	MST	2	Visual	**64**	PFcm	105	Cingulo-Opercular	**124**	p47r	171	Frontoparietal
5	V6	3	Visual	**65**	Pol2	106	Cingulo-Opercular	**125**	A1	24	Auditory
6	V2	4	Visual	**66**	FOP4	108	Cingulo-Opercular	**126**	52	103	Auditory
7	V3	5	Visual	**67**	MI	109	Cingulo-Opercular	**127**	RI	104	Auditory
8	V4	6	Visual	**68**	FOP1	113	Cingulo-Opercular	**128**	TA2	107	Auditory
9	V8	7	Visual	**69**	FOP3	114	Cingulo-Opercular	**129**	PBelt	124	Auditory
10	V3A	13	Visual	**70**	PFop	147	Cingulo-Opercular	**130**	MBelt	173	Auditory
11	V7	16	Visual	**71**	PF	148	Cingulo-Opercular	**131**	LBelt	174	Auditory
12	IPS1	17	Visual	**72**	Pol1	167	Cingulo-Opercular	**132**	A4	175	Auditory
13	FFC	18	Visual	**73**	FOP5	169	Cingulo-Opercular	**133**	7m	30	Default Mode
14	V3B	19	Visual	**74**	PI	178	Cingulo-Opercular	**134**	POS1	31	Default Mode
15	LO1	20	Visual	**75**	a32pr	179	Cingulo-Opercular	**135**	23d	32	Default Mode
16	LO2	21	Visual	**76**	p24	180	Cingulo-Opercular	**136**	v23ab	33	Default Mode
17	PIT	22	Visual	**77**	PEF	11	Dorsal Attention	**137**	d23ab	34	Default Mode
18	MT	23	Visual	**78**	7PL	46	Dorsal Attention	**138**	31pv	35	Default Mode
19	LIPv	48	Visual	**79**	MIP	50	Dorsal Attention	**139**	a24	61	Default Mode
20	VIP	49	Visual	**80**	LIPd	95	Dorsal Attention	**140**	d32	62	Default Mode
21	PH	138	Visual	**81**	6a	96	Dorsal Attention	**141**	p32	64	Default Mode
22	V6A	152	Visual	**82**	PFt	116	Dorsal Attention	**142**	10r	65	Default Mode
23	VMV1	153	Visual	**83**	AIP	117	Dorsal Attention	**143**	47m	66	Default Mode
24	VMV3	154	Visual	**84**	PHA3	127	Dorsal Attention	**144**	8Av	67	Default Mode
25	V4t	156	Visual	**85**	TE2p	136	Dorsal Attention	**145**	8Ad	68	Default Mode
26	FST	157	Visual	**86**	PHT	137	Dorsal Attention	**146**	9m	69	Default Mode
27	V3CD	158	Visual	**87**	PGp	143	Dorsal Attention	**147**	8BL	70	Default Mode
28	LO3	159	Visual	**88**	IP0	146	Dorsal Attention	**148**	9p	71	Default Mode
29	VMV2	160	Visual	**89**	55b	12	Language	**149**	10d	72	Default Mode
30	VVC	163	Visual	**90**	PSL	25	Language	**150**	47l	76	Default Mode
31	4	8	Somatomotor	**91**	SFL	26	Language	**151**	9a	87	Default Mode
32	3b	9	Somatomotor	**92**	STV	28	Language	**152**	10v	88	Default Mode
33	5m	36	Somatomotor	**93**	44	74	Language	**153**	10pp	90	Default Mode
34	5L	39	Somatomotor	**94**	45	75	Language	**154**	OFC	93	Default Mode
35	24dd	40	Somatomotor	**95**	IFJa	79	Language	**155**	47s	94	Default Mode
36	24dv	41	Somatomotor	**96**	IFSp	81	Language	**156**	EC	118	Default Mode
37	7AL	42	Somatomotor	**97**	STGa	123	Language	**157**	PreS	119	Default Mode
38	7PC	47	Somatomotor	**98**	A5	125	Language	**158**	H	120	Default Mode
39	1	51	Somatomotor	**99**	STSda	128	Language	**159**	PHA1	126	Default Mode
40	2	52	Somatomotor	**100**	STSdp	129	Language	**160**	STSvp	130	Default Mode
41	3a	53	Somatomotor	**101**	TPOJ1	139	Language	**161**	TGd	131	Default Mode
42	6d	54	Somatomotor	**102**	TGv	172	Language	**162**	TE1a	132	Default Mode
43	6mp	55	Somatomotor	**103**	RSC	14	Frontoparietal	**163**	TE2a	134	Default Mode
44	6v	56	Somatomotor	**104**	POS2	15	Frontoparietal	**164**	PGi	150	Default Mode
45	OP4	100	Somatomotor	**105**	7Pm	29	Frontoparietal	**165**	PGs	151	Default Mode
46	OP1	101	Somatomotor	**106**	8BM	63	Frontoparietal	**166**	PHA2	155	Default Mode
47	OP2-3	102	Somatomotor	**107**	8C	73	Frontoparietal	**167**	31pd	161	Default Mode
48	FOP2	115	Somatomotor	**108**	a47r	77	Frontoparietal	**168**	31a	162	Default Mode
49	Ig	168	Somatomotor	**109**	IFJp	80	Frontoparietal	**169**	25	164	Default Mode
50	FEF	10	Cingulo-Opercular	**110**	IFSa	82	Frontoparietal	**170**	s32	165	Default Mode
51	5mv	37	Cingulo-Opercular	**111**	p9-46v	83	Frontoparietal	**171**	STSva	176	Default Mode
52	23c	38	Cingulo-Opercular	**112**	a9-46v	85	Frontoparietal	**172**	TE1m	177	Default Mode
53	SCEF	43	Cingulo-Opercular	**113**	a10p	89	Frontoparietal	**173**	PCV	27	Multimodal
54	6ma	44	Cingulo-Opercular	**114**	11l	91	Frontoparietal	**174**	TPOJ2	140	Multimodal
55	7Am	45	Cingulo-Opercular	**115**	13l	92	Frontoparietal	**175**	TPOJ3	141	Multimodal
56	p24pr	57	Cingulo-Opercular	**116**	i6-8	97	Frontoparietal	**176**	PeEc	122	Multimodal
57	33pr	58	Cingulo-Opercular	**117**	s6-8	98	Frontoparietal	**177**	TF	135	Multimodal
58	a24pr	59	Cingulo-Opercular	**118**	AVI	111	Frontoparietal	**178**	Pir	110	Orbito-Affective
59	p32pr	60	Cingulo-Opercular	**119**	TE1p	133	Frontoparietal	**179**	AAIC	112	Orbito-Affective
60	6r	78	Cingulo-Opercular	**120**	IP2	144	Frontoparietal	**180**	pOFC	166	Orbito-Affective

The following report presents a novel structural connectome of the human neocortex based on probabilistic diffusion tractography. The connectome is partially validated against retrograde tracing in macaques and the relationship between tract length and connection strength is quantified. Further validation is provided by reasonable connectivity properties

between contralateral homologous parcels, within language cortex, and between parcels lying at similar levels of the cortical hierarchy. Finally, the dMRI connectome is compared to cortico-cortico evoke potential (CCEP) and resting-state fMRI derived connectivity.

Materials & Methods

Subjects & data sources

No new data was collected for this study, and the existing data used was gathered from publicly available databases. Individual subject's high-resolution T1-weighted structural magnetic resonance volumes (MRI), Diffusion images (dMRI), and group average grayordinate resting-state function MRI (rs-fMRI) connectivity were gathered from the Human Connectome Project's (HCP) WU-Minn 1200 release (Van Essen et al., 2013) at https://db.humanconnectome.org. The diffusion imaging dataset consists of 1065 individuals (575 women), aged 22-36+ years old. The rs-fMRI group average cohort consists of 1003 individuals, 998 of whom are also in the dMRI dataset. These datasets include some twin and non-twin siblings. However, individuals' family structure, as well as exact age, handedness, and ethnicity are access-restricted to protect the privacy of the subjects and these data were not requested as they are not critical to this study. Group-average dense T1w/T2w myelination index were gathered from the same source. Macaque retrograde tracer connectivity was sourced from supplementary table 6 of (Markov et al., 2014). Parcel-by-parcel values were averaged across monkey and hemisphere. Group average, parcellated cortco-cortico evoked potential (CCEP) connectivity was gathered from the v1903 release of the Functional Brain Tractography project (F-TRACT) (David et al., 2013; Trebaul et al., 2018) at https://f-tract.eu.

Cortical parcellation & functional networks

The HCP multimodal parcellation scheme (HCP-MMP1.0), consisting of 180 cortical parcels per hemisphere, was projected from the Workbench (Marcus et al., 2011) 32k

grayordinate template brain to the FreeSurfer (Fischl, 2012) ico5 fsaverage template as per (Coalson et al., 2016). Using the FreeSurfer reconstruction directories gathered from the database, surface-based fsaverage parcel labels were mapped onto each individual's white matter surface using spherical landmark registration (fs_label2label), (Fischl et al., 1999). Grayordinate rs-fMRI connectivity values were morphed to the ico5 fsaverage template then averaged within each parcel. Finally, individual's surface-based parcel labels were converted to binary volumes marking the gray matter — white matter boundary (mri_label2vol) to serve as seed and target regions for probabilistic tractography. Workbench and FreeSurfer functions were sourced from releases 1.2.3 and 6.0, respectively.

To facilitate interpretation of the connectome, parcels were ordered and grouped into functional networks adapted from (Ji et al., 2019), which applied iterative Louvain clustering (Blondel et al., 2008; Rubinov and Sporns, 2010) and other criteria to a resting-state fMRI connectivity. These functional groupings and parcel order were selected as they were also generated using (a subset of) the WU-Minn HCP dataset and the HCP-MMP1.0 parcellation scheme. For this study the parcels of the left and right hemispheres were separated and the order and groupings of the left hemisphere in (Ji et al., 2019) were used for homologous parcels in the both right and left hemisphere, respectively, when combining data across hemispheres. Two pairs of the original networks (primary and secondary visual, ventral and posterior multimodal) contained too few parcels for effective analysis and were highly inter-related. These network pairs were simplified by combining them into visual and multimodal groups, yielding 10 functional networks per hemisphere, see table 1.1.

Probabilistic tractography

All analysis of diffusion imaging data was performed with FSL (Behrens et al., 2007; Jenkinson et al., 2012) release 6.0.1. Analyses were performed identically for each subject and broadly follow (Burns, 2014). The diffusion and bedpostX precursor directories made available

from the HCP database were used as inputs without modification. The WU-Minn HCP diffusion data are corrected for eddy currents and movement with FSL eddy (Andersson and Sotiropoulos, 2016). Subjects' estimated displacement over time from their initial position is written to the eddy_restricted_movement_rms output. Using these data , a scalar index of each subject's motion was derived by integrating their displacement over time.

Fractional anisotropy (FA) analysis was performed using dtifit. The resulting FA volumes were not analyzed but only used for registering the FreeSurfer and dMRI volumes (flirt), as is necessary to map the parcel masks into dMRI space (probtrackx2 arguments --xfm --seedref). Non-invasive probabilistic tractography was performed with probtrackx2 in voxel-by-parcel mode (--os2t --s2tastext). In this configuration, the number and length of streamlines (--ompl --opd) is estimated from each voxel in the seed parcel to each target parcel as a whole. To aid parallelization of these computationally intensive processes, the list of target parcels (--targetmasks) was quartered into four sub-lists. Therefore probtrackx2 was invoked 1440 times per subject, estimating the connectivity between 1 seed parcel and 90 target parcels in each invocation. The default ½ voxel step length, 5000 samples and 2000 steps were used (--steplength 0.5 -P 5000 -S 2000). To avoid artifactual loops, streamlines that loop back on themselves were discarded (-l) and tractography was constrained by a 90° threshold (-c 0) for maximal curvature between successive steps. Within-parcel connectivity and cotico-subcortical connectivity were not examined in this study. All post-hoc analyses and visualization of connectivity data were performed in Matlab 2019b (Mathworks) except for Figure 1.1C which was rendered in fsleyes.

Normalization & symmetrization

Raw streamline counts were averaged across all subjects, then normalized and symmetrized following procedure developed for non-human primate histological tracing (Donahue et al., 2016; Theodoni et al., 2021). Briefly, fractionally scaled values are defined as the

ratio of the number of streamlines originating at parcel A and terminating at parcel B to the total number of streamlines that either originate at parcel A or terminate at parcel B while excluding within-parcel connections.

Eq. 1 $F(DTI_{i,j}) = \frac{DTI_{i,j}}{\sum_{x=1}^{N} DTI_{i,x} + \sum_{y=1}^{N} DTI_{y,j}}, where\ x \neq i\ \&\ y \neq j$

Fractional scaling is one of several plausible normalization strategies. Because we used 5000 samples (-P 5000) and voxel-by-parcel mode (--os2t) in our probtrackX invocation, the maximum possible raw streamline count between any two parcels is 5000N where N is the # of voxels in the seed parcel. Note that because, for probtrackX, all parcels were defined as a single layer of 1mm isotropic voxels at the white matter — gray matter interface, Ni is also equivalent to the area of the seed parcel, in mm2. We examined four strategies for normalizing the raw streamline counts: (1) dividing by the number of samples, 5000, (2) dividing by the number of samples and seed area, 5000Ni, (3) dividing by the number of samples and the areas of both the seed and target parcels, 5000Ni0.5Nj0.5, and (4) fractional scaling, see Eq. 1 These approaches yield similar connectivity matrices, distributions of pairwise connectivity, and rates of connectivity fall-off with fiber tract distance. The choice of normalization does shift the absolute scale of pairwise connectivity strengths, but as this effect is mostly homogenous across all connections, subsequent analyses are not greatly affected. The correlation coefficient of connectivity strengths between normalization techniques exceeds 0.97 for all pairwise comparisons, and exceeds 0.99 if the samples-only normalization approach is excluded (data not shown).

While diffusion tractography is not sensitive to the directionality of connections, because parcel A to B and parcel B to A streamlines are computed separately minor asymmetries arise. Connectivity matrix symmetry is enforced by taking the arithmetic mean of the A-B and B-A fractionally scaled connection weights.

Eq. 2 $F_{i,j} = \frac{F_{i,j} + F_{j,i}}{2}$

Because probabilistic tractography values span several orders of magnitude, and are approximately log-normally distributed, data were log-transformed (log10) prior to subsequent analyses. The CCEP and rs-fMRI connectivity matrices were (re)normalized following the same procedure. However the rsMRI connectivity values were not log-transformed because these data are already approximately normally distributed, if bimodal, in linear space, see Figure 1.9B.

Network theory metrics

All network theoretic measures were computed in matlab using the Brain Connectivity Toolbox, 2019-03-03 release (Rubinov and Sporns, 2010). It is available at http://www.brain-connectivity-toolbox.net or https://www.nitrc.org/projects/bct.

Results

A whole-cortex structural connectome

Figure 1.1A shows the group average parcel to parcel and probabilistic diffusion tractography connectome. This matrix consists of connectivity among the 360 cortical parcels of the HCP-MMP1.0 atlas. Using left V1 connectivity as an example, Figure 1.1B illustrates the spatial mapping of the connectivity matrix to the cortex, and Figure 1.1C shows a rendering of streamline paths for one subject. The cortical parcels are further organized into 10 functional groups per hemisphere modified from (Ji et al., 2019). These larger functional groupings are shown in Figure 1.1D. The raw probabilistic tractography streamline counts have been normalized by fractionally scaling (Eq. 1) into log probabilities (F_{pt}) following procedures developed for tracing non-human primate connectivity. As dMRI reveals structural connections, the network is undirected and therefore symmetric. The main diagonal is masked as intra-parcel connectivity was not examined in this study. The upper left quadrant shows connectivity among the 180 parcels of the left hemisphere, the lower right quadrant the connectivity within the right hemisphere. The upper right and lower left quadrants are duplicates and show the inter-

hemispheric, or callosal, connections. The 180th (or half-) diagonal is clearly visible (white arrows); this shows the connectivity between homologous parcels in the right and left hemispheres, which is greater than non-homologous callosal connectivity for most parcels.

After log_{10} transformation, F_{pt} connectivity among all parcel pairs is approximately Gaussian in distribution with a mean -3.903 ($CI_{95\%}$ = [-3.910 -3.897]), standard deviation 0.8111 ($CI_{95\%}$ = [0.806 0.816]), skewness 0.627 ($CI_{95\%}$ = [0.6082 0.6440]), and kurtosis 3.605 ($CI_{95\%}$ = [3.5603 3.6498]). In addition to bringing the range of F_{pt} values into the same order of magnitude, log_{10} transformation is justified as it brings the distribution's skewness significantly closer to zero (pre-log_{10}: 9.047, $CI_{95\%}$ = [8.719 9.469]), and kurtosis significantly closer to three, pre-log_{10}: 103.684 ($CI_{95\%}$ = [93.991 117.026]) thus bringing the distribution closer to normality. Empirical confidence intervals were estimated via bootstrapping with 2000 iterations. The values of the group average and individual probabilistic dMRI connectivity matrices, as well as all other Figure source data can be found at https://doi.org/10.5281/zenodo.4060485.

Tract length strongly predicts connectivity strength, with exponential decay

In addition to the connection strength, diffusion tractography estimates the fiber tract length between all pairs of parcels. As shown in Figure 1.2, structural connectivity ($10\text{^}F_{pt}$) falls off as an exponential function of fiber tract length with the form $10\text{^}F_{pt} = a*e^{-d/\lambda}$ where λ is the length constant, a the scaling coeffect, and d the tract length. Alternative functional forms were examined, but the exponential was selected for parsimony, goodness-of-fit, and concordance with histological tracing data (see Discussion). Note that λ is sometimes reported in inverted units of mm^{-1}, e.g. (Markov et al., 2013; Theodoni et al., 2021), but we here use the λ convention from neuronal cable theory (Dayan and Abbott, 2001) which has more intuitive units (mm); the conventions are conceptually equivalent. For the group-average connectome, λ = 23.4 mm and the least squares exponential fit explains 84% of the variance in $10\text{^}F_{pt}$ across all parcel pairs. Callosal connectivity, when isolated, decays more slowly with respect to tract length, λ =

32.8, and hews to the exponential expectation less consistently $r^2 = 0.62$. Because the tracing of long fiber tracts may be hampered by poor scan quality, we investigated the effects of subjects' motion on λ. For each subject, λ was calculated for non-zero connections in the same manner as the group average. While subjects' motion within the scanner does reduce λ, this effect is modest, only explaining 1.96% of the inter-subject variance.

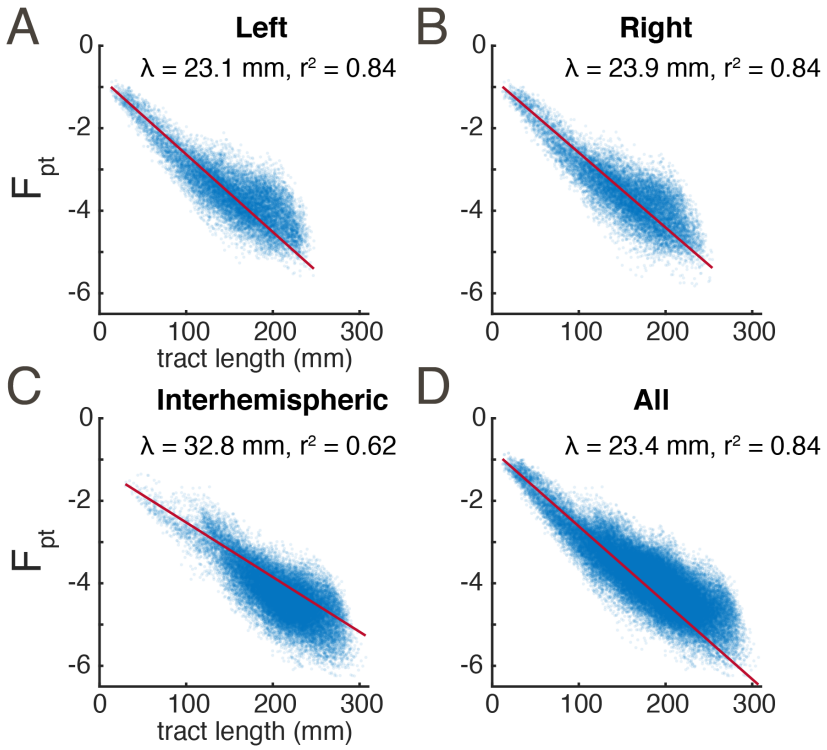

Figure 1.2 Connectivity strength exponential decays with fiber tract length. (A) and (B) connections within the right and left hemispheres, respectively. (C) Connections between the right and left hemisphere. (D) All connections. Each marker represents a pair of parcels. Red traces show the least-squares exponential fit; inset are the length constant λ and r2 of this fit. Note that Fpt is log-transformed making these axes effectively semi-log.

Inter-individual variability

The inter-individual variability of connectivity was assessed by deriving the across-subject coefficient of variation, CV, for each pairwise connection F_{pt}, see Figure 1.3. For this analysis, the normalization, symmetrization, and $\log_{10}$-transformation of raw connectivity values was performed on each subject. Pairwise connections with zero streamlines were not log-

transformed in order to avoid infinities. While there is no clear relationship between fiber tract distance and inter-individual variability, the most consistent connection appear in two clusters of around 50-100 mm and 170-225 mm (Figure 1.3B) . When the most consistent quintile of connections is isolated (Roberts et al., 2017), connectivity falls off more slowly with tract distance, with λ increasing to ~28 mm (Figure 1.3D). Since the proportional size of V1/V2 varies ~3-fold across individuals and is highly heritable (Yoon et al., 2019), we hypothesized that the ipsilateral V1-V2 connection would also be highly variable, with that variability being correlated across hemispheres. Indeed, we find that the ipsilateral V1 – V2 connection is very strong, with ~1.8 fold variability which is strongly correlated across hemispheres (r=0.70). The scatter-plot of right vs. left F_{pt} values for this connection across subjects (Figure 1.3F) does not reveal obvious outliers which would be indicative of subject-specific artifacts. This analysis of inter-individual variability should be considered preliminary. The WU-Minn HCP dataset is rich in individual data, including the NIH neuropsychological toolbox (Gershon et al., 2013), twin and non-twin siblings subsets, and genotypic data (dbGaP phs001364.v1.p1), though the latter two data types are only available by application in order to ensure subject anonymity. With access to these data, a full examination of inter-individual variability, including assessing the heritability and genetic correlates of the strength of specific connections could be made.

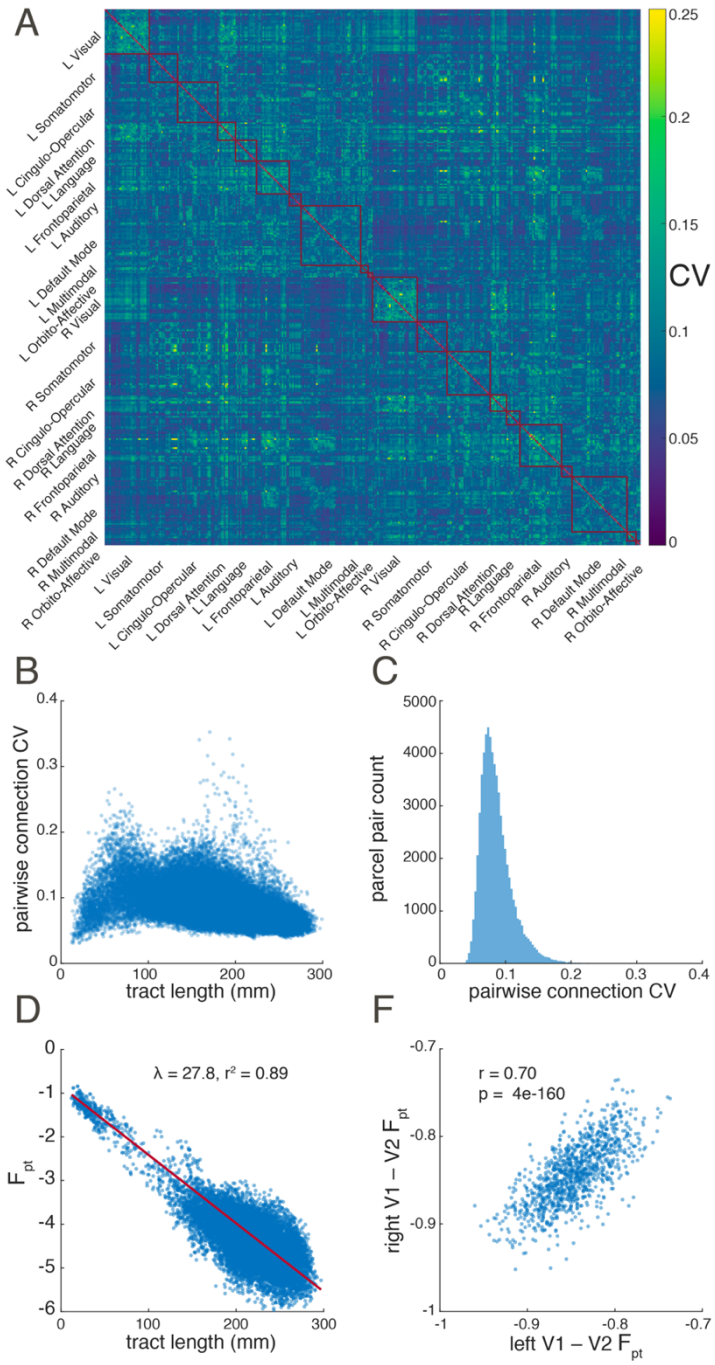

Figure 1.3 Inter-individual variability. Shown are (A) the matrix of connectivity coefficients of variation (CV) across subjects (B) pairwise CV vs. fiber tract length, (C) the distribution of CV across all connections, (D) the F_{pt} vs. fiber tract length for the connections in the highest quintile of inter-individual consistency, and (F) the F_{pt} of right hemisphere V1 – V2 connection in all subjects vs. left hemisphere V1 – V2 connection. In panels B and D each marker represents a sample statistic for a connection between two parcels. In panel F each marker represents an individual subject. In panel D the red trace show the least-squares exponential fit and inset are the length constant λ and r^2 of this fit. Note that F_{pt} is log-transformed making this panel's axes effectively semi-log. In panel F, the r^2 of the least squares linear fit is reported.

Probabilistic dMRI tract tracing in humans reasonably corresponds with histological fiber tracing in macaques

The development of both the HCP-MMP1.0 human cortical atlas (Matthew F. Glasser et al., 2016) and FV91 macaque parcellation scheme (Felleman and Van Essen, 1991) were led by David Van Essen and the parcel definitions of the human atlas were informed by human-macaque homology. As such, the parcel names of these atlases have considerable overlap, particularly for visual and visual association areas as well as the non-visual parcels 1, 2, 25, and 44. We therefore assumed that parcels with the same name were roughly homologous and limited the scope of the inter-species comparison to these parcels. Furthermore, the macaque FLne values found in (Markov et al., 2013) are directly comparable to fractionally scaled Fpt values (Donahue et al., 2016). Comparing the pairwise connectivity between species, we found a Pearson correlation of $r = 0.35$ ($p = 0.0013$), see Figure 1.4. Considering that for macaques, Donahue and colleagues (2016) found a *within-species*, between-technique correlation of $r = 0.59$ when comparing retrograde tracing and probabilistic diffusion tractography, we find the magnitude of *between-species* correlation to be reasonable supporting evidence for the efficacy of the technique.

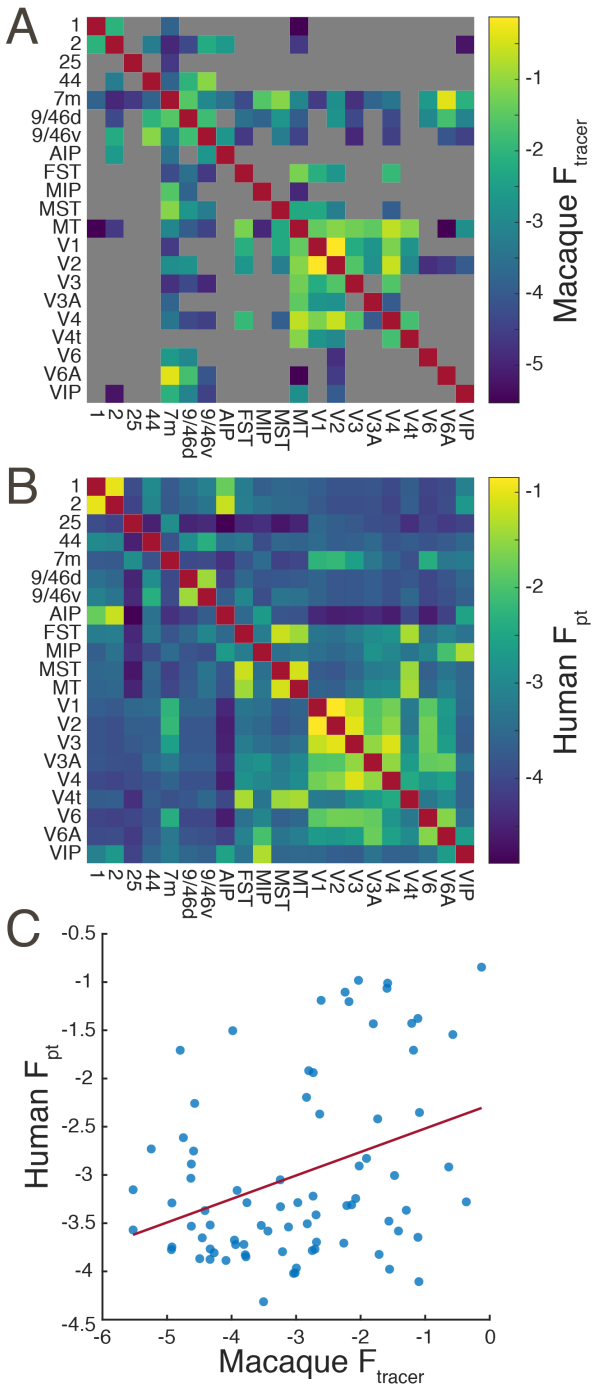

Figure 1.4 Comparison of human diffusion tractography and macaque retrograde tracing connectomes. Subset of homologous parcels in the human HCP-MMPS1.0 and macaque fv91 atlas. (A) Macaque group-average retrograde tracer derived structural connectome, gray indicates missing data. (B) Human probabilistic diffusion tractography connectome. (C) Pairwise correlation between macaque and human structural connectivity. R = 0.35 p = 0.0013

Contralateral connectivity exceeds ipsilateral connectivity in some regions

On the whole, cortical connectivity is dominated by ipsilateral connections. This effect is readily-observed by comparing the ipsilateral and contralateral quadrants of Figure 1.1A. However, there are exceptions to this rule. The differential connectome of ipsi- vs. contra-lateral connections is shown in Figure 1.5. This is achieved by subtracting the mean of left-right and right-left contralateral connectivity from the mean of the right and left ipsilateral connectivity, i.e. subtracting the mean of the first and third quadrants from the mean of the second and fourth. A cingulo-parietal somatomotor region (parcels 5m, 5L, 24dd, and 24dv) are more strongly connected to most contralateral cortex than ipsilateral cortex. Lateromedial connectivity in select prefrontal (a10p, a9-46v, a10p, p10p, p47r, p9-46v, 11l, IFSa, IFJp, a24, d32, p32, 10r) and postcentral – superior parietal lobule (LIPv, VIP, 7AL, 7PC, 1, 2, 3a, 6d, 31a, 31pd, PCV) regions is stronger between hemispheres than within them. We speculate that a possible commonality between these three regions is that they have been broadly implicated in the unitary processes of somatosensory object recognition, emotion, and spatial cognition, respectively. Conversely, the entire auditory network and superior temporal cortices (STGa, STSda, DTDdp, A5, and TPOJ1) as well as the operculum and temporoparietal junction (Ig, MI, FOP1-FOP5, OP1-OP4, PF, PFcm, PFop, PI, PoI1, PoI2, and 43) have pronounced hyper-ipsilateral connectivity, consistent with the low transmission latency required for auditory processing, the left-lateralization of language, and the right lateralization of attention.

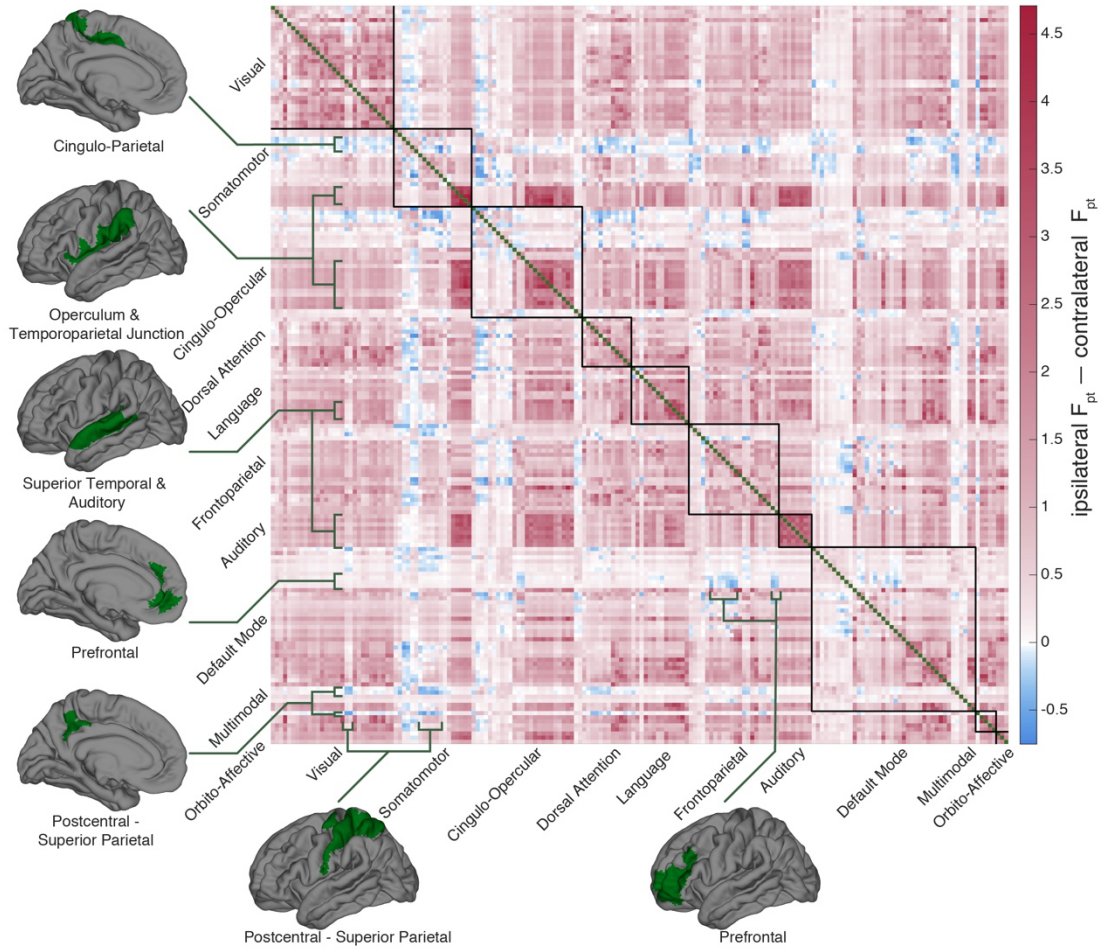

Figure 1.5 Interhemispheric connectivity. Differential connectivity between ipsilateral and contralateral connectivity. Greater Ipsilateral connectivity dominates and is indicated in red. Parcel-pairs with greater *contra*lateral connectivity than ipsilateral are blue. The green cortical patches show anatomic extent of parcel groups of notable contrast.

With the exception of some language areas, most parcels are disproportionately connected to their contralateral homologs

The two hemispheres of the cortex have a high degree of functional and anatomical symmetry. It follows then that most regions will have greater connectivity to their contralateral homologs than other contralateral areas, in order to coordinate their overlapping processing tasks. This is hinted at by the visibility of the 180th, (or half-) diagonal in Figure 1.1A. To further quantify this effect, for all 180 parcels we compared the connectivity between interhemispheric homologs to the mean of all other callosal connectivity. Bonferroni corrected, empirical 95% confidence intervals were estimated via bootstrapping with 2000 iterations. As visualized in

Figure 1.6, 147 parcels are hyperconnected to their contralateral homologs, 18 are hypoconnected, and 15 have homologous callosal connectivity not significantly different than their callosal mean connectivity. Interestingly, parcels that are not hyper-connected to their contralateral homologs are concentrated within and adjacent to the language network, consistent with the greater degree of lateralization in these areas.

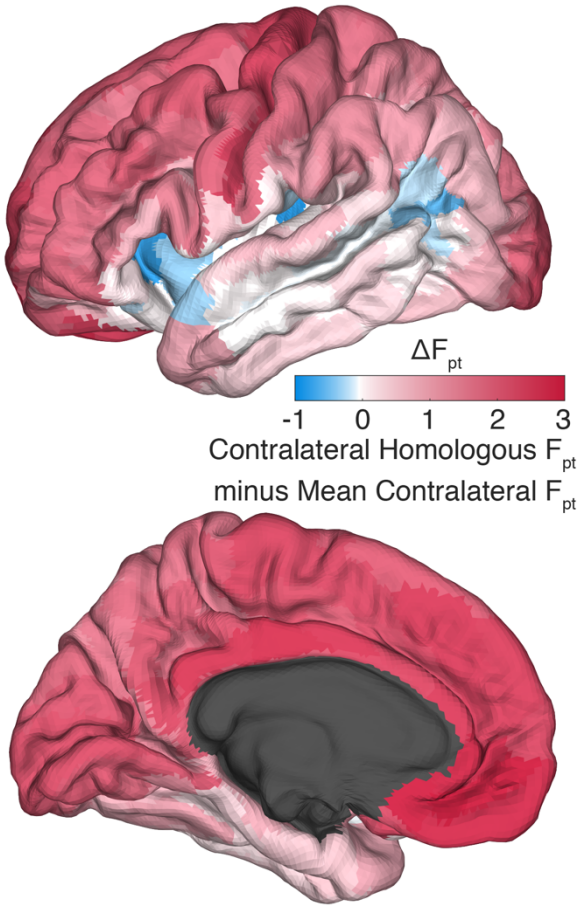

Figure 1.6 Contralateral homologs. Differential connectivity between contralateral homologous parcels vs the mean of all other contralateral parcels. Red indicates contralateral homologous connectivity greater than mean contralateral connectivity. Note that many language-implicated regions have relatively weak connectivity with their contralateral homologs.

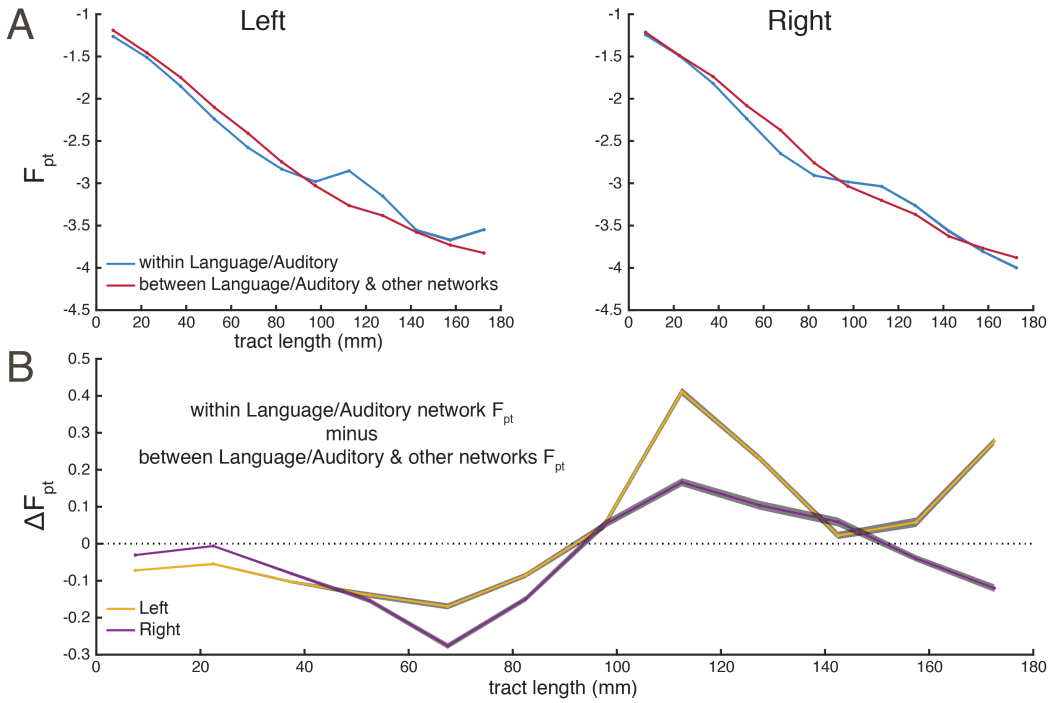

Figure 1.7 Language/Auditory network hyperconnectivity and left-lateralization. (A) Distance-binned connectivity within the language and auditory networks compared to connectivity between the language and auditory networks and other networks, separately for the left and right hemispheres (B) The differential trace for the within- and between- connectivity in both hemispheres. In both panels, gray patches show Bonferroni-corrected bootstrapped 95% confidence intervals across subjects.

The language network is hyper-connected at long distances and left lateralized

In order to investigate distance-resolved left laterality in connections among language-implicated cortex, pairwise connections were binned by fiber tract length in 15 mm increments. Within each bin, connections were grouped as being within the combined language and auditory network, or between the combined networks and the rest of the cortex. For each subject, the F_{pt} of grouped connections within each bin was averaged before being log-transformed. The grand-averages of these within- and between- language/auditory cortex in each distance bin for each hemisphere are shown in Figure 1.7A. Bonferroni corrected, empirical 95% confidence intervals for these grand-averages were estimated via bootstrapping with 2000 iterations. Within-language connectivity is slightly attenuated at distances less that 100 mm, but

strongly amplified at distances above 100 mm, especially ~100-140 mm connections in the left hemisphere. A plurality of these are between frontal and temporoparietal language areas (18/45 connections between 100 and 140mm). The differential traces of between- vs. within-language connectivity (Figure 1.7B) clearly show the left-hemisphere dominance of this effect.

Connectivity is influenced by the cortical hierarchy

Hierarchy is a central organizing principle of the cortex (Burt et al., 2018; Felleman and Van Essen, 1991; Markov et al., 2014; Theodoni et al., 2021). Higher order areas, e.g. supporting abstract processing, have low myelination, and lower order areas, e.g. supporting unimodal sensory processing, have high myelination. Furthermore, areal myelination is indexed by the ratio between T1- and T2-weighted MRI contrast (Glasser and Van Essen, 2011). The WU-Minn HCP 1200 release includes smoothed group-average myelination indices for all vertices in the 32k grayordinate template brain. These values were averaged for each parcel in the HCP-MMP1.0 atlas (Matthew F. Glasser et al., 2016) to yield a group-average parcel-wise index of myelination.

The relationship between cortical hierarchy and connectivity was assessed in two ways. We first examined whether regions of similar level in the cortical hierarchy are better connected, as predicted by (Barbas, 2015). An index of hierarchical similarity, $F_{|\Delta \text{ myelination}|}$, was obtained for each pair of parcels by computing the pairwise difference in myelination between parcels and fractionally scaling it in the same manner as F_{pt}, with smaller values indicating hierarchical closeness. Correlations were obtained for the left and right hemisphere as a whole as well as the colossal connections, Figure 1.8A. In addition, for each of the twenty functional networks (10 per hemisphere) the Pearson correlation between the $F_{|\Delta \text{ myelination}|}$ and F_{pt} for pairwise within-network connections was computed, see Figure 1.8B. With the exception of the interhemispheric connections, calculations were performed on the hemispheres separately to avoid the collinearity introduced by hemispheric homology.

With the exceptions of the bilateral visual and somatomotor networks and right language network, for which there is convincingly no relationship, the preponderance of coefficients are negative, indicating that, on average, areas at similar levels of the cortical hierarchy are better connected. However, quantified in this way, the influence of hierarchy is modest, explaining about 1% of the variance in F_{pt} overall, though perhaps 10-30% in certain subsets of parcels, such as the left auditory and language networks. The left lateralization of the influence of hierarchy in these networks is striking, as is the right-lateralization of the dorsal attention network.

Secondly, we investigated whether a cortical region's hierarchical level affected its overall connectivity. For each parcel, the Pearson correlation between the parcel's F_{pt} to all other parcels and the parcel-wise index of myelination was computed. In other words, correlation between each row of the connectome matrix and the vector of myelination indices was obtained. After Bonferroni correction for multiple comparisons, 74 of 360 parcels have connectivity significantly correlated to their myelination index and of these the vast majority (70) are negatively correlated, indicating that low myelination predicts high connectivity, see Figure 1.8C. These areas form a contiguous bilateral prefrontal network as shown in Figure 1.8D, indicating that prefrontal areas are more connected with higher cortical regions. The rare positively correlated exceptions are the left and right DVT and V6A.

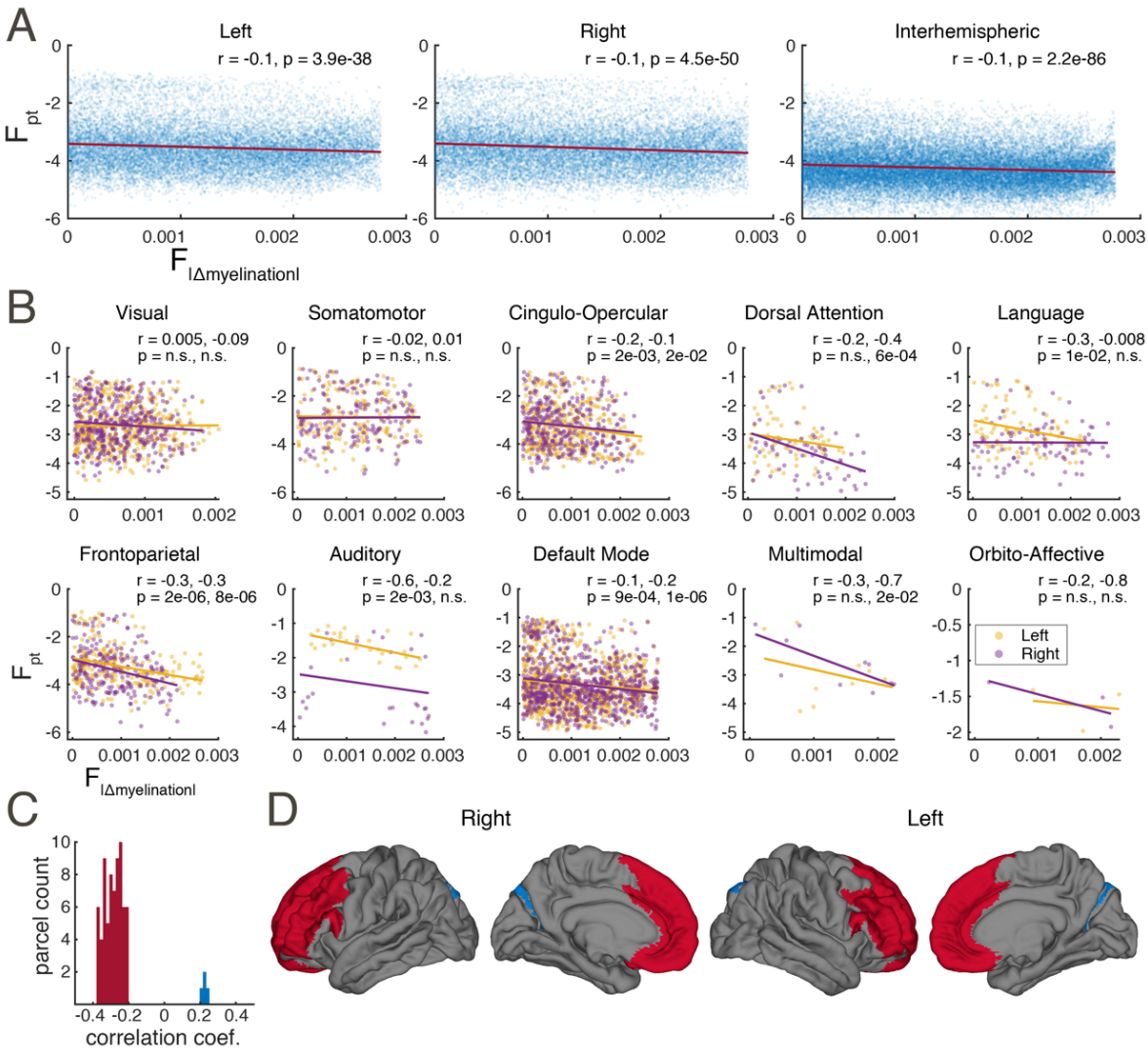

Figure 1.8 Connectivity is influenced by the cortical hierarchy. (A, B) Connectivity is strongly predicted by hierarchical similarity in some networks and modestly predicted overall. (A) All connectivity vs. myelination difference, including within- and across- network connections, for the left, right, and callosal connections. For both panels, each marker represents a parcel pair. (B) Within-network connectivity vs. myelination difference for 10 functional networks. Linear fits and correlation coefficients computed independently for the left and right hemisphere. A negative correlation indicates that parcels at similar hierarchical levels tend to be more connected. (C, D) Higher order prefrontal areas are better connected. (C) Histogram of correlation coefficients between areal myelination and F_{pt} connectivity to each parcel. Only significant coefficients after Bonferroni correction are shown. Most coefficients are negative indicating high connectivity to low-myelination (i.e., higher-order) areas. (D) Significant negative coefficients (red) map onto bilateral prefrontal cortex. Only the bilateral DVT and V6A are show positive significant correlations (blue).

Probabilistic dMRI connectivity more closely resembles CCEPs than resting-state fMRI

In order to further contextualize the dMRI connectome, we compared it to existing connectivity matrices generated from two other brain mapping modalities: cortico-cortico evoked potential probability (CCEP) and resting-state fMRI correlation magnitude (rs-fMRI). As shown Figure 1.9A, the qualitative pattern of rs-fMRI markedly differs from the other two modalities with proportionally stronger ipsilateral across-network connections and especially non-homologous contralateral connections, though the latter is somewhat obscured for CCEPs due to sparse spatial sampling. Over all connections, pairwise probabilistic dMRI connectivity values are nearly twice as linearly correlated to pairwise CCEP connectivity than to rs-fMRI connectivity (Figure 1.9B**)**, and this contrast is equally evident in the ipsilateral connection within each hemisphere. Contralateral connections were not examined in isolation as contralateral sampling for the CCEP modality is relatively rare.

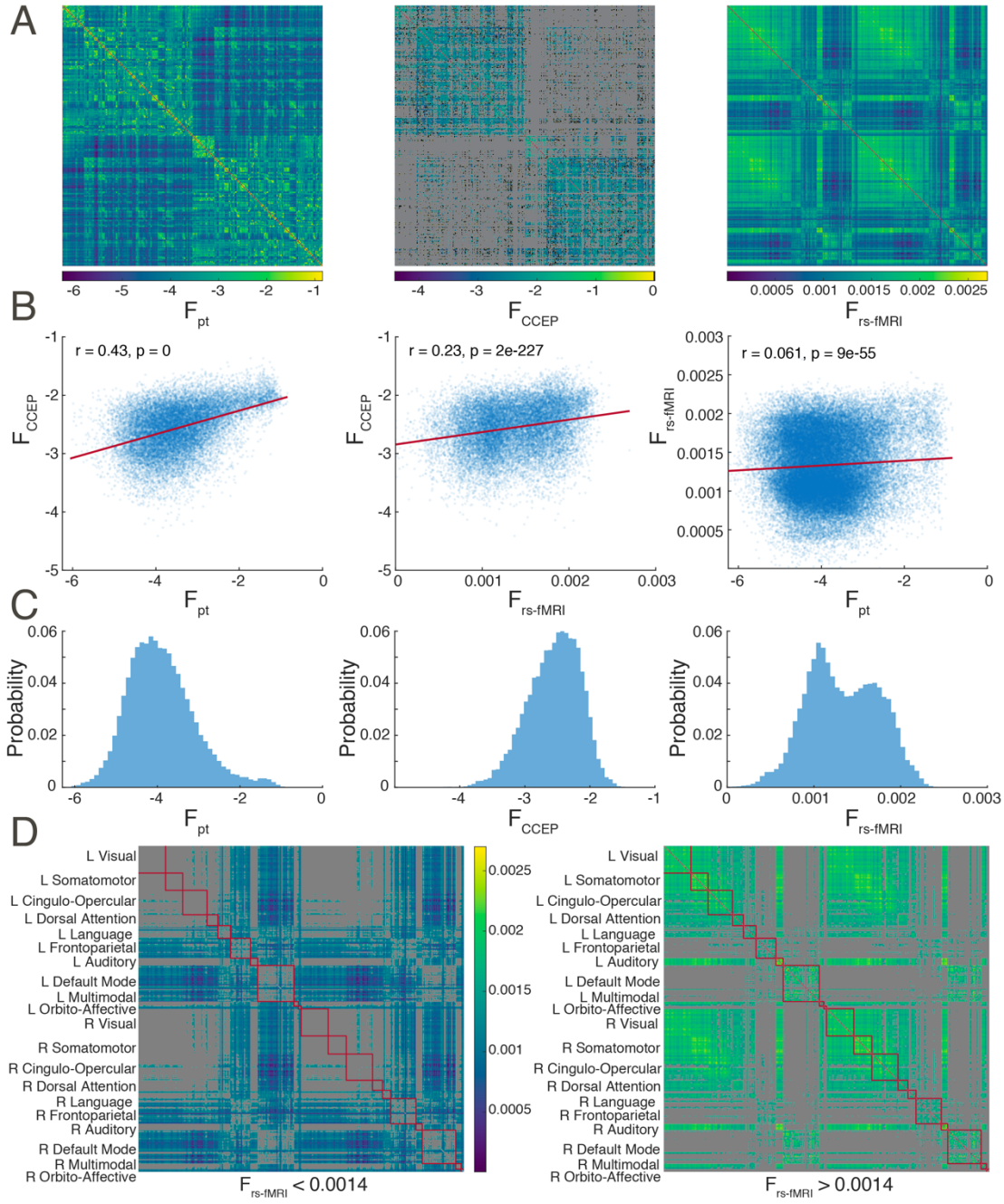

Figure 1.9 Probabilistic dMRI more closely resembles CCEPs than resting-state fMRI. (A) Connectivity matrices for probabilistic dMRI tractography, CCEP, and rs-fMRI. For CCEPs missing data has been colored grey and pre-log zero-strength connections black. (B) Correlations among the three modalities. The least-squares linear fit is shown in red. (C) Non-zero pairwise connection strength distributions. Note that rs-fMRI connectivity values, which are not log-transformed, display two modes, separated at 0.0014. (D) Cortical parcels displaying lower (left) and higher (right) modes of rs-fMRI connectivity.

When comparing the distributions of pairwise connectivity strength (Figure 1.9C), rs-fMRI again exhibits properties different than the other two modalities. While both dMRI and CCEP distributions skew in opposite directions (0.63 and -0.43, respectively), their strengths form unimodal log-normal distributions and thus shown with log-transformed values. In contrast, rs-fMRI connectivity values form a bimodal Gaussian-mixture distribution in linear space. The two modes were characterized by obtaining the maximum-likelihood fit (fitgmdist) of a 2-component Gaussian-mixture to the data, yielding a left mode (μ = 0.0011, σ = 8.1e-8) forming 63% of the distribution and a right mode (μ = 0.0017, σ = 8.1e-8) forming 37%, respectively. Splitting the rs-fMRI modes at the midpoint between their means (0.0014) and plotting their respective connectivity matrices (Figure 1.9D) reveals that the low-connectivity (left) mode consists primarily of connections between the default mode / frontoparietal networks and other regions of the cortex.

To further contrast the three connectivity modalities we computed six network theoretic metrics for each of the connectivity matrices: mean clustering coefficient (MCC), characteristic path length (CPL), global efficiency, gamma (normalized MCC), lambda (normalized CPL), small worldness, transitivity, and assortativity. Binarized network metrics were assessed after thresholding by edge weight (connectivity strength) at intervals of 0.1. Note that this lambda is unrelated to the exponential length constant reported above. To account for the order-based arbitrary treatment of equal edge weights when thresholding, the node (parcel) order was randomized 1000 times, and the mean metric values are shown. Empirical 95% confidence intervals for these means are too small to be shown at scale. Networks densities above 0.6 were not examined as the un-thresholded network density of CCEP connectivity matrix, treating missing data as non-connections, is less than 0.7. However, all measures appear to converge as binary network density approaches 1. As shown in Figure 1.10, the MCC, CPL, global efficiency, small worldness, transitivity, and assortativity are markedly different for rs-fMRI connectivity than for CCEP and probabilistic dMRI tractography, whose metrics as a function of network density

are more similar to each other. Normalizing by metrics computed for a random network with the same statistical makeup changes this pattern. For gamma the rs-fMRI and CCEP networks are more similar than either is to probabilistic dMRI tractography, and lambda rs-fMRI and probabilistic dMRI tractography are more similar than either is to the CCEP network. The high MCC, transitivity, and assortativity and low global efficiency of rs-fMRI relative to the other modalities may be indicative of strong, long-range correlativity beyond that predicted by anatomical connections.

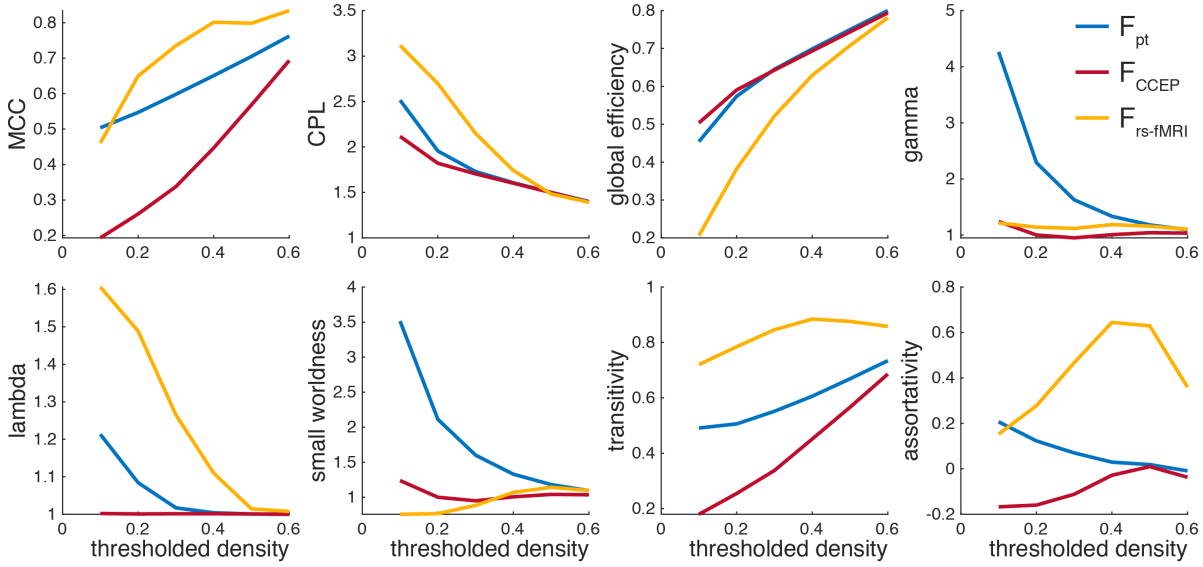

Figure 1.10 Network theoretic differences between the connectivity modalities. Binarized network metrics after thresholding by edge weight (connectivity strength).

Discussion

In this study we compiled a whole-cortex structural connectome by applying probabilistic tractography to the diffusion MR volumes of 1065 subjects from the WU-Minn Human Connectome Project. We report a novel, complete, and high-dynamic-range connectivity matrix discretized into the 360 parcels of the HCP-MMP1.0 atlas and further arranged into 10

functional networks. It is shown that connectivity strength exponentially decays with fiber tract length, that the parts of the connectome with clear homology to macaques correspond reasonably to retrograde tracer mappings in that species, that contralateral homologs are hyperconnected, and that some connections within language-implicated cortex are stronger than expected and left-lateralized. While ipsilateral connectivity generally dominates, some regions have stronger contralateral connections. Inter-individual variability is relatively high for early visual cortex, whose connectivity co-varies across hemispheres. Cortical areas tend to be more connected with areas at similar levels of the cortical hierarchy, as indexed by their estimated myelination, particularly in prefrontal areas. Lastly, it is shown that probabilistic tractography connectivity more closely resembles that of CCEPs than rs-fMRI. In sum, we quantify a dMRI-based estimate of medium- to long-range anatomical cortico-cortical connectivity in a large normative sample.

Diffusion MR imaging and automated post-hoc tractography are powerful tools for the elucidation of cerebral connectivity. The defining advantages of these techniques are non-invasiveness and large field-of-view, enabling whole-brain mapping in humans. However, dMRI does have significant limitations when compared to histological fiber tracing, EM microscopy, or stimulation. The most obvious of these is insensitivity to whether underlying axons are anterograde or retrograde, as evidenced by the symmetry of the connectivity matrix. The anisotropic diffusion of water molecules occurs in both anterograde and retrograde directions. Thus, the true one-way connectivity between two areas could be anywhere between none to all of the symmetric diffusion connectivity. Another important limitation is spatial resolution. While the 1.25 mm isotropic voxels achieved by the WU-Minn dMRI protocol are smaller than those of most studies (Jeurissen et al., 2019), they are still more than three orders-of-magnitude larger than the typical submicron axon diameter (Liewald et al., 2014; von Keyserlingk Graf and Schramm, 1984). This discrepancy is particularly impactful when fiber orientations are not consistent within a voxel, i.e. crossing fibers. Probabilistic diffusion tractography (Behrens et al.,

2007) partially ameliorates the issue by modeling the probability distribution of orientations and accounting for uncertainty, but ultimately dMRI with current technology is a meso- to macroscale technique. Direct histological validation of dMRI techniques is uncommon, but has been performed for probabilistic tractography in vitro in pigs (Dyrby et al., 2007) and macaques (Donahue et al., 2016; Jbabdi et al., 2013), with the latter two studies using the same probtrackX algorithm as the current study (Behrens et al., 2007). We have extended these validations with a between-species comparison (Figure 1.4).

Of the several families of dMRI tractography algorithms available, we selected local, probabilistic tractography (Behrens et al., 2007). The WU-Minn HCP makes available the bedpostX precursor files and creating a probabilistic tractography connectome was always a stated component of the WU-Minn HCP project (Van Essen et al., 2013; Van Essen and Ugurbil, 2017). That such a connectome has not yet been released for these data may be due to the immense computational challenge of performing these analyses at the scale of the HCP. An advantage of probabilistic tractography is its sensitivity to minor, or low-probability connections. Deterministic dMRI tractography connectomes typically have low network densities, e.g. 0.18 (Mori et al., 2008) or 0.23 (Cui et al., 2019), when compared to histological fiber tracing in macaques, 0.66 (Markov et al., 2014), and this is likely a lower bound as such tracing is subject to false-negatives due to imperfect dye uptake and incomplete cortical sampling. This suggests the deterministic dMRI connectomes are missing weaker connections. On the other hand, dMRI in general and probabilistic tractography in particular has been found vulnerable to false-positive connections (Maier-Hein et al., 2017). This exchange of specificity for sensitivity (Sarwar et al., 2019; Zalesky et al., 2016) is consistent with our very high group-average network density of 1.0 and the likely presence false-positive connections, and is thus an important caveat to the data presented here. In cases where false-negative connections are less concerning than false-positive connections, such as topological analyses (Zalesky et al., 2016), subsequent users of

these data may opt to threshold the connectivity matrix by either connection strength or consistency (Roberts et al., 2017), see Figure 1.3.

When constructing this connectome, we divided the cortex into 180 parcels per hemisphere following the HCP-MMP1.0 atlas (Glasser et al., 2016). To ease interpretation, we further organized the parcels into 10 functional networks modified from (Ji et al., 2019). These networks were created by applying iterative Louvain clustering (Blondel et al., 2008; Rubinov and Sporns, 2010) and other criteria to HCP resting state fMRI data. While these fMRI-defined network definitions correspond reasonably to the structural connections reported here, there are exceptions. The operculum and temporoparietal junction, in particular, appears to be a structurally distinct area that has been folded into several functional networks (Ji et al., 2019). However, this contiguous region forms the lateral salience network in (Barnett et al., 2020) which similarly applied a very similar methodology to a non-HCP cohort. Like many cortically-focused studies, we used a surface-based methodology to define these areas, with seed and target regions constrained to the white-matter – gray-matter interface. This approach reduces the overrepresentation of major bundles (Jeurissen et al., 2019), enables the automated assessment based on inter-subject homology (Fischl et al., 1999), facilitates comparison to other cortical datasets, and is true to the anatomical nature of the cortical ribbon. Unfortunately, the subcortex and cerebellum are omitted in this analysis, as are short-range, often unmyelinated, intra-parcel connections. While the inclusion of the thalamic radiations, in particular, is a merited future extension of this connectome, the small size of subcortical structures relative to diffusion imaging voxels, the nuclear (as opposed the sheet-like) organization of subcortical structures, and complex geometry of the subcortical white matter — gray matter interface (e.g. the internal medullary lamina of the thalamus), all render the challenges and methods for obtaining subcortical tractography substantially distinct from those of cortico-cortico tractography.

The HCP-MMP1.0 atlas used was selected because of its wide adoption, symmetry, and high parcel count. Furthermore, the parcels are based on multiple functional and anatomical

criteria and are consistent with previous functional parcellations in human and non-human primates (Felleman and Van Essen, 1991; Glasser et al., 2016). Because the parcels are relatively small and informed by function, erroneous averaging of disparate connections, a connectomic extension of the partial volume artifact, is minimized. However, this comes at the cost of non-uniformity in both parcel area and shape. Methodologically, parcels are assembled from vertices on the tessellated cortical surface. A future vertex- or voxel-based connectome, while computationally challenging, would have the distinct advantage of being readily reformulated into any arbitrary surface-based parcellation scheme.

We found that pairwise connectivity between cortical parcels exhibits an exponential decay rule with respect to fiber tract distance with a length constant λ of ~23 mm (~33 mm for callosal connections). While a tight exponential relationship between probabilistic diffusion tractography strength and fiber length has been previously reported, (Roberts et al., 2016), this study did not report the observed λ or release its data. Histological studies in non-human primates (Donahue et al., 2016; Markov et al., 2013; Theodoni et al., 2021) consistently show exponential connectivity decay with distance. Such a rule when combined with a roughly Gaussian distribution of interareal distances explains the observed log-normal distribution of connectivity strength (Markov et al., 2013). Histological data indicate a λ of about 3.33 mm for marmosets (Theodoni et al., 2021) and 5.55 mm for macaques (Markov et al., 2013). Across species, there appears to be a linear relationship between the logs of λ and total gray matter volume, predicting a human λ of 10 mm (Theodoni et al., 2021). While methodological differences between diffusion and histological tractography cannot be completely ruled out, Donahue and colleagues found similar λ for the two methods in macaques (Donahue et al., 2016). Our results suggest that, compared to other species, human cortical areas are exceptionally well connected relative to their cortical volume, reflected in a disproportionately long λ. Conservatively restricting the exponential fit to only the most consistent quintile of

connections (Figure 1.3D) yields a λ of ~28 mm, further accentuating the proportional long-range hyperconnectivity of humans.

Geometric scaling strongly constrains cortico-cortical connectivity in humans. Considering primate brains increasing in diameter d, volume and number of cortical neurons increases by d3,(Ventura-Antunes et al., 2013), so arriving at a constant probability of connection between any two neurons would require d6 axons, and since they would need to be about d times as long, this would require a volume proportional to d7, or more if axonal diameter is increased to maintain a relatively constant latency of communication (Wang et al., 2008). However, the actual white matter volume is less than d4 (Zhang and Sejnowski, 2000), and consequently the probability of cortico-cortical connectivity must be highly limited in humans. The relatively long λ in humans we report reduces even further the number of connections which can be accommodated within the available white matter volume. A consequence of fewer but longer connections would be reduced metabolic cost, inasmuch the cost of an action potential is 1/3 axonal transmission (proportional to length) and 2/3 synaptic transmission (Lennie, 2003). The low firing rate of human pyramidal cells (Chan et al., 2014) would also reduce the metabolic cost of their axons. These observations are consistent with the proposal that the metabolic costs of cortico-cortical connections may help constrain their organization in the primate brain (Ercsey-Ravasz et al., 2013). Given this strong correlation of connection strength with distance, as well as the bias of tract-tracing techniques toward shorter, less geometrically complex connections (Jeurissen et al., 2019), there may be some merit in regressing out the effect of tract length when evaluating the relative connectivity of different cortical areas. However, the considerations enumerated above imply a strong evolutionary selection to place cortical parcels which require high connectivity to perform their calculations to be situated in direct physical proximity to each other. The patterns of relatively long distance connectivity identified here thus must be viewed as minor deviations from an overall strong tendency favoring local

connectivity, a conceptualization consistent with the view of the cortex as a spatially embedded small world network.

One striking deviation from the distance-based connectivity was the left-lateralized hyper-connectivity between language areas, and specifically between posterior and anterior language areas. This connectivity presumably passes, completely or in part, through the classical language pathways (reviewed in (Dick and Tremblay, 2012)). The lateralization we observed may then reflect that of the arcuate and inferior longitudinal fasciculi which connect the same structures and show significant left lateralization in humans but not macaques (Eichert et al., 2019; Panesar et al., 2018). Left-lateralization of the arcuate fasciculus develops late (Lebel and Beaulieu, 2011), and is sensitive to the presence, quality and quantity of early language experience (Cheng et al., 2019; Romeo et al., 2018). More generally, many of the connectivity patterns observed here could be the indirect result of co-activation of the connected parcels (Mount and Monje, 2017). The left-lateralized ipsilateral connectivity may be compensated by a relative lack of callosal connections from the same areas, under the hypothesis that the total connectivity is constrained.

A more general factor that might induce deviations from a distance-based connectivity rule may be the principle of hierarchical organization. It has been proposed that distant areas with similar laminar properties, and thus of similar hierarchical order may have privileged connections (Barbas, 2015). Across the entire cortex we find that myelination similarity explains a significant but small amount of the overall variance. However, there are regions where the influence of hierarchical position is more pronounced including the right dorsal attention and left auditory/language networks. The observed hyperconnectivity and high degree of lateralization in these regions may be a consequence of the low-latencies necessary for the functions they underly. More broadly, the effects of transmission latency constraints on neuroanatomy and conduction delay on large-scale physiological recordings are an emerging area of study in human neuroscience (Muller et al., 2018). Latency is a hybrid structural–functional property of

connectivity, and might in future be quantified using the latency of cortico-cortical evoked potentials (CCEP).

By emphasizing the cortical connectivity matrix over the white matter bundles per se and organizing the matrix into the widely adopted HCP-MMP1.0 atlas (Glasser et al., 2016), the structural connectome reported here enables ready comparison to other structural, functional, and hybrid connectomes. As an example, we compared the probabilistic tractography connectivity to exist resting-state fMRI (rs-fMRI) (Van Essen et al., 2013) and CCEP (Trebaul et al., 2018) connectivity matrices and found that our dMRI-inferred structural connectivity better reflects CCEP probability than rs-fMRI connectivity in both linear and network-theoretic comparisons, despite the dMRI and rs-fMRI cohorts being highly overlapping. This is not unreasonable, as functional correlations are to varying degrees neurobehavioral state-dependent and far more spatiotemporally dynamic than structural connections. Furthermore, although resting-state functional connectivity is constrained by anatomical networks and can be partially predicted by them (Honey et al., 2009), indirect connections or parallel processing of stimuli in different areas can produce correlated activity even in the absence of direct anatomical connections. One notable example of the latter may be inter-hemispheric connectivity. While we did find hyperconnectivity between inter-hemispheric homologs when compared to other callosal connections, anatomical interhemispheric connectivity on the whole is much weaker than found in rs-fMRI. CCEPs, being directed by clinical requirements, have poor inter-hemispheric sampling, but we found that even among ipsilateral connections, rs-fMRI is still less similar to CCEP than probabilistic tractography. These inter-modal connectivity comparisons are not intended to be comprehensive. The HCP cohort also includes source-localized resting-state magneto-encephalography (MEG) (Larson-Prior et al., 2013), which could be used to examine the degree to which the functional connectivity of various frequency bands corresponds to anatomical connectivity. Furthermore, neuropsychological metrics, including the NIH toolbox (Gershon et al., 2013), and genotypic data (dbGaP phs001364.v1.p1) are also

available for this cohort, enabling future studies of the interplay between cortical connectivity, cognition, and genetics.

The Human Connectome Project was a scientific undertaking of visionary scope and ambition. Its commitment to open science and accessibility of data by the public enabled this study and will continue to facilitate further studies for years to come. Emerging clinical applications of brain connectomics will be underpinned by a strong base of normative data for comparison. The whole-cortex probabilistic diffusion tractography connectome reported here fulfills a key goal outlined in the project's conception and we hope it will empower yet further study of the myriad and beautiful web of connectivity that the human brain embodies.

Acknowledgements

This work was supported by National Institute of Mental Health Grants 1RF1MH117155 and 5T32MH020002, the National Institute of Neurological Disorders and Stroke Grant 1R01NS109553, and the Office of Naval Research Grant 00014-16-1-2415. We thank Adam Niese and the San Diego Supercomputer Center for providing technical support. Data were provided, in part, by the Human Connectome Project, WU-Minn Consortium (Principal Investigators: David Van Essen and Kamil Ugurbil; 1U54MH091657) funded by the 16 National Institutes of Health (NIH) Institutes and Centers that support the NIH Blueprint for Neuroscience Research; and by the McDonnell Center for Systems Neuroscience at Washington University. Data were provided, in part, by the Functional Brain Tractography Project, funded by the European Research council.

Chapter 1, in full, is a reprint of the material as it appears in Rosen BQ, Halgren E. 2021. A whole-cortex probabilistic tractography connectome. *eNeuro*, 8 (1). The dissertation author was the primary investigator and author of this paper.

References

Andersson JLR, Sotiropoulos SN. 2016. An integrated approach to correction for off-resonance effects and subject movement in diffusion MR imaging. Neuroimage.

Barbas H. 2015. General Cortical and Special Prefrontal Connections: Principles from Structure to Function. Annu Rev Neurosci 38:269–289.

Barnett AJ, Reilly W, Dimsdale-zucker H, Mizrak E, Reagh Z, Barnett AJ. 2020. Organization of cortico-hippocampal networks in the human brain 1–30.

Behrens TEJ, Berg HJ, Jbabdi S, Rushworth MFS, Woolrich MW. 2007. Probabilistic diffusion tractography with multiple fibre orientations: What can we gain? Neuroimage 34:144–155.

Blondel VD, Guillaume JL, Lambiotte R, Lefebvre E. 2008. Fast unfolding of communities in large networks. J Stat Mech Theory Exp.

Burns S. 2014. A Recipe for Cortical Tractography Using Freesufer Labels. http://sburns.org/2014/05/03/cortical-tractography-recipe.html

Burt JB, Demirtaş M, Eckner WJ, Navejar NM, Ji JL, Martin WJ, Bernacchia A, Anticevic A, Murray JD. 2018. Hierarchy of transcriptomic specialization across human cortex captured by structural neuroimaging topography. Nat Neurosci 21.

Chan AM, Dykstra AR, Jayaram V, Leonard MK, Travis KE, Gygi B, Baker JM, Eskandar E, Hochberg LR, Halgren E, Cash SS. 2014. Speech-specific tuning of neurons in human superior temporal gyrus. Cereb Cortex 24:2679–2693.

Cheng Q, Roth A, Halgren E, Mayberry RI. 2019. Effects of Early Language Deprivation on Brain Connectivity: Language Pathways in Deaf Native and Late First-Language Learners of American Sign Language. Front Hum Neurosci 13:1–12.

Coalson T, Van Essen D, Glasser M. 2016. hcp-users FAQ #9: How do I map data between FreeSurfer and HCP?

Cui LB, Wei Y, Xi Y Bin, Griffa A, De Lange SC, Kahn RS, Yin H, Van Den Heuvel MP. 2019. Connectome-Based Patterns of First-Episode Medication-Naïve Patients with Schizophrenia. Schizophr Bull 45:1291–1299.

David O, Job AS, De Palma L, Hoffmann D, Minotti L, Kahane P. 2013. Probabilistic functional tractography of the human cortex. Neuroimage 80:307–317.

Dayan P, Abbott LF. 2001. Theoretical neuroscience: computational and mathematical modeling of neural systems.

Desikan RS, Ségonne F, Fischl B, Quinn BT, Dickerson BC, Blacker D, Buckner RL,

Dale AM, Maguire RP, Hyman BT, Albert MS, Killiany RJ. 2006. An automated labeling system for subdividing the human cerebral cortex on MRI scans into gyral based regions of interest. Neuroimage 31:968–980.

Dick AS, Tremblay P. 2012. Beyond the arcuate fasciculus: Consensus and controversy in the connectional anatomy of language. Brain.

Donahue CJ, Sotiropoulos SN, Jbabdi S, Hernandez-Fernandez M, Behrens TE, Dyrby TB, Coalson T, Kennedy H, Knoblauch K, Van Essen DC, Glasser MF. 2016. Using Diffusion Tractography to

Predict Cortical Connection Strength and Distance: A Quantitative Comparison with Tracers in the Monkey. J Neurosci 36:6758–6770.

Dyrby TB, Søgaard L V., Parker GJ, Alexander DC, Lind NM, Baaré WFC, Hay-Schmidt A, Eriksen N, Pakkenberg B, Paulson OB, Jelsing J. 2007. Validation of in vitro probabilistic tractography. Neuroimage 37:1267–1277.

Eichert N, Verhagen L, Folloni D, Jbabdi S, Khrapitchev AA, Sibson NR, Mantini D, Sallet J, Mars RB. 2019. What is special about the human arcuate fasciculus? Lateralization, projections, and expansion. Cortex.

Ercsey-Ravasz M, Markov NT, Lamy C, VanEssen DC, Knoblauch K, Toroczkai Z, Kennedy H. 2013. A Predictive Network Model of Cerebral Cortical Connectivity Based on a Distance Rule. Neuron 80:184–197.

Felleman DJ, Van Essen DC. 1991. Distributed Hierarchical Processing in the Primate Cerebral Cortex. Cereb Cortex 1:1–47.

Fischl B. 2012. FreeSurfer. Neuroimage.

Fischl B, Sereno MI, Tootell RBH, Dale AM. 1999. High-resolution intersubject averaging and a coordinate system for the cortical surface. Hum Brain Mapp 8:272–284.

Fischl B, Van Der Kouwe A, Destrieux C, Halgren E, Ségonne F, Salat DH, Busa E, Seidman LJ, Goldstein J, Kennedy D, Caviness V, Makris N, Rosen B, Dale AM. 2004. Automatically Parcellating the Human Cerebral Cortex. Cereb Cortex 14:11–22.

Gershon RC, Wagster M V, Hendrie HC, Fox NA, Cook KF, Nowinski CJ. 2013. NIH toolbox for assessment of neurological and behavioral function. Neurology 80:S2–S6.

Glasser MF, Coalson TS, Robinson EC, Hacker CD, Harwell J, Yacoub E, Ugurbil K, Andersson J, Beckmann CF, Jenkinson M, Smith SM, Van Essen DC. 2016. A multi-modal parcellation of human cerebral cortex. Nature.

Glasser MF, Van Essen DC. 2011. Mapping Human Cortical Areas In Vivo Based on Myelin Content as Revealed by T1- and T2-Weighted MRI. J Neurosci 31:11597–11616.

Hagmann P, Cammoun L, Gigandet X, Meuli R, Honey CJ, Van Wedeen J, Sporns O. 2008. Mapping the structural core of human cerebral cortex. PLoS Biol 6:1479–1493.
Honey CJ, Sporns O, Cammoun L, Gigandet X, Thiran JP, Meuli R, Hagmann P. 2009. Predicting human resting-state functional connectivity from structural connectivity. Proc Natl Acad Sci U S A 106:2035–2040.

Humphries MD, Gurney K. 2008. Network "small-world-ness": A quantitative method for determining canonical network equivalence. PLoS One.

Jbabdi S, Lehman JF, Haber SN, Behrens TE. 2013. Human and monkey ventral prefrontal fibers use the same organizational principles to reach their targets: Tracing versus tractography. J Neurosci 33:3190–3201.

Jenkinson M, Beckmann CF, Behrens TEJ, Woolrich MW, Smith SM. 2012. FSL. Neuroimage 62:782–790.

Jeurissen B, Descoteaux M, Mori S, Leemans A. 2019. Diffusion MRI fiber tractography of the brain. NMR Biomed 32:1–22.
Ji JL, Spronk M, Kulkarni K, Repovš G, Anticevic A, Cole MW. 2019. Mapping the human brain's cortical-subcortical functional network organization. Neuroimage 185:35–57.

Larson-Prior LJ, Oostenveld R, Della Penna S, Michalareas G, Prior F, Babajani-Feremi A, Schoffelen JM, Marzetti L, de Pasquale F, Di Pompeo F, Stout J, Woolrich M, Luo Q, Bucholz R, Fries P, Pizzella V, Romani GL, Corbetta M, Snyder AZ. 2013. Adding dynamics to the Human Connectome Project with MEG. Neuroimage 80:190–201.

Latora V, Marchiori M. 2001. Efficient behavior of small-world networks. Phys Rev Lett.

Lebel C, Beaulieu C. 2011. Longitudinal development of human brain wiring continues from childhood into adulthood. J Neurosci 31:10937–10947.

Lennie P. 2003. The cost of cortical computation. Curr Biol 13:493–497.

Liewald D, Miller R, Logothetis N, Wagner HJ, Schüz A. 2014. Distribution of axon diameters in cortical white matter: an electron-microscopic study on three human brains and a macaque. Biol Cybern 108:541–557.

Maier-Hein KH, Neher PF, Houde JC, Côté MA, Garyfallidis E, Zhong J, Chamberland M, Yeh FC, Lin YC, Ji Q, Reddick WE, Glass JO, Chen DQ, Feng Y, Gao C, Wu Y, Ma J, Renjie H, Li Q, Westin CF, Deslauriers-Gauthier S, González JOO, Paquette M, St-Jean S, Girard G, Rheault F, Sidhu J, Tax CMW, Guo F, Mesri HY, Dávid S, Froeling M, Heemskerk AM, Leemans A, Boré A, Pinsard B, Bedetti C, Desrosiers M, Brambati S, Doyon J, Sarica A, Vasta R, Cerasa A, Quattrone A, Yeatman J, Khan AR, Hodges W, Alexander S, Romascano D, Barakovic M, Auría A, Esteban O, Lemkaddem A, Thiran JP, Cetingul HE, Odry BL, Mailhe B, Nadar MS, Pizzagalli F, Prasad G, Villalon-Reina JE, Galvis J, Thompson PM, Requejo FDS, Laguna PL, Lacerda LM, Barrett R, Dell'Acqua F, Catani M, Petit L, Caruyer E, Daducci A, Dyrby TB, Holland-Letz T, Hilgetag CC, Stieltjes B, Descoteaux M. 2017. The challenge of mapping the human connectome based on diffusion tractography. Nat Commun 8.

Marcus DS, Harwell J, Olsen T, Hodge M, Glasser MF, Prior F, Jenkinson M, Laumann T, Curtiss SW, Van Essen DC. 2011. Informatics and data mining tools and strategies for the human connectome project. Front Neuroinform 5:1–12.

Markov, Ercsey-Ravasz MM, Ribeiro Gomes AR, Lamy C, Magrou L, Vezoli J, Misery P, Falchier A, Quilodran R, Gariel MA. 2014. A weighted and directed interareal connectivity matrix for macaque cerebral cortex. Cereb cortex 24:17–36.

Markov NT, Ercsey-Ravasz M, Van Essen DC, Knoblauch K, Toroczkai Z, Kennedy H. 2013. Cortical High-Density Counterstream Architectures. Science 342:1238406–1238406.

Mori S, Oishi K, Jiang H, Jiang L, Li X, Akhter K, Hua K, Faria A V., Mahmood A, Woods R, Toga AW, Pike GB, Neto PR, Evans A, Zhang J, Huang H, Miller MI, van Zijl P, Mazziotta J. 2008. Stereotaxic white matter atlas based on diffusion tensor imaging in an ICBM template. Neuroimage 40:570–582.

Mount CW, Monje M. 2017. Wrapped to adapt: experience-dependent myelination. Neuron 95:743–756.

Muller L, Chavane F, Reynolds J, Sejnowski TJ. 2018. Cortical travelling waves: mechanisms and computational principles. Nat Rev Neurosci.

Newman MEJ. 2004. Fast algorithm for detecting community structure in networks. Phys Rev E 69:66133.

Newman MEJ. 2003. The structure and function of complex networks. SIAM Rev.

Panesar SS, Yeh F-C, Jacquesson T, Hula W, Fernandez-Miranda JC. 2018. A quantitative tractography study into the connectivity, segmentation and laterality of the human inferior longitudinal fasciculus. Front Neuroanat 12:47.

Roberts JA, Perry A, Lord AR, Roberts G, Mitchell PB, Smith RE, Calamante F, Breakspear M. 2016. The contribution of geometry to the human connectome. Neuroimage 124:379–393.

Roberts JA, Perry A, Roberts G, Mitchell PB, Breakspear M. 2017. Consistency-based thresholding of the human connectome. Neuroimage 145:118–129.

Romeo RR, Segaran J, Leonard JA, Robinson ST, West MR, Mackey AP, Yendiki A, Rowe ML, Gabrieli JDE. 2018. Language exposure relates to structural neural connectivity in childhood. J Neurosci 38:7870–7877.

Rubinov M, Sporns O. 2010. Complex network measures of brain connectivity: Uses and interpretations. Neuroimage.

Sarwar T, Ramamohanarao K, Zalesky A. 2019. Mapping connectomes with diffusion MRI: deterministic or probabilistic tractography? Magn Reson Med 81:1368–1384.

Sotiropoulos SN, Jbabdi S, Xu J, Andersson JL, Moeller S, Auerbach EJ, Glasser MF, Hernandez M, Sapiro G, Jenkinson M, Feinberg DA, Yacoub E, Lenglet C, Van Essen DC, Ugurbil K, Behrens TEJ. 2013. Advances in diffusion MRI acquisition and processing in the Human Connectome Project. Neuroimage 80:125–143.

Theodoni P, Majka P, Reser DH, Wójcik DK, Rosa MGP, Wang X-J. 2021. Structural Attributes and Principles of the Neocortical Connectome in the Marmoset Monkey. Cereb Cortex 32:15–28.

Trebaul L, Deman P, Tuyisenge V, Jedynak M, Hugues E, Rudrauf D, Bhattacharjee M, Tadel F, Chanteloup-Foret B, Saubat C, Reyes Mejia GC, Adam C, Nica A, Pail M, Dubeau F, Rheims S, Trébuchon A, Wang H, Liu S, Blauwblomme T, Garcés M, De Palma L, Valentin A, Metsähonkala EL, Petrescu AM, Landré E, Szurhaj W, Hirsch E, Valton L, Rocamora R, Schulze-Bonhage A, Mindruta I, Francione S, Maillard L, Taussig D, Kahane P, David O. 2018. Probabilistic functional tractography of the human cortex revisited. Neuroimage 181:414–429.

Van Essen DC, Smith SM, Barch DM, Behrens TEJ, Yacoub E, Ugurbil K. 2013. The WU-Minn Human Connectome Project: An overview. Neuroimage 80:62–79.

Van Essen DC, Ugurbil K. 2017. Components of the Human Connectome Project - Diffusion Tractography. https://www.humanconnectome.org/study/hcp-young-adult/project-protocol/diffusion-tractography

Ventura-Antunes L, Mota B, Herculano-Houzel S. 2013. Different scaling of white matter volume, cortical connectivity, and gyrification across rodent and primate brains. Front Neuroanat 7:1–12.

von Keyserlingk Graf D, Schramm U. 1984. Diameter of axons and thickness of myelin sheaths of the pyramidal tract fibres in the adult human medullary pyramid. Anat Anz 157:97–111.

Wang SSH, Shultz JR, Burish MJ, Harrison KH, Hof PR, Towns LC, Wagers MW,

Wyatt KD. 2008. Functional trade-offs in white matter axonal scaling. J Neurosci 28:4047–4056.

Watts DJ, Strogatz SH. 1998. Collective dynamics of 'small-world'networks. Nature 393:440.

Yeh FC, Panesar S, Fernandes D, Meola A, Yoshino M, Fernandez-Miranda JC, Vettel JM, Verstynen T. 2018. Population-averaged atlas of the macroscale human structural connectome and its network topology. Neuroimage 178:57–68.

Yeh FC, Verstynen TD, Wang Y, Fernández-Miranda JC, Tseng WYI. 2013. Deterministic diffusion fiber tracking improved by quantitative anisotropy. PLoS One 8:1–16.

Yoon JM, Benson NC, Forenzo D, Winawer J, Engel SA, Kay KN. 2019. Heritability of V1/V2/V3 surface area in the HCP 7T Retinotopy Dataset. J Vis 19:41b-41b.

Zalesky A, Fornito A, Cocchi L, Gollo LL, van den Heuvel MP, Breakspear M. 2016. Connectome sensitivity or specificity: which is more important? Neuroimage 142:407–420.

Zhang K, Sejnowski TJ. 2000. A universal scaling law between gray matter and white matter of cerebral cortex. Proc Natl Acad Sci U S A 97:5621–5626.

CHAPTER 2: AN ESTIMATION OF THE ABSOLUTE NUMBER OF AXONS INDICATES THAT HUMAN CORTICAL AREAS ARE SPARSELY CONNECTED

Abstract

The tracts between cortical areas are conceived as playing a central role in cortical information processing, but their actual numbers have never been determined in humans. Here we estimate the absolute number of axons linking cortical areas from a whole-cortex diffusion-MRI (dMRI) connectome, calibrated using the histologically-measured callosal fiber density. Median connectivity is estimated as ~6200 axons between cortical areas within-hemisphere and ~1300 axons inter-hemispherically, with axons connecting functionally-related areas surprisingly sparse. For example, we estimate that <5% of the axons in the trunk of the arcuate and superior longitudinal fasciculi connect Wernicke's and Broca's areas. These results suggest that detailed information is transmitted between cortical areas either via linkage of the dense local connections or via rare, extraordinarily privileged long-range connections.

Introduction

The major tracts connecting cortical areas have long been central to models of information-processing in the human brain (Geschwind, 1965). Such models have been refined and applied to development and disease with the advent of diffusion-MRI or dMRI (Assaf et al., 2019). However, dMRI only provides *relative* connectivity, not the absolute number of axons. Relative connectivity is very useful in many circumstances but more constraints would be possible if the absolute number of axons connecting different cortical areas could be estimated. Here we describe and apply a novel method for translating from dMRI-derived streamlines to axon counts.

The ratio between these two measures is obtained by comparing the number of streamlines pass through the corpus callosum to the number of axons, as measured with histology. The corpus callosum is uniquely well-suited for this purpose. Electron microscopy (EM) can be used to unambiguously count the total number of callosal axons because the limits of the callosum are well-defined, axons are aligned, and sections can be cut perpendicular to

their axis. Likewise, dMRI-derived streamlines can be unambiguously and exhaustively assigned to the callosum because the source and destination of all axons passing through the callosum as a whole are well-defined. In contrast to the ipsilateral fiber tracts, in which the majority of axons enter or leave the tract at point between the fascicular terminals, commissural axons must all be connecting the two hemispheres. Fortunately, despite these differences, the mean and variability of cross-sectional axon density of the corpus callosum is quite similar to that of telencephalic white matter in general (Aboitiz et al., 1992; Zikopoulos et al., 2018; Zikopoulos and Barbas, 2010), permitting the streamline:axon ratio calculated from callosal fiber to be applied to intra-hemispheric connections.

It has long been recognized that as the number of cortical neurons increases, maintaining the same probability of connectivity between neurons would require that axon number increase approximately with the square of neuron number, and this would require too much volume, impose an unsustainable metabolic load (Bullmore and Sporns, 2012), and actually decrease computational power due to conduction delays (Hofman, 2014). The consequent imperative to minimize long distance cortico-cortical fibers has been posited to be reflected in exponential decline in cortical connectivity with distance (Markov et al., 2013), and to be partially compensated for with a small-world graph architecture (Bassett and Bullmore, 2017), granting special properties to rare long-distance fibers in a log-normal neural physiology and anatomy (Buzsáki and Mizuseki, 2014). However, this organizing principle is rarely explicitly addressed in terms of individual axon counts, nor in a manner both granular and exhaustive with respect to cortical areas. In our histologically calibrated dMRI-derived estimation of this intercortical axon counts, we find that the widespread cortical integration implied by behavioral and mental coherence, and routinely observed in widespread physiological synchronization, belies a surprising small absolute number of long-range axons connecting cortical areas.

Materials and Methods

The basic principle of our method is very simple. Given a dMRI-based measure of total inter-hemispheric connectivity in arbitrary units and the physical number of axons traversing the

corpus callosum, the conversion factor between the two can be obtained by dividing the first by the second. Specifically, we started with the total inter-hemispheric tractography strength reported in our dMRI connectome of the Human Connectome Project (HCP) cohort (Rosen and Halgren, 2021). For each individual, the cross-sectional area of the corpus callosum was obtained using the standard FreeSurfer structural MRI pipeline (Fischl, 2012a). Multiplying this number by a histologically ascertained callosal fiber density (Aboitiz et al., 1992) yields an estimate of the number of axons traversing an individual's corpus callosum. Dividing this count by individuals' inter-hemispheric dMRI streamline value yields the conversion ratio from the arbitrarily-scaled dMRI metric to the absolute number of axons. Note that this procedure is independent from the scale of the dMRI metric, requiring only that it be proportional to the absolute number of fibers. A moderate proportionality has been observed in comparisons of dMRI and retrograde tracing in macaque (Donahue et al., 2016; van den Heuvel et al., 2015). Therefore, while the ratio itself is study-specific, the procedure can be applied to any dMRI tractography method or parameter set, provided that the dMRI method returns a continuous distribution of connectivity values and has reasonably similar sensitivity to callosal and ipsilateral fiber tracts. To demonstrate this, we repeated the analysis using data from an alternate tractography of the HCP cohort (Arnatkeviciute et al., 2021). Figure source data for all figures can be found at https://doi.org/10.5281/zenodo.6097026.

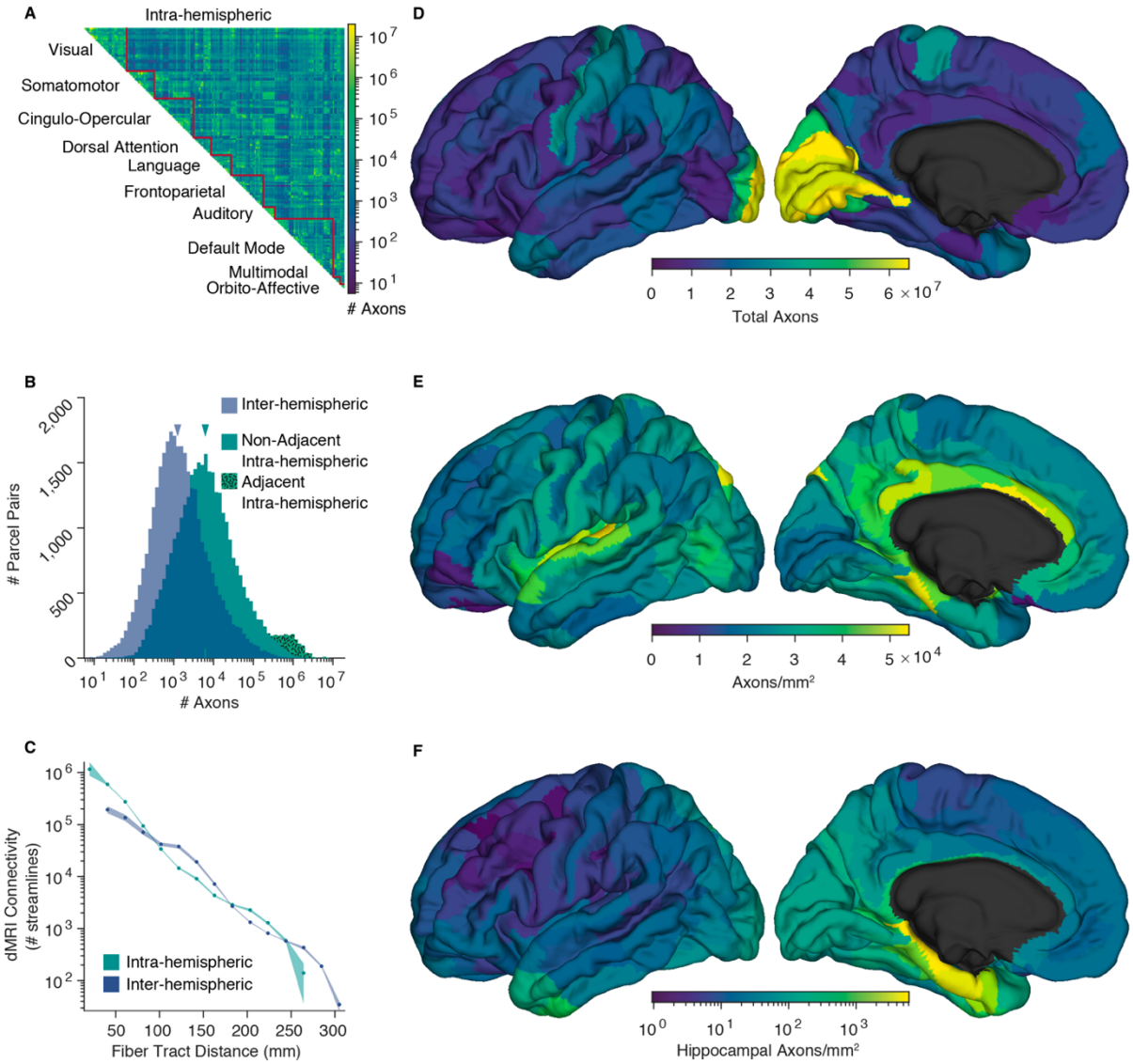

Figure 2.1 The number of axons estimated to interconnect the 360 cortical parcels of the HCP-MMP1.0 atlas. (A) Connectivity matrix of intra-hemispheric axon counts, averaged across the two hemispheres. Parcels are ordered into 10 functional networks. (B) Histograms showing the distribution of inter- and intra-hemispheric pairwise axon counts. Physically adjacent and non-adjacent parcel pair intra-hemispheric histograms are stacked. Median connectivity, indicated, is ~6,200 axons between cortical areas in the same hemisphere, and ~1,300 inter-hemispherically. (C) Comparison of intra- and inter-hemispheric dMRI connectivity as a function fiber tract distance. Pairwise values averaged within 15 fiber-length bins. Shading shows bootstrapped 95% confidence intervals. (D-F) axon counts and densities averaged across the two hemispheres and visualized on the left fsaverage template cortex (Fischl, 2012). (D) total axons connecting each parcel to all others. (E) axons connecting each parcel to all others, normalized by the reference parcel's area. (F) axons connecting the hippocampus to the rest of the cortex, normalized by the area of the cortical parcel, shown in log scale.

Results

Our previous dMRI study (Rosen and Halgren, 2021) includes estimated tractography streamlines between all 360 parcels of the HCP-MMP1.0 atlas (Glasser et al., 2016) for each of the 1,065 individuals in the HCP dMRI cohort. The sum connectivity between the 180 left hemisphere cortical parcels and the 180 right (180^2 parcel pairs) constitutes the total callosal connectivity, on average 1.25×10^8 streamlines. Based on our assumed fiber density of 3.7×10^5 axons/mm^2 (Aboitiz et al., 1992) and measured callosal cross-sectional area (mean = 689.45mm^2), we estimate this cohort to have 2.6×10^8 callosal fibers on average. The mean quotient between these two quantities is 2.00 axons-per-streamline, a ratio specific to the dMRI methodology and parameters used.

Applying the conversion factor to the inter-parcel connectivity from our prior study yields an estimate of the absolute number of axons connecting different cortical areas (Figure 2.1A), 2.43×10^9 axons in total. This implies that <22% of the ~11.5×10^9 cortical pyramidal cells (Azevedo et al., 2009; DeFelipe and Fariñas, 1992) project outside their parcel with the remainder being short-range horizontal or U-fibers. Furthermore, because 51% of inter-areal axons are to adjacent areas, <11% of pyramidal cells project beyond the adjacent parcel. Axons are approximately log-normally distributed among non-adjacent parcel pairs, with adjacent pairs having disproportionally high axon counts (Figure 2.1B). Median connectivity is ~6,200 axons between cortical areas in the same hemisphere, and ~1,300 inter-hemispherically. The number of axons in the median *inter*-hemispheric connection is ~20% of that in the median *intra*-hemispheric connection, similar to that found with histological tracing in macaques (Barbas et al., 2005). The number of callosal axons is not significantly affected by subject sex, though subjects ages 26-30 have slightly more inter-hemispheric axons than subjects ages 22-15. This sparse long-range connectivity is consistent with its exponential fall-off measured with dMRI in humans and histologically in other mammals (Markov et al., 2013; Rosen and Halgren, 2021) and with previous statistical estimates based on traditional neuroanatomy (Schüz and Braitenberg, 2002). In

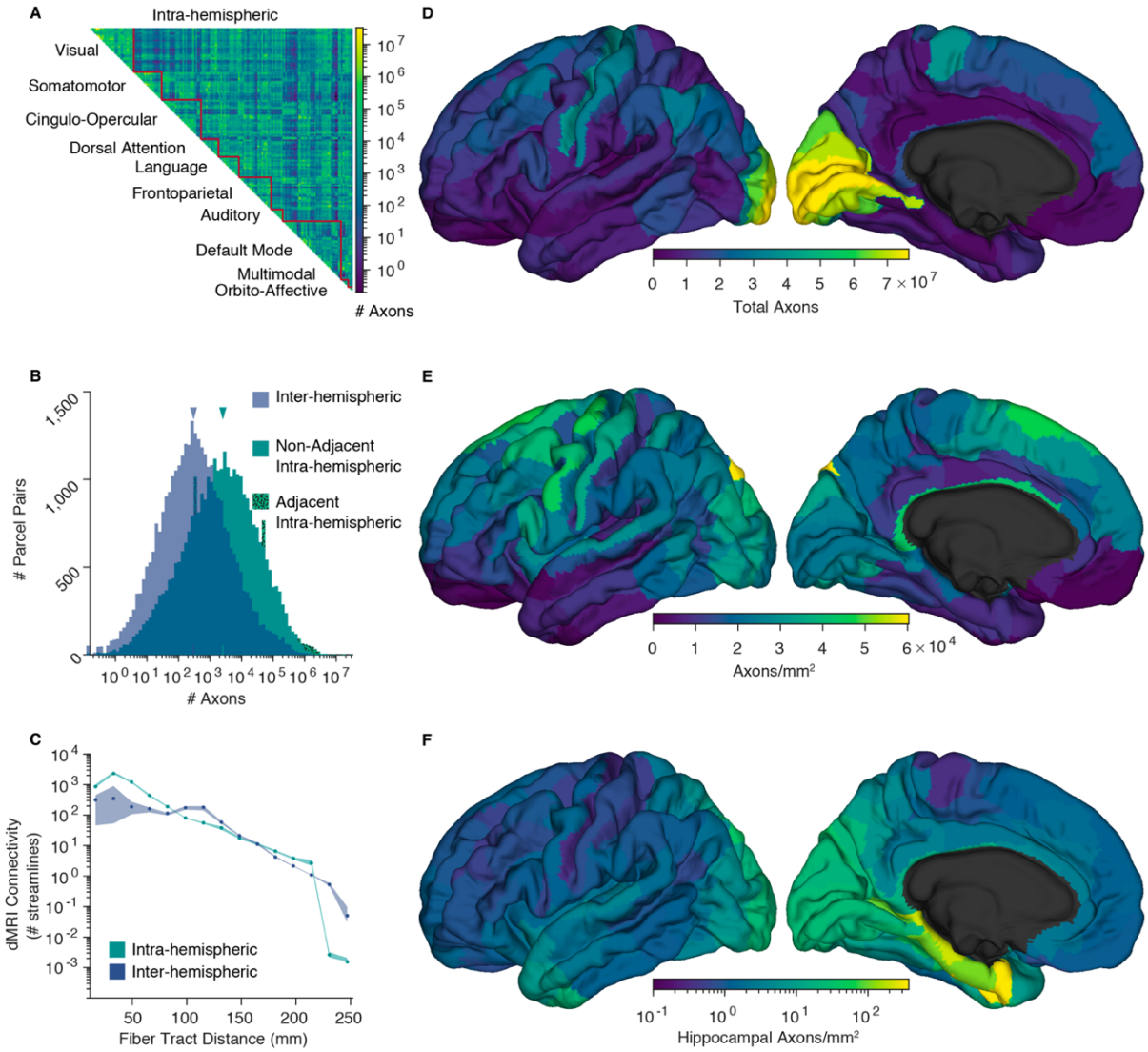

Figure 2.2 Replication results. Results obtained by repeating the analysis using an alternative tractography dataset (Arnatkeviciute et al., 2021) (A) Connectivity matrix of intra-hemispheric axon counts, averaged across the two hemispheres. Parcels are ordered into 10 functional networks. (B) Histograms showing the distribution of inter- and intra-hemispheric pairwise axon counts. Physically adjacent and non-adjacent parcel pair intra-hemispheric histograms are stacked. Median connectivity, shown in gray, is ~2,500 axons between cortical areas in the same hemisphere, and ~300 inter-hemispherically. Parcel pairs with zero axons connecting them are represented by the bars left of the y-axis. (C) dMRI connectivity as a function fiber tract distance. Pairwise values averaged within 15 fiber-length bins. Shading shows bootstrapped 95% confidence intervals. (D-F) axons counts and densities averaged across the two hemispheres and visualized on the left fsaverage template cortex (Fischl, 2012). (D) total axons connecting each parcel to all others. (E) axons connecting each parcel to all others, normalized by the reference parcel's area. (F) axons connecting the hippocampus to the rest of the cortex, normalized by the area of the cortical parcel, shown in log scale.

comparison to the number of axons that would be necessary for complete interconnectivity of neurons in different cortical areas with each other, the estimated number is ~10^{11} times smaller.

Our method requires that dMRI-tractography performs in a roughly similar manner when applied to intra- versus inter-hemispheric connections. We evaluated this similarity by comparing linear regressions of distance-matched log-transformed streamlines, and found no difference between the slope or intercept of inter- and intra-hemispheric connections (Figure 2.1C); within the common distance domain a paired r-test showed no difference in correlation, $p = 0.58$. The total count of a parcel's axons to or from all other areas is much less variable when normalized by the parcel's area (Figure 2.1D,E). Multiplying the total number of fibers by the effective fiber cross-sectional area (the inverse callosal packing density, 2.7×10^{-6} mm^2/axon) yields 6.6×10^3 mm^2 of cortex or 3.7% of the total white-gray interface. Note that the effective axonal area includes myelin, supporting cells and intercellular space in addition to the axon proper. The cross-sectional packing density of human prefrontal white matter is quite similar to callosal values with an average of 3.5×10^5 myelinated axons/mm^2 (Zikopoulos and Barbas, 2010) after correction for tissue shrinkage, and this varies among prefrontal regions by a less than factor of 2 (Zikopoulos et al., 2018). The percent of fiber-allocated cortical area is quite similar to the ~4% of total cortical fibers Schüz and Braitenberg estimated (Schüz and Braitenberg, 2002) are contained in the corpus callosum and long fascicles. The remaining ~95% of the cortical gray-white interface area is likely occupied by the short range U-fiber system which is difficult to assess with dMRI.

We estimated the fraction of axons traversing the entire length of the arcuate / superior lateral fasciculus (AF/SLF) between termination fields centered on Broca's and Wernicke's areas. The total number of AF/SLF axons was derived by multiplying the tracts' cross-sectional areas by mean axon density of ipsilateral tracts. Using published estimates of the cross-sectional areas of 160.6 mm^2 and 51.5 mm^2 for the left and right AF and 213.8 mm^2 and 174.4 for the left and right

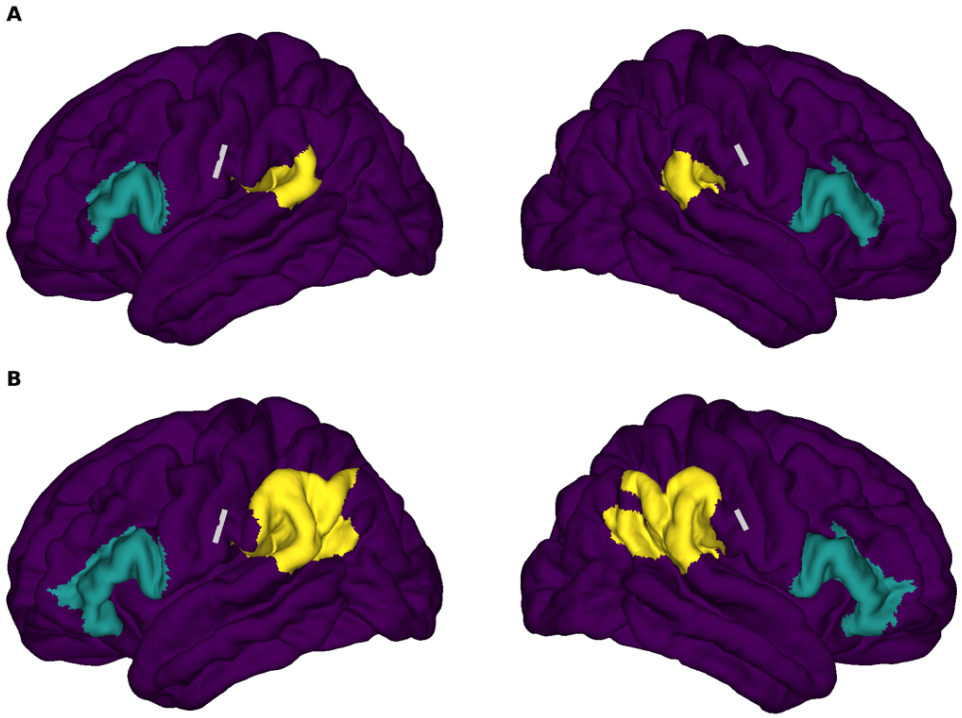

Figure 2.3 Arcuate / superior lateral fasciculus termination fields. In order to estimate the fraction of tract axons that travel the entire length of the tract, it's termination fields, centered on Broca's and Wernicke's areas, were manually defined in terms of HCP-MMP1.0 parcels according to consensus definitions (Tremblay et al., 2016). (A) Conservative definitions where the anterior termination field, in teal, is composed of parcels 44, 45, 6r, IFSa, IFSp, and FOP4 and the posterior termination field, in yellow, is composed of parcels PSL, RI, STV, and PFcm. For this definition trans-terminal axons account for 0.6% and 0.8% of tract axons in the left and right hemispheres. (B) Liberal definitions in which parcels 47l and p47r were added anteriorly and parcels PF, PFm, and PGi were added posteriorly, resulting in trans-terminal axons accounting for 1.9% and 2.9% of tract axons in the left and right hemispheres. Gray lines indicate the approximate locations at which the tract diameter, used to estimate the total number of tract axons were ascertained (Yeh, 2020).

SLF (Yeh, 2020), and a shrinkage-corrected axon density of $3.5x10^5$ axons/mm^2 (Zikopoulos and Barbas, 2010), yields a total of $1.3x10^8$ and $0.8x10^8$ axons in the left and right AF/SLF. These values were compared to the number of tractography-derived axons connecting AF/SLF termination fields (Glasser et al., 2016) according to consensus definitions from reference (Tremblay and Dick, 2016), see Figure 2.3. When the anterior termination field, centered on Broca's area is defined as HCP-MMP1.0 parcels 44, 45, 6r, IFSa, IFSp, and FOP4 and the posterior termination field, centered on Wernicke's area as parcels PSL, RI, STV, and PFcm, trans-terminal axons account for only 0.6% and 0.8% of tract axons in the left and right hemispheres. If the termination

fields are liberally expanded to also include parcels 47l and p47r in Broca's and parcels PF, PFm, and PGi in Wernicke's then these percentages increase to a still modest 1.9% and 2.9% of total tract axons. Please note that in this calculation all axons between Broca's and Wernicke's areas are assumed to pass through the AF/SLF; to the degree that some pass outside the AF/SLF, our estimates should be decreased.

The volume of hemispheric white matter (WM) occupied by axons between cortical parcels is equal to the sum of all axons' lengths multiplied by their cross-sectional areas. The mean fiber tract lengths of connections were taken from our prior dMRI analysis (Rosen and Halgren, 2021). For the effective cross-sectional area of axons we again assumed an effective cross-sectional area equivalent to the inverse of the callosal fiber density (Aboitiz et al., 1992). So calculated, the volume occupied by cortico-cortical and hippocampo-cortical fibers is $4.3x10^5$ mm^3, or about 96% of the total MRI-assessed WM volume. This implies that the number of long-range fibers cannot be larger than our estimate unless the axon density calculated from the corpus callosum histology is mistakenly low, but this is a linear effect that would need to be unrealistically inaccurate for it to change our main conclusions. Another possibility is that axon density was correctly measured for the corpus callosum but is higher for intra-hemispheric fibers *and* the number of axons per streamline is higher intra- than inter-hemispherically. These both need to be the case because there is no space available in the hemispheric white matter to contain more axons unless they are smaller. However, the histological data indicates that axonal density is approximately the same intra- and inter-hemispherically (Aboitiz et al., 1992; Zikopoulos and Barbas, 2010) and the comparison of distance-matched streamlines (Figure 2.1C). suggests that the number of axons per streamline intra- and inter-hemispherically is also approximately equal. The remaining WM volume may seem insufficient for connections with subcortical structures. However, the major subcortical structures known to communicate with the cortex

(thalamus, amygdala, striatum, nucleus basalis, locus coeruleus, etc.) contain, in sum, less than 1% of the number of cortical neurons (Arcelli et al., 1997; Avino et al., 2018; Xuereb et al., 1991). Even under the unlikely assumption that all excitatory thalamic neurons project to the cortex with a density across all cortical parcels proportionally to their area, their axons would only comprise ~4% of the total WM volume.

We conducted a series of simulations examining the consequences of possible errors in axonal packing density and axon-to-streamline ratio. As noted above, these parameters are co-constrained by the physical volume available for white matter. At our derived ratio and assumed packing density, the volume of inter-areal axons is just under the observed total white matter volume. Large net errors in the assumed packing density would result in total inter-areal axon volumes that are inconsistent with the hemispheric white matter volume, a value that is well established. Consequently, in our simulations, axonal packing density and axon-to-streamline ratio were reciprocally changed in order to maintain a constant total cerebral white matter volume. Since our parameter estimates are based primarily on fibers passing through the callosum, which are longer in general than intra-hemispheric fibers, parameter inaccuracies are more likely for short fibers. In order to evaluate the effect of such inaccuracies, we first simulated the effect of assuming that dMRI sensitivity is systematically reduced (and thus axon count underestimated) for shorter fibers. Uniformly doubling the number of axons with lengths < 40 mm in this way yields only a 37.5% increase in the total number of inter-areal axons, and because rank-order of observations is not altered the median axon counts are unchanged. Conceivably, our parameter estimates are accurate for the longest fibers (which tend to pass through the callosum) but are progressively less accurate for shorter inter-areal distances. Consequently, we simulated assuming that our packing density and dMRI sensitivity estimates at the longest fiber lengths were as in our base model, and then increased the dMRI streamline-to-axon ratio linearly as the fibers got shorter. Axon density was adjusted to maintain white matter volume constant. Even with unrealistically large systematic and matched errors in the two estimates, median inter-

areal axon count are only modestly increased. For example, adjustments resulting in twice the axon density and half the sensitivity of dMRI to axons at short inter-parcel distances increase the median number of inter-parcel axons by only ~36%. As reviewed below, errors in inter-areal axon count due to miss-estimation of axonal packing density are likely to be relatively unbiased with respect to inter-areal fiber length, and reported measures vary less than a factor of two. Our simulations indicate that such errors would have only marginal effects on the median number of inter-areal axons.

In order to demonstrate that the key principles and findings of this report are robust to the details of tractography procedure, we repeated our analysis on the tractography data of Arnatkeviciute and colleagues (Arnatkeviciute et al., 2021). These data consist of a 972 subject subset of the HCP cohort and use the same parcellation but a different method to reconstruct the fiber streamlines. These data contain fewer streamlines and the estimated numbers of axons per connection are broadly comparable, being somewhat fewer but within an order of magnitude of our primary estimate with medians of ~1100 and ~130 axons for pairwise intra- and inter-hemispheric connections between cortical areas (Figure 2.2), i.e., even more sparse than those calculated from our tractography data. These data confirm that, independent of tractography procedure, cortical areas are sparsely connected.

Discussion

In this study we estimated the absolute number of axons interconnecting cortical areas by calibrating dMRI-based tractography using the histologically ascertained cross-sectional fiber density of the corpus callosum and found that long-range cortico-cortical connections are quite sparse. Our method depends on histological estimates of callosal axon packing density and leverages the unique properties of the callosum. It assumes proportionality between the number of axons connecting two areas and the number of dMRI tractography streamlines for the areal pair, and it assumes approximate parity between dMRI sensitivity to inter- and intra-hemispheric connections. In order to estimate the volume occupied by inter-parcel cortico-cortical

connections, we make the further assumption that the effective axonal packing density is reasonably uniform across the hemispheric white matter.

Although there are few reports of axonal density in the corpus callosum (Aboitiz et al., 1992; Liewald et al., 2014), they are consistent with each other and with reports of axonal density of intra-hemispheric tracts (Zikopoulos and Barbas, 2010). Our study relies on the data reported by Aboitiz et al. (Aboitiz et al., 1992), because it is the most systematic count of which we are aware. There is a later study, (Liewald et al., 2014), which provides a value only slightly lower, $2.83x10^5$ vs $3.7x10^5$ axons/mm^2 after correction for tissue shrinkage (Schüz and Palm, 1989). However, since this later study was primarily a survey of axon diameter with packing density only incidentally recorded, it is conceivable that density values derived from could be small underestimates. Mis-estimated tissue shrinkage is possible but likely to be <10% and callosal areas were measured with a well-validated and widely-used in vivo method (Fischl, 2012a). The axon count estimate does not require that the packing densities of the corpus callosum and ipsilateral white matter be the same, but rather the lesser assumption that the axon to dMRI streamline ratio be reasonably uniform across the various instances of long distance cortico-cortical connectivity. However, if the packing densities of ipsilateral and callosal long distance connections are also similar then the total hemispheric white matter volume provides an absolute constraint on the number of long distance connections, and this provides a powerful validation of our estimate.

The literature provides converging evidence that the fiber packing density of white matter varies by at most a factor of 2 across the cortex, including the corpus callosum. A histological study of human cortex found only a 7% difference in the axon densities of the callosum versus the superior longitudinal and inferior occipitofrontal fasciculi (Liewald et al., 2014). Zikopolous and Barbas (Zikopoulos and Barbas, 2010) found that the cross-sectional packing density of human prefrontal white matter is remarkably similar to callosal values with an average of $3.5x10^5$ myelinated axons/mm^2 after correction for tissue shrinkage and that this

varies among prefrontal regions by a less than factor of 2 (Zikopoulos et al., 2018). In addition, while dMRI-based estimates of axon density and caliber are imperfect, they suggest that axon density varies by less than 2-fold both between major ipsilateral tracts and within each tract along their length (De Santis et al., 2014). While packing density is not directly equivalent to axon caliber, the two are likely inversely related. Axon diameter, as estimated with dMRI, varies by 20% among ipsilateral tracts and by at most a factor of 2.2 among white matter voxels, including those of the corpus callosum (Fan et al., 2020; Huang et al., 2020). Overall, distributions of dMRI-derived axon diameter for the callosum (Horowitz et al., 2015) and whole cerebrum (Fan et al., 2020) are similar with the bulk of values between 2.5 and 5 μm. Histological measurements in macaques concur that axon diameters are very similar within the callosal and non-callosal segments of major fasciculi and vary by less than 2-fold across the cortex (Tomasi et al., 2012). Furthermore, even this limited variation in diameter is not systematically dependent on the length of axons but rather on their regions of origin and termination (Innocenti et al., 2014).

Concerning dMRI- to-axon-count proportionality, it has been shown that there is a moderate linear correlation between dMRI-traced streamlines and the number of fibers identified with histological tracers connecting cortical regions in macaques (Donahue et al., 2016; van den Heuvel et al., 2015) and a strong correlation in ferrets (Delettre et al., 2019). Based on these data, Donahue and colleagues (Donahue et al., 2016) concluded that dMRI tractography was capable of quantitively describing cortico-cortical white matter tracts with approximately order-of-magnitude precision using a high-quality dataset such as the HCP. In line with previous statistical estimates of whole-cortex axon counts based on traditional neuroanatomy (Schüz and Braitenberg, 2002), the numbers of axons in pairwise connections are probably correct within an order of magnitude. Estimates of this precision are useful as we find that that inter-areal connectivity derived from dMRI varies over more than seven orders of magnitude.

While we derive a single dMRI-to-axon count factor, it is likely that the true conversion ratio varies somewhat among connections due to local microstructural differences other than axon count such as axon caliber, packing density, or myelination. However, the major fasciculi (including the corpus callosum) have similar axon calibers and packing densities, varying by only a factor of ~2 across the cortex when examined in humans histologically (Liewald et al., 2014; Zikopoulos et al., 2018; Zikopoulos and Barbas, 2010) or with dMRI (De Santis et al., 2014; Fan et al., 2020; Huang et al., 2020) and histologically in macaques (Tomasi et al., 2012). More generally, packing density is a function of local cellular interactions, especially with oligodendrocytes, and because these are the same in the corpus callosum and intra-hemispheric white matter, the *a priori* expectation is that packing density would be similar, as histological data supports. Myelination has only a modulatory effect on dMRI-detected anisotropy, with most of the effect derived from axonal membranes (Beaulieu, 2002). Nevertheless, microstructural variation in dMRI-to-axon count ratio may be a source of noise in our estimates. Our simulations of miss-estimation of dMRI-to-axon ratio and packing density show that these errors only marginally affect estimated axon counts and do not alter our conclusions. Our findings were also similar when we repeated our analysis on an alternative, somewhat sparser dMRI tractography dataset (Arnatkeviciute et al., 2021), demonstrating that the details of the tractography algorithm do not affect the overall tenor of our results. While the scope of this study is limited to long-range fibers, we note that shorter, more superficial U-fibers are systematically less myelinated and of lesser caliber than their inter-areal counterparts (Zikopoulos et al., 2018) and therefore the procedure outlined here may require modification before being applied to them.

As previously stated, this methodology assumes a reasonable degree of parity in the sensitivity of the dMRI tractography to intra- and inter-hemispheric fiber tracts. Consistent with this assumption, we found little difference between distance-matched dMRI connectivity for callosal versus ipsilateral connections. If callosal axons were more easily detectable, this would

be reflected as an upward displacement of the inter-hemispheric trace (blue) above the intra-hemispheric trace (green) across the entire distance domain in Figure 2.1C, which is not evident. This parity is perhaps unsurprising because over most of their trajectories, inter-hemispheric fibers are subjected to the same crossing fiber issues as intra-hemispheric. Specifically, the corpus callosum is a distinct tract for only about 15-35 mm, but its fibers range in length up to about 300 mm. Thus, the fraction of an inter-hemispheric tract that resides within the callosum is inversely proportional to its total length. Consequently, if there were enhanced detection of callosal fibers as streamlines by dMRI, one would expect the inter-hemispheric (blue) trace in Figure 2.1C to be elevated primarily at short fiber lengths and depressed at long fiber lengths, resulting in a noticeably steeper slope for the inter-hemispheric than the intra-hemispheric trace, which is not observed. These data support the applicability of the scaling factor derived from inter-hemispheric fibers to intra-hemispheric fibers.

The corpus callosum was used to calibrate the estimate because of its unique properties: it has a well-defined cross-sectional area, more than ~99% of inter-hemispheric cortico-cortical axons are routed through it (Aboitiz et al., 1992; Highley et al., 1999), and essentially no fibers leave or enter the tract between the two hemispheres. This is in sharp contrast to non-commissural fasciculi. While it may be commonly assumed that within major cortical fasciculi the majority of axons terminate or originate at the ends of the tract and thus carry information along its entire length, an alternative conception is that these large bundles are composed mostly of axons shorter than the total fascicular length which enter and exit the tract at various points. By analogy, the former assumption likens a tract to a tunnel, where all traffic is trans-terminal, whereas the latter conceives of tracts as like interstate highways, where very few vehicles travel the entire route. In a supplementary analysis we compared these models for the arcuate / superior lateral fascicular (AF/SLF) system. The total number of AF/SLF axons was estimated using the tract diameters (Yeh, 2020) and packing densities (Zikopoulos and Barbas, 2010) taken from the literature. The number of trans-terminal axons was determined by defining termination field

parcels centered on restricted and inclusive definitions of Broca's and Wernicke's areas (Tremblay and Dick, 2016). Depending on the assumptions, only about 1-5% of the axons in a middle section of these fasciculi are trans-terminal. These percentages may be over-estimates since they assume that all fibers between the posterior and anterior areas travel through the AF/SLF. However, even if these values are a 2-fold underestimate, it suggests that only a small fraction of the axons in the ipsilateral fasciculi are trans-terminal. The evidence indicates that the 'highway' model is more apt for the ipsilateral fiber tracts and this conception is consistent with neural wiring being driven, in large part, by exponential distance rules (Markov et al., 2013). This of course, does not apply to the corpus callosum, as there is no inter-terminal cortex to project into.

Importantly, the reconceptualization of major intra-hemispheric tracts as containing few fibers connecting their distant terminals is still consistent with the long- and well-established impression from blunt dissection (Schmahmann and Pandya, 2007) and dMRI orientation maps (Hagler et al., 2009) that the hemispheric white matter is largely composed of well-defined long-distance tracts. Indeed, we estimate that ~96% of the white matter is composed of inter-areal axons. What these observations suggest is that the major tracts arise from the tendency of axons to grow in alignment with axons which are already present using established mechanisms of adhesion and fasciculation (Spead and Poulain, 2020). Thus axons are free to join tracts at various points, and tend to proceed together (fasciculate), but again are free to leave whenever they approach their own target. In other words, axons are joined in a given tract because they share a direction rather than an origin and destination.

The inter-areal axon counts we derive here permit other interesting quantitative estimates which may inform models of cortical neurophysiology. For example, the connections between Wernicke's and Broca's areas are thought to integrate receptive and expressive aspects of language, but we estimate that there are only ~58,000 axons between the core cortical parcels in these regions (parcels 44 and PSL), fewer than two for each word in an average university

student's vocabulary (Brysbaert et al., 2016). Another example where quantitative appreciation of direct axonal connections may influence neuro-cognitive models are the hippocampo-cortical interactions subserving recent memory, which are commonly posited to carry information regarding the contents of the memory trace during memory formation, consolidation and retrieval. We estimated that areas distant from the hippocampus, notably the dorsolateral prefrontal cortex, may be connected to it by <10 axons/mm^2 (Figure 2.1F) including both efferent and afferent axons, yet hippocampo-prefrontal interactions are considered crucial for contextual recall (Jin and Maren, 2015). We estimated the average neural density in the cortex as ~92,300 neurons/mm^2 by dividing the $16.34x10^9$ cortical neurons (including interneurons) from (Azevedo et al., 2009) by the $1.77x10^5$ mm^2 mean white—gray surface area of the HCP cohort used. If the sparse connectivity suggested by our calculations is correct, it implies that hippocampo-dorsolateral prefrontal interactions in memory are likely mediated by polysynaptic pathways.

These constraints encourage consideration of models of cortical function where connections are dense but mainly local, i.e. a small world network with intense interconnections within modules and sparse projections between them. While this general principle is widely accepted, the scale of the vast gulf in absolute connectivity between local and long-range connections is startling. This network architecture provides for the wide and efficient distribution of information created by local processing within modules (Bassett and Bullmore, 2017; Markov et al., 2013). A more uniformly connected cortex would require more white matter, necessitating a more voluminous cerebrum and the human cortex is near the limit after which an increase in size reduces computational power (Bullmore and Sporns, 2012; Hofman, 2014). Functionally, a deep reservoir of weak connections enables a large number of states and eases state transitions (Buzsáki and Mizuseki, 2014). Modeling suggests that long range covariance and even synchrony can be achieved through activation of multi-synaptic pathways rather than direct connections

(Bazhenov et al., 2008; Vicente et al., 2008), and possible signs of these have been observed experimentally in humans (Dickey et al., 2022; Mak-McCully et al., 2014).

While the long-range direct cortico-cortical axons are few in number, we note that axons are heterogeneous and that these counts are a limited proxy for true inter-areal connectivity. Axons, especially those connecting architectonically similar regions, may have a disproportionate impact on the flow of information despite their rarity (Aboitiz et al., 2003; Beul et al., 2017; Deco et al., 2021), by virtue of their morphology (e.g. greater diameter, larger termination fields, greater axonal arborization, or more numerous *en passant* varicosities) or by molecular synaptic specializations. For example, while only ~5% of the synapses to V1 layer 4 come from the lateral geniculate body in the macaque (Peters et al., 1994), they have an outsized effect on their firing (Chung and Ferster, 1998). The importance of rare inter-module connections might also be enhanced if they are focused on a small location within cortical parcels (i.e. the rich club (Van Den Heuvel and Sporns, 2011)), but this has not been convincingly demonstrated. Lastly, it is useful to note that these quantitative considerations are radically different in other species, where the smaller number of cortical neurons and shorter inter-areal distances allow greater connectivity between cortical areas, as well as a larger proportion of subcortical connectivity (Hofman, 2014).

Acknowledgements

This work was supported by National Institute of Mental Health Grant 1RF1MH117155. Data were provided, in part, by the Human Connectome Project, WU-Minn Consortium (Principal Investigators: David Van Essen and Kamil Ugurbil; 1U54MH091657) funded by the 16 National Institutes of Health (NIH) Institutes and Centers that support the NIH Blueprint for Neuroscience Research; and by the McDonnell Center for Systems Neuroscience at Washington University.

Chapter 2, in full, is a reprint of the material as it appears in Rosen BQ, Halgren E. 2022. An estimation of the absolute number of axons indicates that human cortical areas a sparsely connected. *PLOS Biol*, 20 (3) e3001575. The dissertation author was the primary investigator and author of this paper.

References

Aboitiz F, López J, Montiel J. 2003. Long distance communication in the human brain: timing constraints for inter-hemispheric synchrony and the origin of brain lateralization. Biol Res 36:89–99.

Aboitiz F, Scheibel AB, Fisher RS, Zaidel E. 1992. Fiber composition of the human corpus callosum. Brain Res 598:143–153.

Arcelli P, Frassoni C, Regondi MC, De Biasi S, Spreafico R. 1997. GABAergic neurons in mammalian thalamus: a marker of thalamic complexity? Brain Res Bull 42:27–37.

Arnatkeviciute A, Fulcher BD, Oldham S, Tiego J, Paquola C, Gerring Z, Aquino K, Hawi Z, Johnson B, Ball G, Klein M, Deco G, Franke B, Bellgrove MA, Fornito A. 2021. Genetic influences on hub connectivity of the human connectome. Nat Commun 12:4237.

Assaf Y, Johansen-Berg H, Thiebaut de Schotten M. 2019. The role of diffusion MRI in neuroscience. NMR Biomed 32:e3762.

Avino TA, Barger N, Vargas M V, Carlson EL, Amaral DG, Bauman MD, Schumann CM. 2018. Neuron numbers increase in the human amygdala from birth to adulthood, but not in autism. Proc Natl Acad Sci 115:3710–3715.

Azevedo FAC, Carvalho LRB, Grinberg LT, Farfel JM, Ferretti REL, Leite REP, Filho WJ, Lent R, Herculano-Houzel S. 2009. Equal numbers of neuronal and nonneuronal cells make the human brain an isometrically scaled-up primate brain. J Comp Neurol 513:532–541.

Baker KG, Halliday GM, Hornung J-P, Geffen LB, Cotton RGH. 1991. Distribution, morphology and number of monoamine-synthesizing and substance P-containing neurons in the human dorsal raphe nucleus. Neuroscience 42:757–775.

Barbas H, Hilgetag CC, Saha S, Dermon CR, Suski JL. 2005. Parallel organization of contralateral and ipsilateral prefrontal cortical projections in the rhesus monkey. BMC Neurosci 6:32.

Bassett DS, Bullmore ET. 2017. Small-world brain networks revisited. Neurosci 23:499–516.

Bazhenov M, Rulkov NF, Timofeev I. 2008. Effect of synaptic connectivity on long-range synchronization of fast cortical oscillations. J Neurophysiol 100:1562–1575.

Beaulieu C. 2002. The basis of anisotropic water diffusion in the nervous system – a technical review. NMR Biomed 15:435–455.

Beckmann H, Lauer M. 1997. The human striatum in schizophrenia. II. Increased number of striatal neurons in schizophrenics. Psychiatry Res Neuroimaging 68:99–109.

Behrens TEJ, Berg HJ, Jbabdi S, Rushworth MFS, Woolrich MW. 2007. Probabilistic diffusion tractography with multiple fibre orientations: What can we gain? Neuroimage 34:144–155.
Beul SF, Barbas H, Hilgetag CC. 2017. A Predictive Structural Model of the Primate Connectome. Sci Rep 7:1–12.

Blinkov SM, Glezer II. 1968. The human brain in figures and tables: a quantitative handbook. Basic Books.

Brysbaert M, Stevens M, Mandera P, Keuleers E. 2016. How Many Words Do We Know? Practical Estimates of Vocabulary Size Dependent on Word Definition, the Degree of Language Input and the Participant's Age. Front Psychol.

Bullmore E, Sporns O. 2012. The economy of brain network organization. Nat Rev Neurosci 13:336–349.

Buzsáki G, Mizuseki K. 2014. The log-dynamic brain: how skewed distributions affect network operations. Nat Rev Neurosci 15:264–278.

Chung S, Ferster D. 1998. Strength and orientation tuning of the thalamic input to simple cells revealed by electrically evoked cortical suppression. Neuron 20:1177–1189.

De Santis S, Drakesmith M, Bells S, Assaf Y, Jones DK. 2014. Why diffusion tensor MRI does well only some of the time: variance and covariance of white matter tissue microstructure attributes in the living human brain. Neuroimage 89:35–44.

Deco G, Sanz Perl Y, Vuust P, Tagliazucchi E, Kennedy H, Kringelbach ML. 2021. Rare long-range cortical connections enhance human information processing. Curr Biol 31:4436-4448.e5.

DeFelipe J, Fariñas I. 1992. The pyramidal neuron of the cerebral cortex: Morphological and chemical characteristics of the synaptic inputs. Prog Neurobiol 39:563–607.

Delettre C, Messé A, Dell L-A, Foubet O, Heuer K, Larrat B, Meriaux S, Mangin J-F, Reillo I, de Juan Romero C, Borrell V, Toro R, Hilgetag CC. 2019. Comparison between diffusion MRI tractography and histological tract-tracing of cortico-cortical structural connectivity in the ferret brain. Netw Neurosci 3:1038–1050.

Dickey CW, Verzhbinsky IA, Jiang X, Rosen BQ, Kajfez S, Stedelin B, Shih JJ, Ben-Haim S, Raslan AM, Eskandar EN, Gonzalez-Martinez J, Cash SS, Halgren E. 2022. Widespread ripples synchronize human cortical activity during sleep, waking, and memory recall. Proc Natl Acad Sci 119:e2107797119.

Donahue CJ, Sotiropoulos SN, Jbabdi S, Hernandez-Fernandez M, Behrens TE, Dyrby TB, Coalson T, Kennedy H, Knoblauch K, Van Essen DC, Glasser MF. 2016. Using Diffusion Tractography to Predict Cortical Connection Strength and Distance: A Quantitative Comparison with Tracers in the Monkey. J Neurosci 36:6758–6770.

Eriksen N, Stark AK, Pakkenberg B. 2009. Age and Parkinson's disease-related neuronal death in the substantia nigra pars compacta. Birth, life death dopaminergic neurons Subst Nigra 203–213.

Fan Q, Nummenmaa A, Witzel T, Ohringer N, Tian Q, Setsompop K, Klawiter EC, Rosen BR, Wald LL, Huang SY. 2020. Axon diameter index estimation independent of fiber orientation distribution using high-gradient diffusion MRI. Neuroimage 222:117197.

Fischl B. 2012. FreeSurfer. Neuroimage 62:774–781.

Geschwind N. 1965. Disconnexion syndromes in animals and man. Brain 88:237–294.

Glasser MF, Coalson TS, Robinson EC, Hacker CD, Harwell J, Yacoub E, Ugurbil K, Andersson J, Beckmann CF, Jenkinson M, Smith SM, Van Essen DC. 2016. A multi-modal parcellation of human cerebral cortex. Nature 536:171–8.

Hagler DJ, Ahmadi ME, Kuperman J, Holland D, McDonald CR, Halgren E, Dale AM. 2009. Automated white-matter tractography using a probabilistic diffusion tensor atlas: Application to temporal lobe epilepsy. Hum Brain Mapp 30:1535–1547.

Highley JR, Esiri MM, McDonald B, Roberts HC, Walker MA, Crow TJ. 1999. The size and fiber composition of the anterior commissure with respect to gender and schizophrenia. Biol Psychiatry 45:1120–1127.

Hofman MA. 2014. Evolution of the human brain: when bigger is better. Front Neuroanat 8:15.
Horowitz A, Barazany D, Tavor I, Bernstein M, Yovel G, Assaf Y. 2015. In vivo correlation between axon diameter and conduction velocity in the human brain. Brain Struct Funct 220:1777–1788.

Huang SY, Tian Q, Fan Q, Witzel T, Wichtmann B, McNab JA, Daniel Bireley J, Machado N, Klawiter EC, Mekkaoui C, Wald LL, Nummenmaa A. 2020. High-gradient diffusion MRI reveals distinct estimates of axon diameter index within different white matter tracts in the in vivo human brain. Brain Struct Funct 225:1277–1291.

Innocenti GM, Vercelli A, Caminiti R. 2014. The Diameter of Cortical Axons Depends Both on the Area of Origin and Target. Cereb Cortex 24:2178–2188.
Jenkinson M, Beckmann CF, Behrens TEJ, Woolrich MW, Smith SM. 2012. FSL. Neuroimage 62:782–790.

Ji JL, Spronk M, Kulkarni K, Repovš G, Anticevic A, Cole MW. 2019. Mapping the human brain's cortical-subcortical functional network organization. Neuroimage 185:35–57.

Jin J, Maren S. 2015. Prefrontal-Hippocampal Interactions in Memory and Emotion. Front Syst Neurosci.
Liewald D, Miller R, Logothetis N, Wagner HJ, Schüz A. 2014. Distribution of axon diameters in cortical white matter: an electron-microscopic study on three human brains and a macaque. Biol Cybern 108:541–557.

Mak-McCully RA, Deiss SR, Rosen BQ, Jung KY, Sejnowski TJ, Bastuji H, Rey M, Cash SS, Bazhenov M, Halgren E. 2014. Synchronization of Isolated Downstates (K-Complexes) May Be Caused by Cortically-Induced Disruption of Thalamic Spindling. PLoS Comput Biol 10.

Markov NT, Ercsey-Ravasz M, Van Essen DC, Knoblauch K, Toroczkai Z, Kennedy H. 2013. Cortical high-density counterstream architectures. Science.

Meyer M, Desbrun M, Schröder P, Barr AH. 2003. Discrete Differential-Geometry Operators for Triangulated 2-Manifolds. pp. 35–57.

Mouton PR, Pakkenberg B, Gundersen HJG, Price DL. 1994. Absolute number and size of pigmented locus coeruleus neurons in young and aged individuals. J Chem Neuroanat 7:185–190.

Mufson EJ, Ginsberg SD, Ikonomovic MD, DeKosky ST. 2003. Human cholinergic basal forebrain: chemoanatomy and neurologic dysfunction. J Chem Neuroanat 26:233–242.

Peters A, Payne BR, Budd J. 1994. A numerical analysis of the geniculocortical input to striate cortex in the monkey. Cereb Cortex 4:215–229.

Rivara C, Sherwood CC, Bouras C, Hof PR. 2003. Stereologic characterization and spatial distribution patterns of Betz cells in the human primary motor cortex. Anat Rec Part A Discov Mol Cell Evol Biol An Off Publ Am Assoc Anat 270:137–151.

Rosen BQ, Halgren E. 2021. A whole-cortex probabilistic diffusion tractography connectome. eNeuro 8.

Schmahmann JD, Pandya DN. 2007. Cerebral White Matter — Historical Evolution of Facts and Notions Concerning the Organization of the Fiber Pathways of the Brain. J Hist Neurosci 16:237–267.

Schüz A, Braitenberg V. 2002. The human cortical white matter: quantitative aspects of cortico-cortical long-range connectivity. Cortical areas Unity Divers 377–385.

Schüz A, Palm G. 1989. Density of neurons and synapses in the cerebral cortex of the mouse. J Comp Neurol 286:442–455.

Spead O, Poulain FE. 2020. Trans-axonal signaling in neural circuit wiring. Int J Mol Sci 21:5170.

Tomasi S, Caminiti R, Innocenti GM. 2012. Areal differences in diameter and length of corticofugal projections. Cereb Cortex 22:1463–1472.
Tournier JD, Calamante F, Connelly A. 2010. Improved probabilistic streamlines tractography by 2nd order integration over fibre orientation. distributions Proceedings of the International Society for Magnetic Resonance in Medicine. New Jersey, USA: John Wiley & Sons, Inc.

Tournier JD, Smith R, Raffelt D, Tabbara R, Dhollander T, Pietsch M, Christiaens D, Jeurissen B, Yeh CH, Connelly A. 2019. MRtrix3: A fast, flexible and open software framework for medical image processing and visualisation. Neuroimage 202:116137.

Tremblay P, Dick AS. 2016. Broca and Wernicke are dead, or moving past the classic model of language neurobiology. Brain Lang 162:60–71.

Van den Heuvel MP, de Reus MA, Feldman Barrett L, Scholtens LH, Coopmans FMT, Schmidt R, Preuss TM, Rilling JK, Li L. 2015. Comparison of diffusion tractography and tract-tracing measures of connectivity strength in rhesus macaque connectome. Hum Brain Mapp 36:3064–3075.

Van Den Heuvel MP, Sporns O. 2011. Rich-club organization of the human connectome. J Neurosci 31:15775–15786.

Van Essen DC, Smith SM, Barch DM, Behrens TEJ, Yacoub E, Ugurbil K. 2013. The WU-Minn Human Connectome Project: An overview. Neuroimage 80:62–79.

Vicente R, Gollo LL, Mirasso CR, Fischer I, Pipa G. 2008. Dynamical relaying can yield zero time lag neuronal synchrony despite long conduction delays. Proc Natl Acad Sci 105:17157–17162.

von Bartheld CS, Bahney J, Herculano-Houzel S. 2016. The search for true numbers of neurons and glial cells in the human brain: A review of 150 years of cell counting. J Comp Neurol 524:3865–3895.

Wada A, Goto J, Goto N, Kawamura N, Matsumoto K. 2001. Are There One Million Nerve Fibres in the Human Medullary Pyramid? Okajimas Folia Anat Jpn 77:221–224.

Wegiel Jarek, Flory M, Kaczmarski W, Brown WT, Chadman K, Wisniewski T, Nowicki K, Kuchna I, Ma SY, Wegiel Jerzy. 2017. Partial Agenesis and Hypoplasia of the Corpus Callosum in Idiopathic Autism. J Neuropathol Exp Neurol 76:225–237.

Williams EJ. 1959. The comparison of regression variables. J R Stat Soc Ser B 21:396–399.

Xuereb JH, Perry RH, Candy JM, Perry EK, Bonham JR. 1991. Nerve cell Loss in the thalamus in Alzheimer's disease and Parkinson's disease. Brain 114:1363–1379.

Yeh F-C. 2020. Shape analysis of the human association pathways. Neuroimage 223:117329.

Zikopoulos B, Barbas H. 2010. Changes in prefrontal axons may disrupt the network in autism. J Neurosci 30:14595–14609.

Zikopoulos B, García-Cabezas MÁ, Barbas H. 2018. Parallel trends in cortical gray and white matter architecture and connections in primates allow fine study of pathways in humans and reveal network disruptions in autism. PLoS Biol 16:e2004559.

CHAPTER 3: SIMULATING HUMAN SLEEP EEG AND MEG FROM ION CHANNEL AND CIRCUIT LEVEL DYNAMICS

Abstract

Although they form a unitary phenomenon, the relationship between extracranial M/EEG and transmembrane ion flows is understood only as a general principle rather than as a well-articulated and quantified causal chain. We present an integrated multiscale model, consisting of a neural simulation of thalamus and cortex during stage N2 sleep and a biophysical model projecting cortical current densities to M/EEG fields. Sleep spindles were generated through the interactions of local and distant network connections and intrinsic currents within thalamocortical circuits. 32,652 cortical neurons were mapped onto the cortical surface reconstructed from subjects' MRI, interconnected based on geodesic distances, and scaled-up to current dipole densities based on laminar recordings in humans. MRIs were used to generate a quasi-static electromagnetic model enabling simulated cortical activity to be projected to the M/EEG sensors. The simulated M/EEG spindles were similar in amplitude and topography to empirical examples in the same subjects. Simulated spindles with more core-dominant activity were more MEG weighted. The model was then refined, to include realistic hierarchical corticocortical connectivity with diffusion MRI based distances and conduction delays. This refined model produces both slow waves and sleep spindles and biophysical conduction models were used to generate synthetic EEG, MEG, and ECoG. Previously published models lacked either spindle-generating thalamic neural dynamics or whole head biophysical modeling; the framework presented here is the first to simultaneously capture these disparate scales. This multiscale model provides a platform for the principled quantitative integration of existing information relevant to the generation of sleep spindles, and allows the implications of future findings to be explored. It provides a proof of principle for a methodological framework allowing large-scale integrative brain oscillations to be understood in terms of their underlying channels and synapses.

Introduction

Magnetoencephalography (MEG) and electroencephalography (EEG, together M/EEG), are complementary, non-invasive, instantaneous, and clinically essential, measures of human neural activity. M/EEG are measured as global brain activities, but are known to ultimately arise from channel currents, at a spatial scale ~8 orders of magnitude smaller (Cohen, 2017). The causal chain which leads to M/EEG can be divided into two linked domains: (1) the biophysical propagation of electromagnetic fields after summating and cancelling under anatomical constraints; and (2) the neurobiology of large networks of active neurons whose ionic currents generate these fields. Here we present an initial effort to traverse the spatial scales by integrating simulations of large networks of neurons with biophysical models of electromagnetic propagation, informed by non-invasive imaging and invasive recordings in humans, as well as decades of work in animal models.

Ion movements through ligand- and voltage-gated transmembrane channels result in current flows which are influenced by the intrinsic channel properties of each neuron and the activity of the network. These currents flow through intracellular and extracellular spaces to form complete circuits, restricted by cellular membranes, and thus microscopic cellular anatomy (Einevoll et al., 2013). Currents cancel and summate locally with those of other neurons in the same cortical column, producing a net current which can be expressed as a multipole expansion (Nunez and Srinivasan, 2009). At a distance, the dipolar term predominates, and the local contribution is typically expressed as a current dipole moment. Before reaching the sensors, current dipole moments from different columns cancel and summate mesoscopically with other columns depending on their relative position and orientation in the highly folded cortical surface, and the covariance and phase synchrony of their magnitudes over time (Ahlfors et al., 2010a, 2010b; Irimia et al., 2012; Linden et al., 2011). Ultimately, the signal at each M/EEG sensor is the result of the complex cancellation and summation of microscopic synaptic and intrinsic

currents from the many thousands or millions of neurons contributing to any single sensor's leadfield.

Transmembrane currents are the result of spontaneous or evoked neural activity, which can be modeled computationally with various degrees of realism, balancing accuracy at the individual cell level against the quantity of neurons that comprise the simulated network. In the current study, we focus on a model for stage 2 of non-rapid eye movement sleep (N2) which is characterized by spontaneous sleep spindles. Sleep spindles manifest in normal M/EEG as spontaneous bursts of 10-16 Hz activity lasting 0.5-2 s and are thought to be important for memory consolidation (Andrillon et al., 2011; Bonjean et al., 2011; Contreras et al., 1996; Dehghani et al., 2011a; Diekelmann and Born, 2010; Sejnowski and Destexhe, 2000). A large number of studies in animal models have established the key elements in spindle generation: local circuit interactions between thalamocortical and thalamic reticular nucleus neurons, reinforcing intrinsic rhythmicity from successive activation of the hyperpolarization-activated cation current, I_h (Destexhe et al., 1996; McCormick and Pape, 1990) and low-threshold Ca^{2+} current I_T (Huguenard and McCormick, 1992; Huguenard and Prince, 1992). Secondarily, the corticothalamic projections play a role in synchronizing and terminating the spindle (Bonjean et al., 2011; Timofeev et al., 2001).

Although the initial circuitry and cellular properties generating spindles are thus in the thalamus, the transmembrane currents that produce the M/EEG are cortical. The thalamocortical projection connecting these structures is comprised of a focal projection to layer 4 (termed the 'core'), and a distributed projection to upper layers (termed the 'matrix') (Jones, 2002, 2001). We found previously that sleep spindles detected in MEG are more numerous and less synchronous than EEG spindles (Dehghani et al., 2010, 2011a), and suggested that this may reflect a relatively greater sensitivity of EEG to the matrix and MEG to the core projections (Piantoni et al., 2016). Consistent data has been obtained with laminar recordings showing primary involvement of middle versus upper layers in different spindles or parts of

spindles (Hagler et al., 2018).

In this report we combine neural and biophysical models to generate M/EEG sleep spindles. The neural model is based on our previous computational modeling including the thalamic and cortical local and distant circuits involved in spindles, including matrix and core (Bazhenov et al., 2000; Bonjean et al., 2012; Krishnan et al., 2016, 2018b). All relevant thalamic ligand- and voltage-gated currents are included. The cortical elements are mapped to 20,484 locations on the ~1 mm resolution cortical surface reconstructed from structural MRI. We have found in previous simulations that this resolution is necessary in order to accurately model the interactions between simultaneously active ECDs in producing M/EEG signals (Ahlfors et al., 2010b). In order to computationally model this large number of elements in cortex we use discrete-time models of neurons, which capture critical features of individual cell dynamics and synapses with difference equations (Rulkov et al., 2004; Rulkov and Bazhenov, 2008).

Empirical sleep M/EEG were collected to provide a basis for model evaluation and simulated neurons were embedded in donor cortical and cranial substrates produced from structural MRI collected from the same subjects. Thus, in our framework, it is the neural activity of individual persons that is modeled, as cortical geometry, since tissues intervening between brain and sensors, and connections among neurons are derived from the reconstructed cortical geometry of the subject. Microscopic cellular currents are scaled to mesoscopic current dipole moment densities using factors derived from human laminar electrode data. The extracranial electromagnetic fields generated by these mesoscopic sources are derived by quasi-static electromagnetic forward modeling, which accounts for orientation induced summation and cancelation by utilizing high-resolution cortical and cranial geometry. The basic validity of the model is tested by comparing the topography and amplitude of simulated macroscale extracranial M/EEG fields to those empirically recorded in the subject used to create the structural model.

The modeling approach employed here, an extension of our earlier work, allows for the currents of the coupled core and matrix networks to be isolated (Bonjean et al., 2012; Krishnan et al., 2018b) and then projected to the extracranial sensors (Gramfort et al., 2010). We find that simulated spindles have similar amplitudes and topographies to those recorded empirically, suggesting that the basic construction of the model is sound. We then apply the model to test the hypothesis that spindles recorded with MEG vs EEG tend to represent activity in the thalamocortical core vs matrix systems. Results consistent with that hypothesis are found. More generally, we demonstrate a proof-of-concept for relating microscale neuronal parameters to macroscale M/EEG observations.

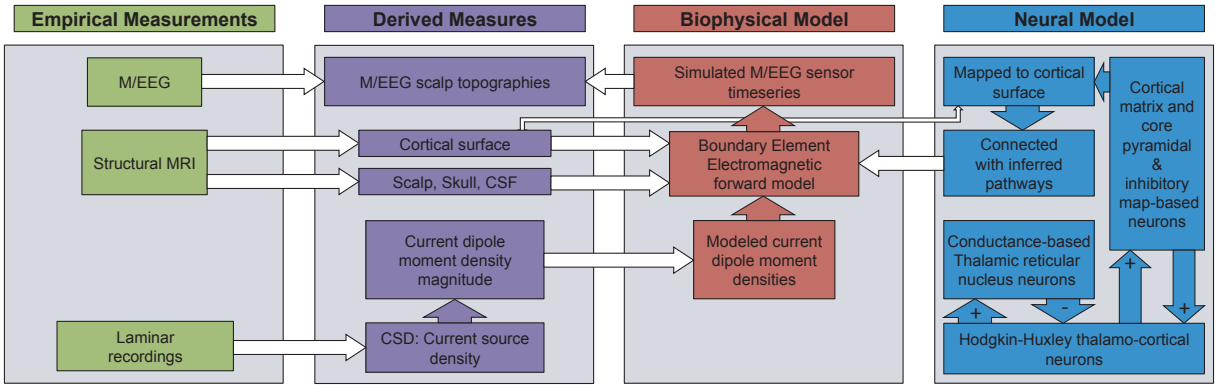

Figure 3.1 Overall structure of experiment. Empirical Measurements are processed to yield Derived Measures which provide validation targets (top), basic anatomical constraints informing the forward solution (middle), or basic physiological constraints for the fundamental unit of spindle generation (bottom). The Neural Model is comprised of thalamic cells modelled at high resolution (to capture the channel and local network synaptic processes underlying spindle generation) driving cortical cells (computationally-efficient map-based neurons), which are embedded in the cortical surface. The Biophysical Model takes the output of the Neural Model and projects it to the M/EEG sensors to be compared to actual empirical measurements

Materials and Methods

The overall structure of the study is shown in Figure 3.1. Two kinds of models were constructed: a Neural Model to compute sleep spindle activity during N2 sleep, based on the known anatomy and physiology of the thalamus and cortex; and a Biophysical Model to project the activity to the M/EEG sensors. Empirical Measurements were obtained and analyzed to produce Derived

Measures, used to specify the models and validate the model: Structural MRI to define the location and orientation of cortical generating dipoles, Laminar recordings to scale the current dipole moment densities generating spindles, and M/EEG in the same subjects to permit validation of model predictions of amplitude and topography.

Empirical Data

Participants: MEG, EEG, and Structural MRI data were recorded for 6 healthy adults, (2 male, ages 20-35). Data for one additional subject was collected but was excluded from analysis due to poor EEG quality. Written informed consent approved by the institutional review boards of the University of California, San Diego or the Partners Healthcare Network, as appropriate, was obtained for all subjects. A whole-head MEG system with integrated EEG cap (Elekta Neuromag) was used to collect 204 planar gradiometers and 60 EEG channels. The position of the subjects' head within the MEG helmet was monitored using head position indicator (HPI) coils (Uutela et al., 2001), updated every 15-20 minutes. Each subject's headshape, HPI coil locations, and EEG electrode positions were digitized (Polhemus isotrak). Structural MR images were acquired in a separate session. While the empirical subjects did not have intracranial electrodes, a virtual ECoG array was placed homologously to those probed in patients with pharmaco-resistant epilepsy.

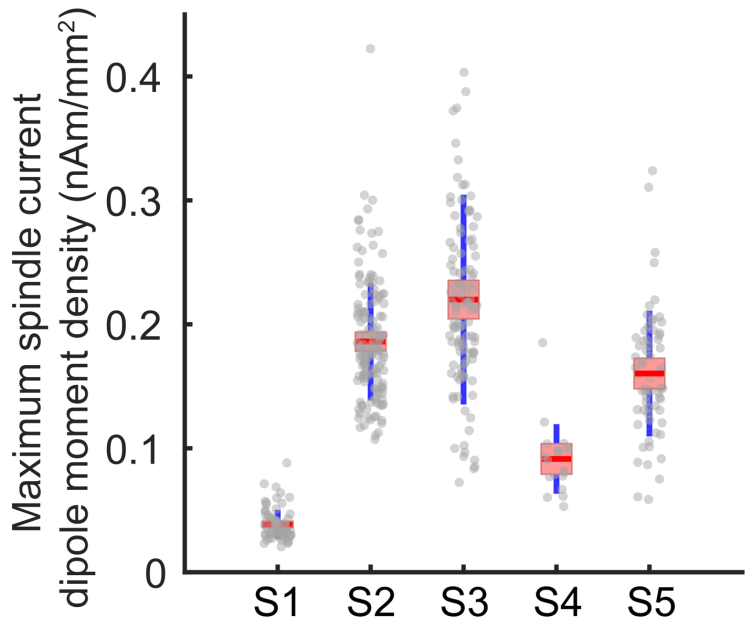

Figure 3.2 Dipole magnitude of sleep spindles in humans. The current dipole moment density was estimated from CSD profiles as described in the text from laminar micro-electrode array recordings (24 contacts at 150μm centers, natural sleep). Gray dots represent the maximum current dipole moment density for each automatically detected 10-16 Hz spindle. Standard deviations and 95% confidence intervals are shown in blue and red, respectively.

M/EEG: M/EEG data were acquired during natural sleep at 1 kHz with a 300 Hz low-pass antialiasing filter. Epochs of stage II non-REM sleep were selected for analysis using standard criteria (Iber et al., 2007). Channels with poor data quality or gross artifacts were excluded by visual inspection. The electrocardiogram artifact was removed with independent component analysis (Delorme and Makeig, 2004).

Structural MRI: High-resolution structural images were acquired with a 1.5 Signa HDx whole body scanner (General Electric). The acquisition protocol consisted of a 3-plane localizer, calibration scan, and a high-resolution T1-weighted MP-RAGE scans (TR = 10.728 s, TE = 4.872 ms, TI = 1000 ms, flip angle = 8 degrees, FOV = 256, 176 sagittal slices, 1 mm isotropic).

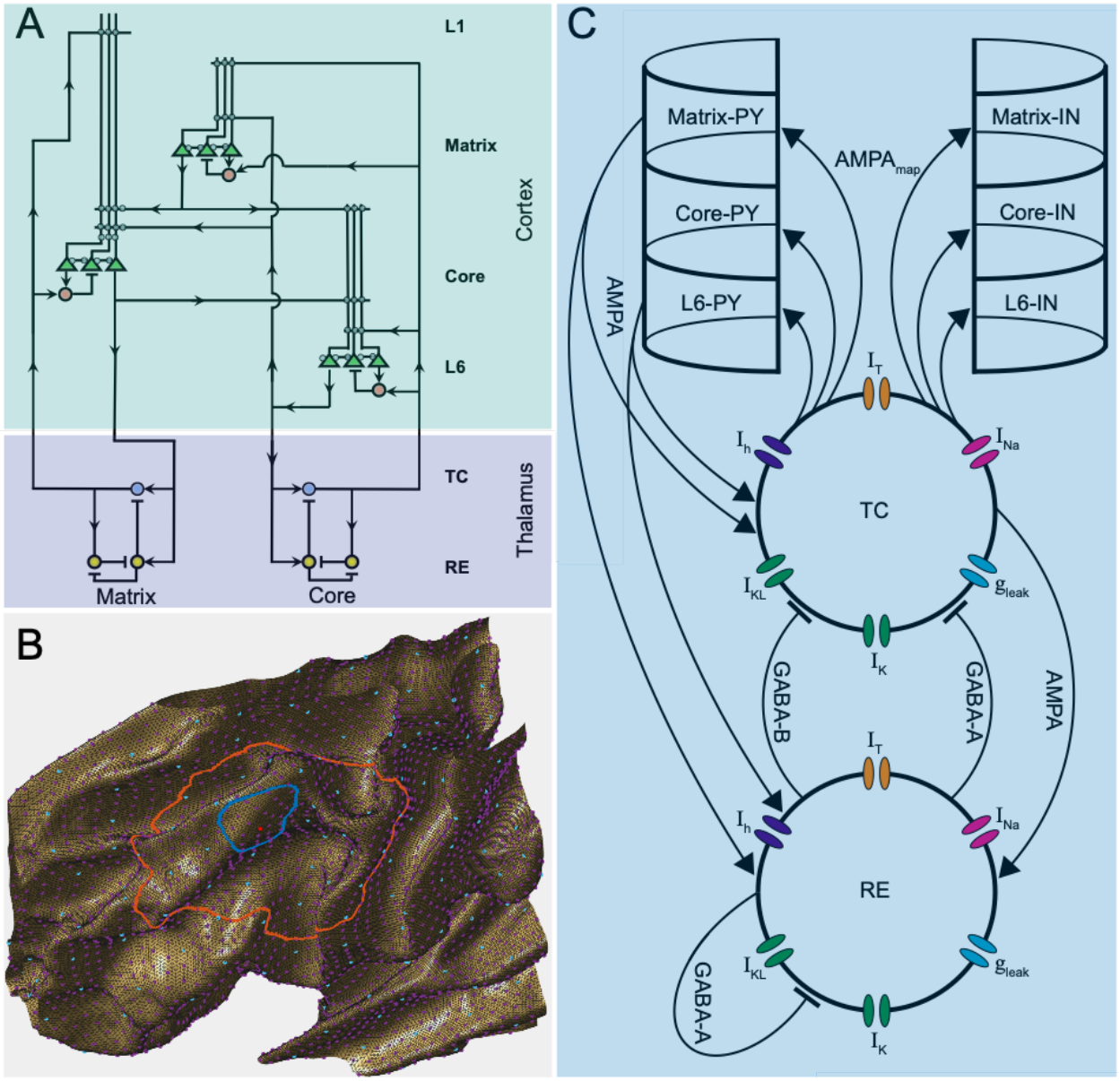

Figure 3.3 Network connectivity. (A) Schematic representation of thalamocortical and corticocortical connections. (B) Example of cortical geodesic-based connectivity in a patch of cortex. Pyramidal and inhibitory cortical neurons exist at purple and cyan locations, respectively. The blue contour shows the fanout (11.7 mm) of a core-projecting thalamic neuron at the virtual position marked in red. The orange contour shows the fanout (45.0 mm) for a matrix-projecting thalamic neuron at the same virtual location. (C) Schematic representation of currents and synapses included in detailed conductance-based thalamic neurons. Corticocortical connectivity is not shown.

Laminar recordings: As described in greater detail in (Hagler et al., 2018), after obtaining fully informed consent according to the Declaration of Helsinki guidelines as monitored by the local Institutional Review Boards, laminar microelectrodes arrays (Ulbert et al., 2001) were implanted into cortical tissue designated for resection in 5 patients (2 male; 15–42

years old) undergoing surgical treatment for drug resistant epilepsy. These arrays consisted of twenty-four 0.040 mm diameter 90%Pt/10%Ir contacts with 0.150 mm on-center spacing and were inserted along the surface normal of the cortex. Microelectrode localization within the cortical lamina was based on surgical procedure and electrode design and confirmed by histology in two patients. Bipolar referencing of reported laminar potentials yields a depth-resolved measure of potential gradients within and among cortical layers to be recorded simultaneously. After wideband (DC 10 kHz) preamplification (gain 10x, CMRR 90db, input impedance 1012 ohms), the laminar gradient recordings were antialiased at 0.5 kHz, gain 1000x, digitized at 2 kHz, 16 bit and stored continuously. Notch filters were applied to remove line noise and data from artifact-containing contacts were replaced by the weighted average of neighboring channels using an exponential decay function, $\lambda = 0.1$ channel spaces, (Hagler et al., 2018). Mild 1d spatial smoothing was applied with a Gaussian kernel ($\sigma = 0.64$ channel spaces), in order to ensure gradual and continuous variation across laminar channels, thereby suppressing false sources and sinks due to minor signal fluctuations.

Derived Measures

Calculation of current dipole moment density scale: Periods of N2 sleep were isolated by the prevalence of generalized slow rhythms and spindles in simultaneously recoded cortical and scalp electrodes. Within these periods spindles were detected as described in Hagler et al. (2018). Briefly, after artifact rejection, spindles were identified as epochs with continuous sustained power in the 10-16 Hz spindle band (Andrillon et al., 2011). Spindle identification was made more selective by adding power in adjacent frequency bands as a rejection criteria (Mak-Mccully et al., 2017). Putative spindle epochs were detected independently for each laminar contact and epochs with durations less than 200 ms were rejected. Epochs containing a spindle in a least one laminar channel were identified and bounded by the earliest spindle onset and latest spindle offset across all channels, yielding a single unified set of detected spindle

epochs for the entire array.

The laminar current source density (CSD), in $\mu A/mm^3$, of sleep spindles was calculated by estimating the explicit quasi-electrostatic inverse of the laminar potential gradients (Pettersen et al., 2006). CSD's were scaled by their distance from the center of the array to yield current dipole moments per unit volume, and then trapezoidally integrated over the length of the column to yield current dipole moment densities, in $\mu Amm/mm^2$, or nAm/mm^2. Microscopic transmembrane currents were scaled up to mesoscopic patch current dipole moment densities, a quantity corresponding to the dipole moment per unit area. This was accomplished by in two steps: scaling these currents by the cortical patch area represented by each column, then scaling these current densities to be consistent with empirical spindle current dipole moment densities recorded from human laminar microelectrode data

M/EEG spindle topographies: Empirical and simulated M/EEG time series were band-passed to between 10 and 16 Hz with an 8^{th} order zero-phase IIR filter. The spindle-band complex analytic signal was extracted with the Hilbert transform and its envelope obtained by computing the elementwise modulus of the phasor time series. Spindles were automatically detected on empirical and simulated EEG standard criterion of sustained power in the 10-16 Hz spindle band (Andrillon et al., 2011). In short, the spindle band envelope was smoothed with a 300 ms Gaussian kernel (σ = 40 ms), and then normalized into units of standard deviation. Spindle occurrences were assigned to peaks of at least 2 s.d. and their temporal extent extended from these peaks until the smooth envelope fell below 1 s.d. For each detected spindle, the mean (unnormalized) envelope was computed and these data were interpolated over flattened sensor positions to produce topographic maps of spindle band envelope in a standardized head space (Oostenveld et al., 2011). Grand average maps were generated by averaging the mean spindle topographies from all subjects, or simulation runs.

ECoG traveling wave detection: Simulated ECoG time series were band-passed to between 10 and 16 Hz with an 8^{th} order zero-phase IIR filter. The spindle-band complex analytic signal was

extracted with the Hilbert transform and the instantaneous phase extracted by taking the arctan of vectors on the complex plane. The spatial gradient of phase vectors was calculated across the ECoG grid and the vector field curl and divergence obtained. In each spindle oscillation cycle the channel with the largest curl value was used as the source of the putative rotating wave and the channel with the largest divergence was used as the source of the putative expanding wave. Traveling wave classification was performed on each cycle by computing the circular-linear correlation coefficient between signal phase, φ, and radial distance from the source for expanding waves:

$$\text{Eq. 1 } \rho_{\varphi,\delta} = \sqrt{\frac{r_{c,\delta}^2 + r_{s,\delta}^2 - 2r_{c,\delta}r_{s,\delta}r_{cs}}{1 - r_{c,s}^2}}$$

where r is Pearson correlation, and c,s are the cosine and sine of φ, respectively (Jammalamadaka and Sengupta, 2001). The circular-circular correlation coefficient between φ and rotation angle, θ, was calculated to detect rotating waves:

$$\text{Eq. 2 } \rho_{\varphi,\theta} = \frac{\sum_{x,y} \sin(\varphi_{x,y} - \bar{\varphi}) \sin(\theta_{x,y} - \bar{\theta})}{\sqrt{\sum_{x,y} \sin^2(\varphi_{x,y} - \bar{\varphi}) \sin^2(\theta_{x,y} - \bar{\theta})}}$$

Where $\bar{\theta} = Arg\left[\sum_{x,y} e^{i\phi_{x,y}}\right]$ and x,y are ECoG grid indices (Fisher, 1993; Muller er al., 2016). Classification was performed by estimating circular-linear and circular-circular correlation coefficients for each oscillatory cycle, creating a null distribution of coefficients by randomly shuffling the channel positions and recalculating 30 times. Spindles were labeled as expanding or rotating if their observed mean correlation coefficients was greater than 99th percentile of shuffled correlation coefficients for all cycles. If a spindle was labeled as both expanding and rotating, it was classified as rotating.

Core/Matrix index: The degree of core or matrix character was quantified for each simulated spindle. First, the 10-16 Hz envelopes were computed for the neural model derived current dipole moment density time series for core and matrix layers, using the procedure

described for M/EEG analysis above. An index of core vs. matrix character was defined:

$$\text{Eq. 3 } Core/Matrix\ index\ = \frac{\sum_{t=1}^{T}\sum_{n=1}^{N}\left|\overrightarrow{s_{(t,n)}^{core}}\right|}{\sum_{t=1}^{T}\sum_{n=1}^{N}\left|\overrightarrow{s_{(t,n)}^{matrix}}\right|} - 1$$

where *T* is the duration of the spindle in samples, *N* is the total number of cortical current dipole moment densities (20484), and $\vec{s}$ is the 10-16 Hz complex analytic signal. Positive values indicate a stronger core character and negative values indicate a stronger matrix character.

Biophysical Model

Cortical reconstruction: White-gray matter surfaces were reconstructed from the MR volumes using FreeSurfer (Fischl, 2012b). Surfaces were sampled at three resolutions as recursively subdivided icosahedra with 642, 10,242, and 163,842 vertices per hemisphere, wherein lower resolution meshes are nested subsets of higher resolution meshes. These are referred to as ico3, ico5, and ico7 surfaces, respectively, indicating the number of subdivisions. Within each hemisphere the geodesic distance between all pairs of vertices was computed using the Dijkstra approximation (Balasubramanian et al., 2009) with 13 Steiner nodes.

Forward Model: The forward model, or gain matrix describing the gradiometer and EEG sensor activity produced by equivalent current dipoles at each ico5 vertex was then computed for each subject's cortex. In addition to the white-gray matter surface, four extra-cortical boundary shells were reconstructed from the segmented (Fischl, 2012b) images: gray-matter-cerebral-spinal fluid (CSF), CSF-inner skull, inner skull-outer skull, and outer skull-scalp. While the cranial boundaries consisted of triangular meshes with 5,124 vertices, critically, the cortical mesh was sampled at ~1 mm resolution (327,684 vertices) in order to capture the summation and cancelation of opposed dipoles. The position of these surfaces relative to the EEG sensors and HPI coils (Uutela et al., 2001) was determined by registering the digitized headshape to the outer-scalp surface using non-linear optimization (matlab's fmincon) with manual corrections. The position of these surfaces relative to the gradiometers was computed using the known

relative positions between and the surfaces and the HPI coils, and the HPI coils and the gradiometers. The orientation of each dipole was set to the surface normal of the white-gray interface. The quasi-static electromagnetic forward solution was numerically computed using a four shell boundary element model, or BEM as implemented with the OpenMEEG software suite (Gramfort et al., 2010; Kybic et al., 2005). Consistent with reported experimental ranges, conductivities of 0.33, 1.79, 0.022, and 0.33 S/m, were used for the brain, CSF, skull, and scalp, respectively.

Rows of the resulting gain matrices were multiplied by the approximate Voronoi area (Meyer et al., 2003) of the cortical patch each represents to yield a vertex by sensor forward operator describing the contribution of each cortical patch's current dipole moment density to each gradiometer and voltmeter. Current dipole moment densities resulting from core and matrix system pyramidal neurons were computed independently, summed together, and then multiplied by the forward operator to yield simulated EEG and MEG gradiometer time series.

Briefly, for the relatively low frequency of biologically relevant signals, electric and magnetic fields become uncoupled and the quasi-static approximations of the Maxwell equations can be used (Nunez and Srinivasan, 2009). Under this regime, the EEG forward model is a numeric solution for voltage, *V,* given *f*, the divergence of current density distribution, $\mathbf{J}^{\mathrm{p}}$, in the Poisson equation:

Eq. 4 $\boldsymbol{\nabla} \cdot (\sigma \boldsymbol{\nabla} V) = f = \boldsymbol{\nabla} \cdot \mathbf{J}^{\mathrm{p}}$

where σ is the tissue conductivity, in S/m. Because the cranial tissues are modeled as nested, closed, and piecewise homogenous domains, the integration reduces down to solving a symmetric linear system (Kybic et al., 2005). For MEG, solving for the magnetic field **B** requires both the current source distribution $\mathbf{J}^{\mathrm{p}}$ and the computed electric field *V*, and is obtained by evaluating the Biot-Savart law at the boundaries:

Eq. 5 $\mathbf{B}(r) = \frac{\mu_0}{4\pi} \int \left(\mathbf{J}^{\mathrm{p}}(\mathbf{r}') - \sigma \boldsymbol{\nabla} V(\mathbf{r}')\right) \times \frac{\mathbf{r}-\mathbf{r}'}{\|\mathbf{r}-\mathbf{r}'\|^3} d\mathbf{r}'$

where **r** and **r′** are displacements of the current source and magnetometer, respectively, and μ_0 is the vacuum permeability constant. Planar gradiometer leadfields are derived by differentiating virtual magnetometer, or integration point, leadfields with respect to the length of the gradiometer. See (Gramfort et al., 2010; Kybic et al., 2005) for these methods in greater detail.

For the refined model, intracranial electrocorticography (ECoG) was created using the equation, for dipolar volume conduction in an infinite homogeneous medium (Nunez and Srinivasan, 2009):

$$\text{Eq. 6 } \Theta(r,\theta) = \frac{Id\cos\theta}{4\pi\sigma r^2}$$

Where *I* is the is the simulated dipole moment density, *d* the effective distance between charges assumed to be 1 mm, σ the brain conductivity assumed to be 0.33 S/m, *r* the radius from the dipole and the sensor, and θ the angle formed between the dipolar axis and the radius. Intracranial potentials were synthesized with a noiseless virtual reference, before, in the case of SEEG, being re-referenced into bipolar recordings.

Neural Model

Neurons: We used a computational model of a thalamocortical network (Fig 2A) with three layers in cortex, with each layer comprised of excitatory (PY) neurons and inhibitory (IN) neurons. The thalamus consisted of a network of core (specific) and matrix (non-specific) nuclei, each consisting of thalamic relay (TC) and reticular (RE) neurons. Conductance-based neural models were used to simulate thalamic neurons. A phenomenological model based on difference equation (map-based model) was used for cortical PY and IN cells. We have previously demonstrated that such map-based neurons are computationally efficient and able to reproduce the response characteristics of conductance-based neurons (Bazhenov et al., 2008; Rulkov et al., 2004; Rulkov and Bazhenov, 2008). Map-based models use a large discrete time step compared to the small integration time step used by pure conductance-based

models while still capturing the dynamics of these models. Map-based models are capable of simulating large-scale network dynamics with emergent oscillatory activity (Rulkov et al., 2004) including slow oscillations during NREM sleep (Komarov et al., 2017).

The following equation describes the update of the PY neurons in time:

Eq. 7 $x_{t+1} = f_\alpha\left(x_t, y_t + \beta I_{syn}\right)$

$$y_{t+1} = y_t - \mu(x_t + 1) + \mu\,\sigma + \mu * \beta_y I_{syn}$$

where variable x_t represents the membrane potential of a biological neuron at time t and y_t represent slow varying ion channel dynamics. The parameter μ (=0.0005) describes the change in the slow variable (μ less than 1 lead to slow update of y variable). The parameter β scale the input synaptic currents (I_{syn}) for x variable, with β =0.133. The parameter σ (=0.02) defines the resting potential of the model neuron. The function f_α is given below:

Eq. 8 $$f_\alpha(x_t, u_t) = \begin{cases} \frac{\alpha}{1-x_t} + u_t, & x \le 0 \\ \alpha + u_t, & 0 < x_t < \alpha + u_t \;\; x_{t-1} \le 0 \\ -1, & x_t \ge \alpha + u_t \; OR \; x_{t-1} > 0 \end{cases}$$

where u_t is taken as $y_t + \beta\, I_{syn}$ from Eq 1, α (=3.65) is a control parameter which was set to obtain tonic spiking like activity for wide range of input currents.

The inhibitory INs were implemented using only the x variable to capture the fast spiking nature of inhibitory neurons and is described by the following equation:

Eq. 9 $x_{t+1} = f_\alpha\left(x_t, y^* + \beta\, I_{syn}\right)$

where, y^*=-2.90 with the same f_α function as Eq 2 with α =3.8 and β =0.05.

The thalamic TC and RE cells were modeled as conductance-based neurons, described by the following equation:

Eq. 10 $$C_m \frac{dV}{dt} = -g_{leak}(V - E_{leak}) - I_{int} - I_{syn}$$

where the membrane capacitance, C_m, is equal to 1 μF/cm^2, non-specific (mixed Na^+ and Cl^-) leakage conductance, g_{leak}, is equal to 0.0142 mS/cm^2 for TC cells and 0.05 mS/cm^2 for RE cells, and the reversal potential, E_{leak}, is equal to -70 mV for TC cells and -77 mV for RE cells. I_{int} is the sum of active intrinsic currents, and I_{syn} is the sum of synaptic currents. The area of a RE cell and a TC cell was 1.43x10^{-4} cm^2 and 2.9x10^{-4} cm^2, respectively. RE and TC cells included fast sodium current, I_{Na}, a fast potassium current, I_K, a low-threshold Ca^{2+} current I_T, and a potassium leak current, $I_{KL} = g_{KL}\ (V - E_{KL})$, where E_{KL} = -95 mV. In addition, a hyperpolarization-activated cation current, I_h, was also included in TC cells. For TC cells, the maximal conductances are g_K = 10 mS/cm^2, g_{Na}= 90 mS/cm^2, g_T= 2.2 mS/cm^2, g_h = 0.017 mS/cm^2, g_{KL} = 0.0142 mS/cm^2. For RE cells, the maximal conductances are g_K = 10 mS/cm^2, g_{Na} = 100 mS/cm^2, g_T = 2.3 mS/cm^2, g_{leak} = 0.005 mS/cm^2. Figure. 3.3C shows a schematic illustration of the currents and synapses in our conductance-based neurons. The expressions of voltage- and Ca^{2+}- dependent transition rates for all currents are given in (Bazhenov et al., 2002; Chen et al., 2012).

Synaptic currents: All the inputs to the map-based neurons were described by the

$$\text{Eq. 11 } \{g_{t+1}^{syn}, d_{t+1}\} = \begin{cases} \{\gamma g_t^{syn} + g_{syn} d_n, (1-\eta) d_n\}, spike_{pre} \\ \{\gamma g_t^{syn}, 1-(1-\delta)(1-d_n)\},, \quad otherwise \end{cases}$$

where g_{t+1}^{syn} and d_{t+1} are the synaptic conductance and depression variable for time t+1, $g_{syn}$is the synaptic coupling strength similar to the maximal conductance. The parameter $\gamma = 0.99$ is the decay variable to capture the first order kinetics of the synaptic transmission, $\eta = 0.00005$ is the rate of decay of the depression variable (d). The synaptic currents that are input to all conductance-based neurons were governed by equations given in (Timofeev et al., 2000) and reproduced here:

$$\text{Eq. 12 } \mathrm{I_{syn}} = g_{syn}[O](V - E_{syn})$$

where $g_{syn}$is the maximal conductance, $[O]$ is the fraction of open channels, and E_{syn} is the reversal potential. In RE and PY cells, reversal potential was 0 mV for AMPA receptors, and -70

mV for GABA-A receptors. For TC cells, the reversal potential was -80 mV for GABA-A receptors, and -95 mV for GABA-B receptors. GABAA, and AMPA synaptic currents were modeled by the first-order activation schemes. GABA-B receptors were modeled by a higher-order reaction scheme that considers the activation of K^+ channels by G-proteins. The fraction of open channels $[O]$ is calculated according to the kinetic equation:

Eq. 13 $\frac{\mathrm{d}[O]}{\mathrm{d}t} = \alpha(1-[O])[\mathrm{T}] - \beta[O], [T] = A\Theta(t_o + t_{max} - t)\Theta(t - t_o)$

where Θ(x) is the Heaviside function, t_0 is the time instant of receptor activation. The parameters for the neurotransmitter pulse were amplitude A = 0.5 and duration t_{max} = 0.3 ms. The rate constants, a and β, were a = 10 ms and β = 0.25 ms for GABA-A synapses and a = 0.94 ms and β = 0.18 ms for AMPA synapses. E was calculated according to the interactive scheme (Tsodyks and Markram, 1997).

Eq. 14 $E_{n+1} = 1 - [1 - E_n(1 - U_{SE})]e^{-\Delta t/\tau}$

where Δt is the time interval between nth and (n+1)th spike, τ = 700 ms is the time constant of recovery of the synaptic resources and U_{SE} is the fractional decrease of synaptic resources after an action potential which was varied between 0.07 and 0.15. Spontaneous miniature EPSPs and IPSPs were included for the AMPA and GABA-A connections within cortical neurons. The arrival times of miniature EPSPs and IPSPs followed the Poisson process (Stevens, 1993), with time-dependent mean rate

Eq. 15 $\mu = \log(\frac{t - t_0 + T}{T})$

where t is current time and t_0 was timing of the last presynaptic spike and T = 50 ms.

Synaptic conductance: The maximal conductances for various connections were $g_{GABA\text{-}A}$(RE-TC) = 0.045 μS, $g_{GABA\text{-}B}$(RE-TC) = 0.06 μS, $g_{GABA\text{-}A}$(RE-RE) = 0.175 μS; core thalamus: g_{AMPA}(TC-PY) = 0.03 μS, g_{AMPA}(TC-IN) = 0.015 μS; matrix thalamus: g_{AMPA}(TC-PY) = 0.045 μS, g_{AMPA}(TC-IN) = 0.02 μS; connections within each layer (matrix, core and L6) pyramidal neurnons: g_{AMPA}(PY-PY) =

2.5 nS, g_{NMDA}(PY-PY) = 0.4 nS; connection from matrix to core: g_{AMPA}(PY-PY) = 1.5 nS, g_{NMDA}(PY-PY) = 0.1 nS; connection from matrix to L6 : g_{AMPA}(PY-PY) = 2.0 nS, gNMDA(PY-PY) = 0.2 nS; connection from core to matrix: g_{AMPA} (PY-PY) = 1.5 nS, g_{NMDA}(PY-PY) = 0.1 nS; connection from core to L6: g_{AMPA}(PY-PY) = 2.0 nS, g_{NMDA}(PY-PY) = 0.2 nS; connection from L6 to matrix: g_{AMPA}(PY-PY) = 2.0 nS, g_{NMDA}(PY-PY) = 0.2 nS; connection from L6 to core: g_{AMPA}(PY-PY) = 1.5 nS, gNMDA(PY-PY) = 0.1 nS; connection betwen PY and IN cells for all layers: g_{AMPA}(PY-IN) = 0.05 μS, g_{NMDA}(PY-IN) = 0.4 nS, $g_{GABA\text{-}A}$(IN-PY) = 0.05 μS and connection from core and L6 cells to thalamic neurons: g_{AMPA}(PY-TC) = 0.025 μS, g_{AMPA}(PY-RE) = 0.045 μS.

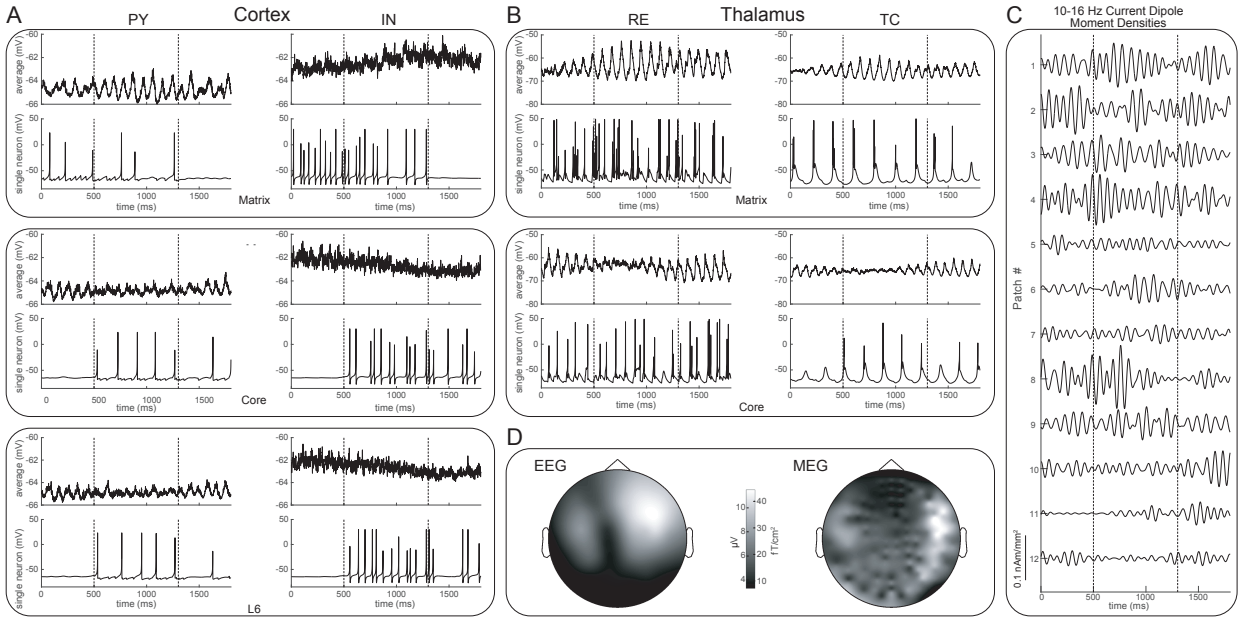

Figure 3.4 Example simulated spindle. Single-neuron and population mean membrane voltage traces in cortex (A) and thalamus (B) during a matrix-weighted spindle. Simultaneous activity is shown for the matrix and core system neurons of the reticular nucleus (RE) and thalamocortical (TC) subpopulations of the thalamus, as well as the pyramidal (PY) and inhibitory (IN) subpopulations in each of the three cortical layers. (B) Transcortical currents and scaled current dipole moment densities. Twelve spatially representative columns selected through icosahedral subsampling are shown. (C) Average 10-16 Hz M/EEG topographies for the duration of the spindle. In panels (A-C) the spindle duration is demarcated with vertical dashed lines. All panels display the same modeled spindle.

Network connectivity: A schematic of network connectivity is shown in Fig 2A. For each subject's donor cortex, one pyramidal neuron was simulated for each vertex in the ico5 mesh (10,242 vertices per hemisphere) for each of layers matrix, core, and L6. The ico3 mesh was populated with inhibitory and thalamic neurons at each of 642 vertices per hemisphere. For all

intra-hemispheric synapses, connectively was established by comparing synapse-specific fan-out radii to the geodesic distance between vertices on the ico7 cortex (163,842 vertices per hemisphere), see Figure 3.3B. Inter-hemispheric synapses were threaded between homologously located cortical neurons in 85% of cases and the remaining connections were made between randomly located neurons. The probability of transmission in interhemispheric synapses was reduced to 25% and 50% in the core and matrix systems, respectively, in order to represent sparse collosal connectivity. Figure 3.5B shows simulated current on an inflated cortex at a single time point for the core and matrix neurons.

In a refined model, The number of cortical layers was expanded to six (L2, L3, L4, L5a, and L5b) and the number of simulated neurons increased accordingly. The cortex was parcellated into 180 areas per hemisphere according to the HCP-PPM1.0 atlas (Glasser et al., 2016). Parcels were assigned a hierarchical index based on a noninvasive estimate of their bulk myelination (Glasser et al., 2011;Burt et al., 2018). Excitatory corticocortical connections were assigned into 6 classes based on the difference in hierarchical index of pre- and post-synaptic neurons: within local column, within same parcel, weakly ($<50^{th}$ percentile) feedforward, strongly ($>50^{th}$ percentile) feedforward, weakly feedback and strongly feedback. Synaptic weights for these connections were scaled based on reports of connectivity in histological studies (Markov et al., 2013; Rockland, 2019). Corticocortical as well as thalamocortical and corticothalamic connection weights are shown in table 3.1.

Furthermore, in the refined model, connectivity was scaled based on diffusion MRI (dMRI) connectivity we have previously reported (Rosen and Halgren, 2021) rather than using fixed connection radii. Inter-parcel dMRI connectivity shows an exponential relationship with length constant $\lambda = 23.4$ mm and scaling parameter 0.17. To impute a higher-resolution inter-column connectivity for the model, we compared parcelwise intra-hemispheric dMRI streamline distances to geodesic distances and found them to be related to a first approximation by a linear rational function $F(x) = (p_1*x + p_2) / (x + q_1)$ with parameters $p_1 = 295.6$, $p_2 = -2256$, and $q_1 =$

69.4. By applying this function to the columnwise geodesic distances, intercolumnar fiber distances were estimated. Connection probability between neurons was then scaled by

Table 3.1 Interlaminar connection weights in the refined model.

Within Column

		postsynaptic					
		L2	L3	L4	L5a	L5b	L6
presynaptic	L2	2	2	0	2	2	0
	L3	2	2	0	2	2	0
	L4	2	3	3	1	1	1
	L5a	1	1	0	2	2	0
	L5b	1	1	0	0	3	2
	L6	0	0	1	0	2	2

Within Parcel

		postsynaptic					
		L2	L3	L4	L5a	L5b	L6
presynaptic	L2	1	0	0	0	0	0
	L3	0	2	0	0	0	0
	L4	0	0	0	0	0	0
	L5a	0	0	1	1	0	0
	L5b	1	0	0	0	0	0
	L6	0	0	0	0	1	1

Weakly feedforward

		postsynaptic					
		L2	L3	L4	L5a	L5b	L6
presynaptic	L2	0	0	0	0	0	0
	L3	0	2.5	1.25	0	0	0
	L4	0	0	0	0	0	0
	L5a	0	0	0	1.25	0	0
	L5b	0	0	0	0	0	0
	L6	0	0	0	0	0	0

Strongly Feedforward

		postsynaptic					
		L2	L3	L4	L5a	L5b	L6
presynaptic	L2	0	0	0	0	0	0
	L3	0	3	2	0	0	0
	L4	0	0	0	0	0	0
	L5a	0	0	0	0	0	0
	L5b	0	0	0	0	0	0
	L6	0	0	0	0	0	0

Weakly feedback

		postsynaptic					
		L2	L3	L4	L5a	L5b	L6
presynaptic	L2	1	0	0	0	0	0
	L3	0	0	0	0	0	0
	L4	0	0	0	0	0	0
	L5a	0	0	0	0	0	0
	L5b	0	0	0	0	0	0
	L6	1	1	0	0	1	1

Strongly Feedback

		postsynaptic					
		L2	L3	L4	L5a	L5b	L6
presynaptic	L2	0	0	0	0	0	0
	L3	0	0	0	0	0	0
	L4	0	0	0	0	0	0
	L5a	0	0	0	0	0	0
	L5b	0	0	0	0	0	0
	L6	1.25	1.25	0	0	1.25	1.25

Corticothalamic

		postsynaptic			
		Core TC	Core RE	Matrix TC	Matrix RE
presynaptic	L5b	0	0	1	1
	L6	1	1	0	0

Thalamocortical

		postsynaptic					
		L2	L3	L4	L5a	L5b	L6
presynaptic	Core TC	0	1	3	0	0	1
	Matrix TC	1	1	0	1	1	1

applying the observed parcelwise dMRI exponential function to the imputed columnwise fiber distance. In addition, residual connectivity inter-parcel dMRI connectivity, estimated by regressing out the exponential trend, was added to inter-column connections based on each column's parcel identity. In effect, this connectivity accounts for the functional specialization of each parcel of cortex. Lastly, realistic conduction delays proportional to the fiber distance between neurons was implemented. Note that while the hierarchal index and dMRI distances are for the group average of the (Rosen and Halgren, 2021) cohort, for the refined model they were mated to the biophysical model of a single subject using high-resolution surface registration (Fischl et al., 1999).

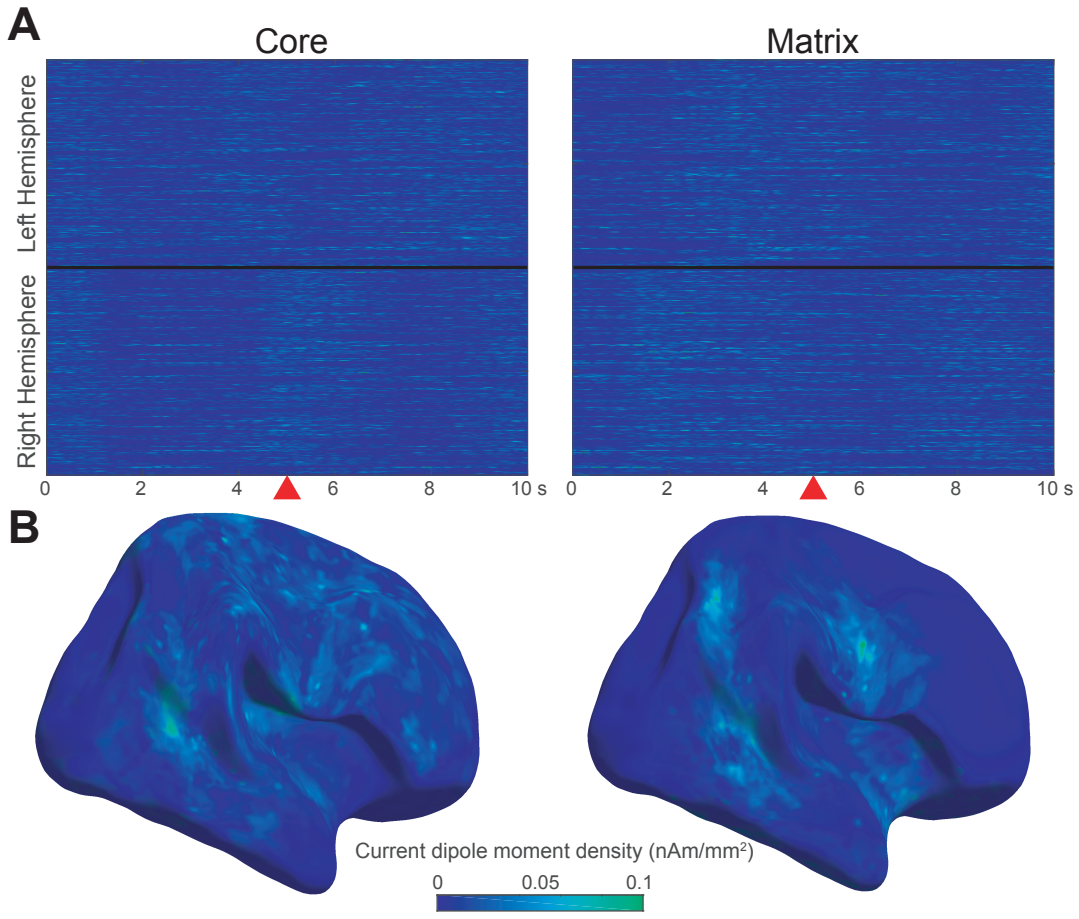

Figure 3.5 Simulated cortical sources. (A) 10 seconds of simulated spindling for one subject. (B) matrix and core pyramidal current dipole moment density distributed across the cortex at a single time point, marked in red. Data are displayed on an inflated right cortex.

Results

We designed a thalamocortical network model that combined the detailed laminar connectivity with the network connectivity of the whole brain based on MRI reconstructions. Using this approach we demonstrate the feasibility of connecting the cellular level activity with the macroscopic activity seen in M/EEG. We used a difference equation (map-based) model for cortical neurons, which has the computational efficiency necessary for simulating the cortex at sufficient resolution to accurately reproduce the cancellation and summation of cortical dipoles; we used conductance-based neuronal models for the thalamic network, which has the elements necessary to accurately reproduce the interaction of voltage-gated channels and recurrent synaptic connections central to spindle generation.

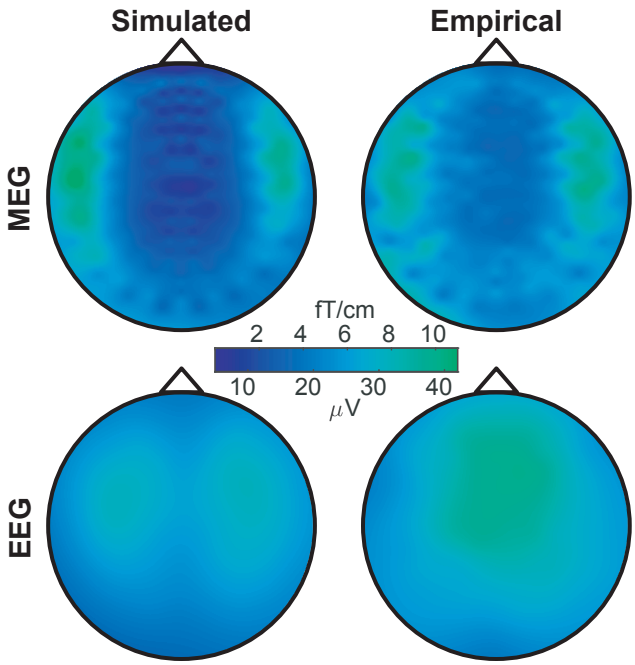

Figure 3.6 Grand average 10-16 Hz complex envelope topographies for empirical and simulated M/EEG during automatically detected EEG spindles. Empirical data show averages for six subjects, simulated data for six simulation runs using those subjects' cortical surfaces, cranial tissue boundaries, and M/EEG sensor positions. The same MEG and EEG scales are used for both empirical and simulated topographies.

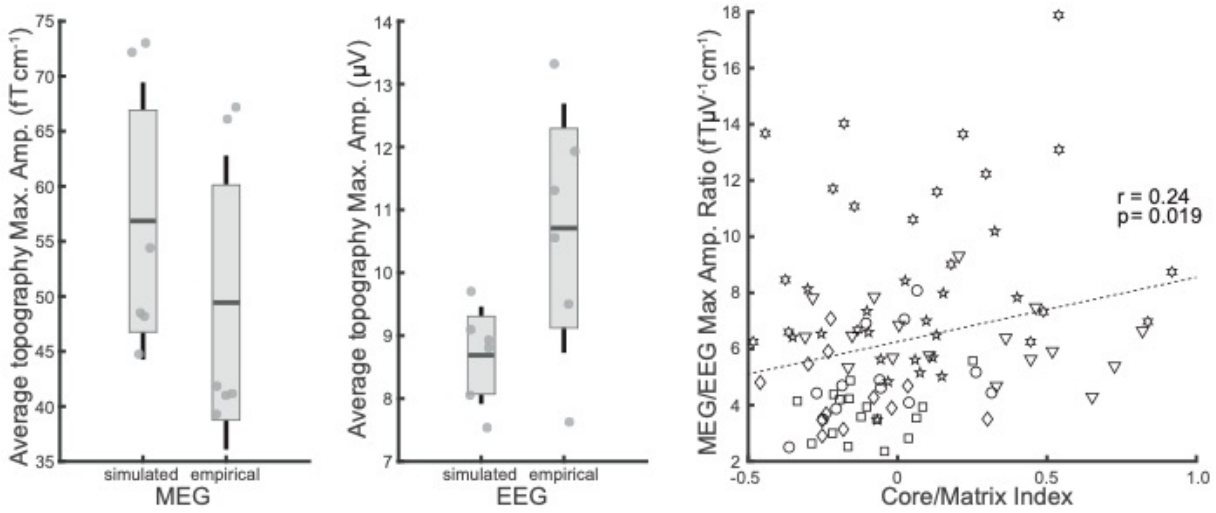

Figure 3.7 M/EEG sensor 10-16 Hz envelope maxima during EEG spindles. (A) For simulated and empirical M/EEG, 10-16 Hz envelopes are averaged across the duration of the spindles then averaged across spindles. The envelope magnitudes of strongest sensors are shown. Each marker represents the average value for one subject. (B) Simulated individual spindle sensor maxima vs. neural model derived core/matrix index. Positive index values indicate a more core-weighted spindle while negative values indicate a more matrix-weighted spindle. Each marker represents an individual simulated spindle with symbols signifying the simulation run, each using a different donor subjects' cortical surfaces, cranial tissue boundaries, and M/EEG sensor positions.

In a manner similar to our previous studies, (Bazhenov et al., 2000; Bonjean et al., 2011; Krishnan et al., 2016), the state of the network was set to be stage 2 sleep state by modifying the intrinsic and synaptic currents to mimic the level of low acetylcholine, nor-epinephrine and histamine. In this state, the network spontaneously generated electrical activity consisting of multiple randomly occurring spindle events involving thalamic and cortical neuronal populations. Spindle oscillations are driven by thalamic cell bursting as observed by experimental recordings (Steriade et al., 1993). Spindles spontaneously reappeared every 3–10s in agreement in prior intracellular data (Contreras et al., 1996) and computational models (Bazhenov et al., 2000; Bonjean et al., 2011; A. Destexhe et al., 1996; Destexhe et al., 1998). In this computational model, the initiation and termination of spindle sequences critically involved corticothalamic influences (Bonjean et al., 2011; Contreras et al., 1996; Timofeev et al., 2001). Furthermore, the synchronization of spindles across cortical and thalamic regions is determined by the strength and fanout of thalamocortical and corticothalamic connections (Bonjean et al.,

2011; Krishnan et al., 2018b). The model consisted of two thalamocortical systems: core and matrix. The matrix system had broad thalamocortical and corticothalamic projections which is known to result in lower spindle density and increased spatial synchrony (Krishnan et al., 2018b). During spindles, cortical and thalamic neurons in both the core and matrix system had elevated and synchronized firing (Fig 3A) consistent with previous in-vivo experimental recordings (Steriade et al., 1993). This computational neural model was fed into a biophysical model: an electro- and magnetostatic forward model was applied to large-scale simulations of a thalamocortical network to simulate EEG and MEG signals.

As described in the Methods, current dipole moment densities were calculated using linear microelectrode array recordings spanning the cortical surface scale during sleep spindles in stage N2 sleep. The laminar current source density (CSD), in $\mu A/mm^3$, of sleep spindles was calculated by estimating the explicit quasi-electrostatic inverse of the laminar potential gradients (Pettersen et al., 2006), followed by appropriate spatial scaling and integration over the cortical column to yield current dipole moment densities. As shown in Figure 3.2, we found sleep spindle surface current densities have an average maximum spindle-band envelope on the order of 0.1 nAm/mm^2 with considerable variation. Therefore, the simulated neural currents (in nA) were divided by the approximate Voronoi area (Meyer et al., 2003) of the cortical patch each represents, then scaled to approximately match in amplitude this surface current dipole moment density, yielding corresponding current dipole moment densities in nAm/mm^2.

We found our model was able to simulate essential elements of empirical M/EEG. Grand average topographies of simulated and experimental data, shown in Figure 3.6, are qualitatively similar to experimental ones. The empirical MEG topography, in particular, is well-reproduced and shows the characteristic pattern (Dehghani et al., 2011b; Manshanden et al., 2002) of frontolateral gradiometer activation. The dynamic range across the scalp is higher in the simulated data, likely because the empirical data contains widespread non-spindle background activity, forming the $1/f$ curve of the power spectrum, and which was not included in the neural

model.

The simulated EEG topography, while matching the frontal position of the empirical data on the anterior-posterior axis, modestly differs in its lateral distribution. Whereas the empirical topography characteristically peaks along the midline, the two dorsal lobes of the simulated data only partially converge there. This may be due the model's relatively crude implementation of inter-hemispheric connectivity, which consisted of low reliability synapses between mostly homologous cortical areas. An alternative possibility is that the ideal dipole model is incomplete for EEG.

The simultaneously simulated MEG and EEG are also similar in magnitude of the empirical M/EEG (Figure 3.7A) with average spindle topography maxima (mean ± s.d. across all subjects or model runs) of 56.8 ± 12.6 fT/cm and 49.4 ± 13.4 fT/cm, $p = 0.93$, for simulated and empirical MEG, respectively, and 8.7 ± 0.8 μV and 10.7 ± 2.0 μV, $p = 0.96$, for simulated and empirical EEG. However, despite their quantitative similarity, the simulated EEG and MEG spindles show opposite systematic tends, with simulated MEG spindles being slightly stronger and EEG spindles being weaker and less varied than empirical examples. This differential bias may be due insufficiently detailed or inaccurate cranial tissue conductivities, factors that have a much greater bearing on EEG than MEG, for whom these tissues are nearly transparent. Individual differences in skull conductivity (Akalin Acar and Makeig, 2013), in particular, may explain the increased inter-subject variability in empirical spindles. Another possibility is that the biophysical generation of these signals, commonly thought of as absolutely unified for a given source distribution, are in fact partially uncoupled, perhaps by the accumulation of static charges or effective monopoles, here unaccounted for, which would contribute to EEG but not MEG.

For simulated spindles, the relative contributions of the core and matrix systems to current dipole moment densities was quantified and, as shown in Figure 3.7B, we found this index to correlate with the ratio of derived MEG vs. EEG maxima (Pearson's $r = 0.24$, $p = 0.019$). These data are consistent with the hypothesis that MEG gradiometer recordings are more sensitive to

core system neurons when compared to EEG recordings which are biased towards the matrix system. However, other factors, including individual differences, could also explain these results, and more focused studies are needed.

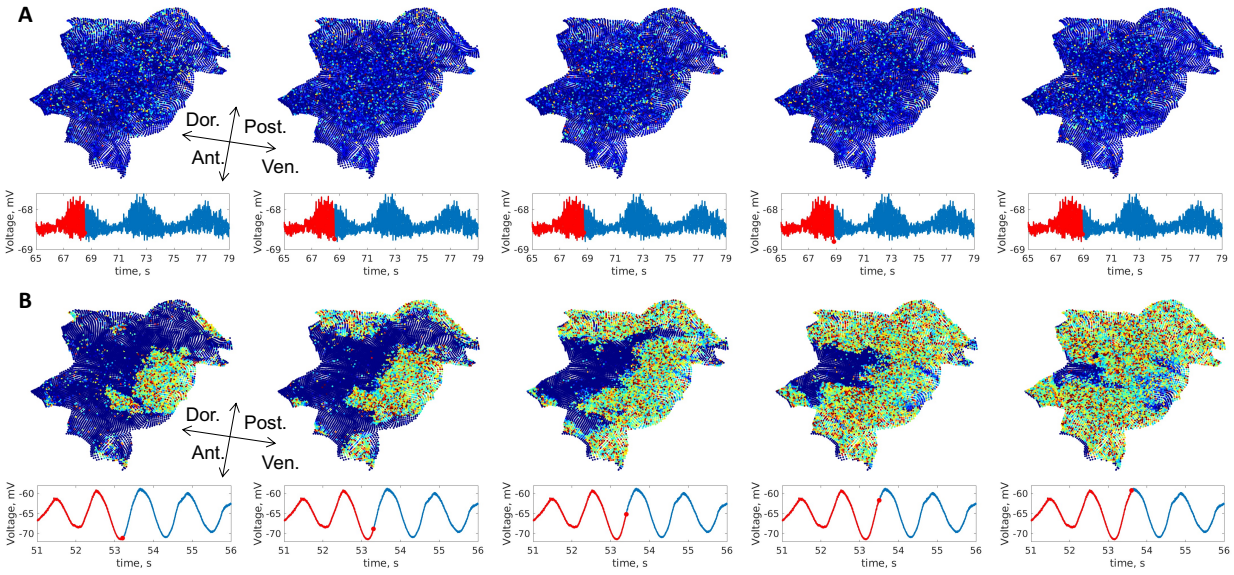

Figure 3.8 Simulated sleep spindles and slow oscillations. Membrane voltages from the refined model are presented on a flattened cortex. (A) sleep spindles. (B) Slow Oscillations.

A refined model with a 6-layer cortex, hierarchically specified interlaminar routing, dMRI-based connection probabilities, and realistic conduction was tuned to produce the slow oscillations and spindles characteristic of non-REM sleep. For spindles, patterns of simulated activity were broadly similar to the earlier model. Cortical spindles initiate in various regions of the cortical surface and locally propagate rather than showing global synchrony, as is often observed on the scalp. Then the cortical currents are projected to the virtual MEG and scalp EEG by use of a biophysical forward model, the topographies are similar to empirically observed examples and importantly have reasonable amplitudes for EEG and MEG simultaneously, see Figure 3.9. Hemisphere-spanning rotating waves during sleep spindles, first reported by (Muller er al., 2016) are observed in synthetic ECoG generated from the refined model (Figure 3.10). These waves are qualitatively similar in dynamics and spatial scope to those reported in (Muller er al., 2016). Expanding wavefronts are also observed, though less often than rotating waves. The

probability of detecting rotating and expanding wave patterns during simulated spindles is not significantly altered when corticocortical connectivity is made random or uniform, or when hierarchical interlaminar routing is removed, or even when all excitatory corticocortical connectivity is removed from the model. This strongly suggests that these patterns are thalamic in origin and are projected to the cortex through thalamocortical circuits.

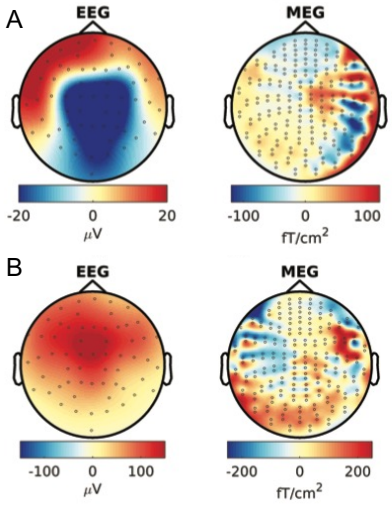

Figure 3.9 Synthetic EEG and MEG from simulated spindle and slow oscillation. Data from refined model. (A) sleep spindle (B) Slow Oscillation

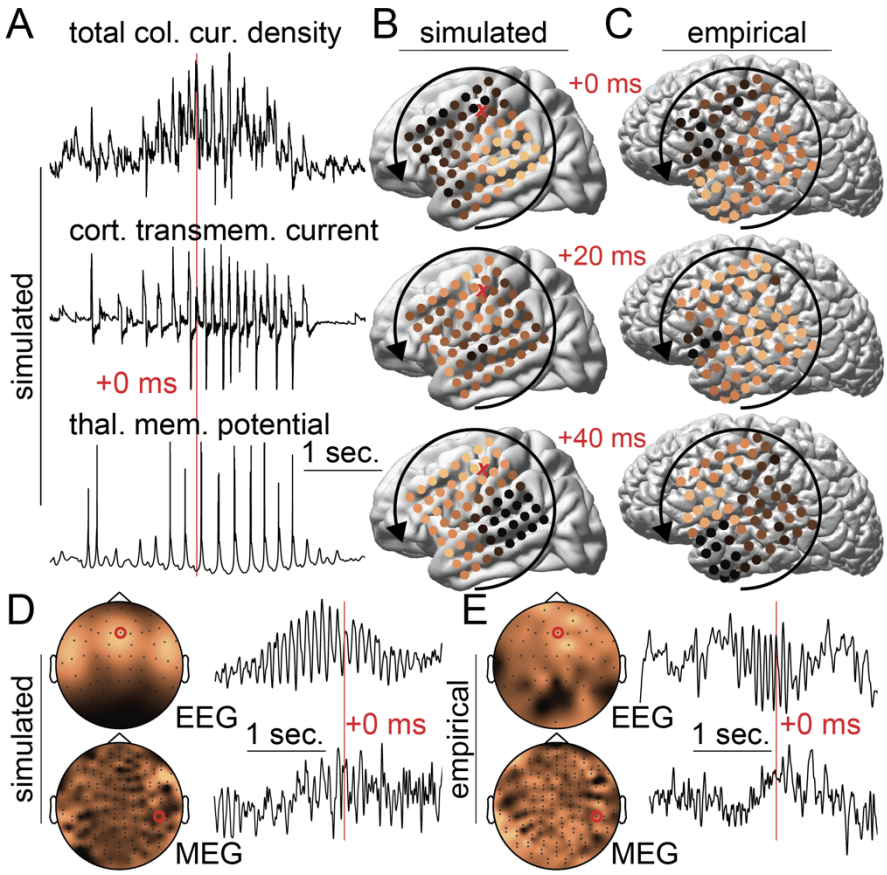

Figure 3.10 Simulated rotating spindle wave. A. Membrane potential for a representative thalamo-cortical cell, total intracellular input current for an L4 cortical pyramidal cell, and the total current density for the columnar area. The column's location is indicated by the red x in panel B. Time marker +0 ms is synchronized across all simulated data panels (A, B, D). B. Virtual ECoG activity for the same simulation showing a rotating wavefront during the spindle. C. An empirically recorded rotating wavefront during a spindle, reproduced with modifications from Figure 1B from Muller L, Piantoni G, Koller D, Cash SS, Halgren E, Sejnowski TJ. 2016. Rotating waves during human sleep spindles organize global patterns of activity that repeat precisely through the night. Elife 5:1–16 (https://creativecommons.org/licenses/by/4.0/). D. Simulated whole head EEG and MEG topographies at time +0 ms and sensor waveforms for the channels indicated with red circles. E. Empirical EEG and MEG spindle topographies for time +0 ms and accompanying waveforms for the channels indicated with red circles.

Discussion.

In this study, we developed a computationally efficient large-scale hybrid thalamocortical model which generated sleep spindles in cortical patches. We estimated the magnitude of current dipole density from empirical measures and then used a biophysical model to project the output of the model simulation to the EEG, MEG and ECoG sensors. The patches were embedded in the reconstructed cortical surface based on structural MRI data,

and sufficiently dense to accurately model the summation and cancellation that occurs as M/EEG signals propagate from their cortical generators to the extracranial sensors. The amplitude and topography of the M/EEG derived from the model were similar to those found in empirical recordings in healthy subjects, when using their individual brain and head anatomy to define the projection from cortex to M/EEG, thereby suggesting that our approach is basically sound. We then applied our model to test the previous hypothesis (Bonjean et al., 2011; Dehghani et al., 2010) that EEG activity during spindles is relatively more sensitive to the matrix thalamocortical system, while MEG is relatively more sensitive to the core thalamocortical system.

Thus, using this approach, we demonstrate the viability of an integrated model for the generation of EEG and MEG, proceeding from ionic and synaptic activity, through local and distant networks, whose currents are then passed through a realistic biophysical model to generate M/EEG fields that correspond to empirical recordings, a foundational problem in neuroimaging. The model presented here simultaneously satisfies a considerable ensemble of neural and biophysical constraints including: dozens of neural properties, low-threshold Ca^{2+} current dynamics, the location and orientation of the cortical ribbon, empirically-backed biophysically probable maximum current dipole moment densities, and observed simultaneous M/EEG topographies and amplitudes. This multitude of constraints, embedded in each of the many scales the model traverses, precludes the pitfall of evoking over-tuned parameters in order to reproduce over-circumscribed behaviors. Given the ambitious scope of our model and the complexity of the system that it attempts to emulate, it is unsurprising that its limitations are numerous, including limited realism of the neural and biophysical models, limited application to M/EEG phenomena, and limited validation measures.

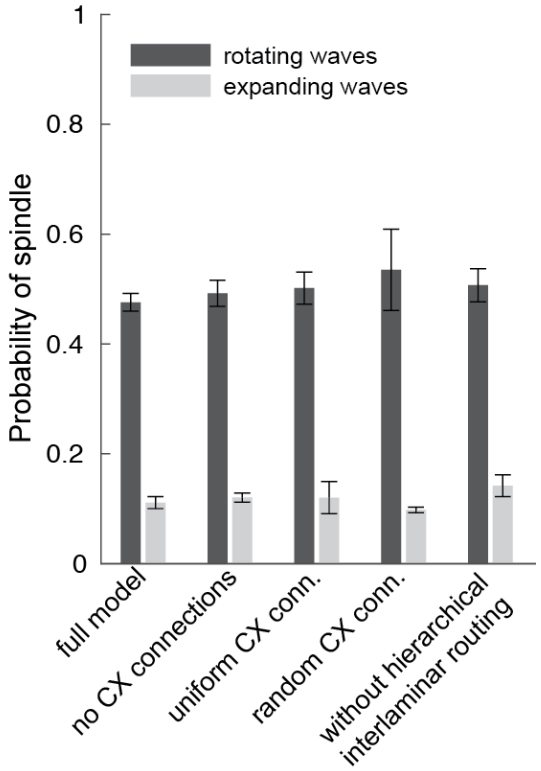

Figure 3.11 Virtual ECoG traveling waves not dependent on corticocortical connectivity. Error bars show standard error of the mean across simulation runs with different random seeds. Removing all excitatory corticocortical (CX) connections, imposing uniform or random CX connectivity, and removing hierarchically-based interlaminar routing weights does not significantly alter the probability of traveling wave patterns.

Our neural model simulated 65,304 cortical neurons and 5,136 thalamic neurons. While the model is thus much larger than previous efforts of this kind, it is still contains about 250,000 times fewer neurons than the actual human forebrain. Moreover, each simulated neuron is considerably simpler than a real neuron, especially in the number of synapses and number of dendritic compartments. In addition, subcortical areas other than the thalamus are not included in our model. While the direct contribution of these areas to extracranial M/EEG is minimal (Cohen et al., 2011), many, e.g. the nucleus basalis and hippocampus, may play critical roles in the timing, extent, amplitude and propagation of cortical activity during spindling. Notwithstanding these limitations, the model is sufficiently complex to generate sleep spindles using the same voltage-gated currents, within the same local thalamic and distant thalamo-

cortico-thalamic synaptic circuits, as have been shown (Bonjean et al., 2012; Krishnan et al., 2018b) to generate sleep spindles in vivo. Furthermore, the model was sufficiently large to generate cortical patterns with a complexity that appears similar to that recorded in vivo (Frauscher et al., 2015; Mak-McCully et al., 2015; Piantoni et al., 2016) although this needs to be further investigated.

At its base, our study used a realistic computational model at the level of intrinsic and synaptic transmembrane currents to simulate MEG and EEG. It would be possible to increase the number of modeled neurons by using a population based neural mass model. Using such a model, Ritter et al. (2013) have modeled EEG signals from cortical activity projected to extracranial sensors. While such models could reproduce the spectrogram of EEG, they do not explicitly resolve activity at the level of individual neuron's ionic or synaptic currents. This becomes critical when trying to leverage information from extensive intracellular and direct recordings of cortical and thalamic activity, to test new hypotheses. For example, abnormal spindling is common in schizophrenia (Wamsley et al., 2012) and variants of the gene CACNA1I, which encodes a T-type low-threshold Ca^{2+} channel and is expressed in the reticular nucleus of the thalamus (Manoach et al., 2016), are implicated in schizophrenia risk (Ripke et al., 2014). The framework we present can be used to simulate the effects of abnormal low-threshold Ca^{2+} channels on M/EEG. Costa and colleagues (Costa et al., 2016) included some of channel details in their neural mass model, but their biophysical modeling of EEG only considered an anatomically and physiologically implausible point source.

An important limitation of the neural model presented here is that it does not fully take into account functional specialization or cytoarchitectonic differentiation among cortical regions, including hemispheric lateralization. The model framework, however, can accommodate these distinctions. Projects using non-invasive structural, functional and diffusion MR imaging in large healthy populations now provide detailed cortical parcellations into distinct areas (Glasser et al., 2016). In the refined model, we used this parcellation to introduce some

functionally specific connectivity at the inter-parcel and inter-laminar level of organization. Parcellation schemes may also be combined with post-mortem transcriptomes to map receptor and channel variants, as well as laminar and cellular properties across the cortical mantle (Burt et al., 2018; Smith et al., 2013; van den Heuvel and Sporns, 2013). Future work could incorporate these cortical specializations into the neural model to determine if they underlie the variations in spindle amplitude and frequency across cortical areas which have been found with intracranial recordings (Frauscher et al., 2015; Mak-McCully et al., 2015; Piantoni et al., 2016).

Non-invasive imaging studies in humans and tracer studies in primates provide estimates of structural and functional connectivity between cortical areas (Glasser et al., 2016; Markov et al., 2014). The connections in our model did not incorporate these estimates but relied on the geodesic distance between cortical locations. While geodesics are a closer analog to anatomical and functional connectivity than conventional Euclidian distances, they remain a limiting simplification. A related limitation in our neural model is its lack of a conduction delay. Such delays are on the order of 10s of ms between lobes or between the thalamus and cortex (Klopp et al., 2000; Mak-Mccully et al., 2017), and thus, together with the strength and pattern of cortico-cortical connections could have a substantial effect on the propagation patterns (Muller et al., 2016), coherence, or phase relationships within and among spindles. These large-scale interactions are important for determining whether and how dipoles summate and propagate to the M/EEG sensors, and need to be addressed in future iterations of the model.

An additional limitation of our neural model is that the current dipole moment density produced by cortical spindles was based on empirical measurements, and the model only provided the timing, location and relative amplitude of the spindles. Current source density was calculated from sleep spindles recorded by 24 microcontacts spaced every 150 µm on center, traversing the cortical thickness from the pia to white matter (Hagler et al., 2018). The observed amplitude (~0.5 – ~2.0 nAm/mm^2) is consistent with physiologically plausible maximum current dipole moment densities (Murakami and Okada, 2015). An important extension of the model

would be to determine if this empirically determined value is consistent with that calculated in a detailed model of the columnar microstructure such as LFPy (Lindén et al., 2014) or the blue brain project (Markram, 2006). This calculation requires accurate reconstruction of dendritic domains, cell-densities and distributions, and synaptic terminations, in multi-compartment Hodgkin-Huxley models (Lindén et al., 2014). Such models are obviously too computationally expensive to incorporate directly into the many cortical patches in our model. However, an in-depth analysis of a single patch could help inform how well the limited number of cells we simulate in each patch represents the large number of actual cortical cells in that area.

The biophysical model used to propagate the cortical activity to the extracranial sensors also has limitations. We use a boundary element model which has been found to provide a good estimate of propagation at reasonable computational cost (Gramfort et al., 2010). Our model estimates four tissue-boundary 'shells' from each subject's structural MRI: pia/CSF; CSF/skull; skull/scalp; and scalp/air. Although other models commonly omit the CSF layer, simulations indicate that its inclusion produces greater smearing of the EEG (Irimia et al., 2012; Lopes da Silva, 2013). Within the layers we use accepted tissue conductivities for the brain, CSF, and scalp (Hallez et al., 2007). However, the *in vivo* electroconductive properties of the skull remain controversial and may vary significantly across subjects (Akalin Acar and Makeig, 2013; Awada et al., 1998; Hallez et al., 2007). The biophysical model used to generate synthetic ECoG was simpler still, and did not take into account the skull, which is reasonable given the proximity of the electrodes to the sources, and in addition the large craniotomy necessary for the array to be implanted. Furthermore, cranial nerve exits and other skull inhomogeneities may have significant effects (Akalin Acar and Makeig, 2013) which are unaccounted for in our model. Note that these issues will not affect MEG as, at the precision of biomedical analyses, the magnetic permeability of these tissues is equivalent to that of a vacuum (Hämäläinen et al., 1993).

The cortical surface used in the biophysical model is also reconstructed from each

individual subject's structural MRI (Dale et al., 1999). Extracranial M/EEG fields generated by a cortical dipole depend not only on its location and the magnitude of its moment, but are also highly dependent on the extent of spatial-temporal synchrony with other dipoles across the cortex and their relative orientations (Ahlfors et al., 2010a; Lutkenhoner, 2003). Dipoles are created by the post-synaptic currents of aligned pyramidal neurons oriented perpendicular to cortical surface (Lopes Da Silva, 2004; Nunez and Srinivasan, 2009). Thus, synchronous dipoles with opposed orientations, such as those on opposite side of the sulcal walls, will cancel each other out. In fact, the majority of the total cortical MEG signal is canceled before exiting the head on account of this phenomena (Ahlfors et al., 2010b; Lutkenhoner, 2003). Although the neural model contains only 20,484 cortical patches, their activity is mapped to 327,684 vertices for the biophysical model, which provides ~1 mm resolution. Our previous simulations indicate that this resolution better captures the summation and cancelation of simultaneously active dipoles than lower resolutions (Ahlfors et al., 2010b). The high-resolution cortical mesh also reduces the numerical integration errors that can be present in BEM forward models with small inter-shell distances. However the efficacy of even finer resolutions at capturing cancelation accurately and the extent of errors in cortical ribbon orientation reconstruction are unknown, as are their effects on modeled M/EEG.

Despite these limitations of our neural and biophysical models, they produced reasonable amplitudes and topographies in both EEG and MEG. The amplitude of the M/EEG is a powerful constraint reflecting the interaction of many parameters and we are not aware of a previous study which reproduces both with realistic parameters and cortical source topographies. The empirical MEG topography, in particular, is well-reproduced and shows the characteristic pattern (Dehghani et al., 2011b; Manshanden et al., 2002) of frontolateral gradiometer activation. The leadfields of MEG gradiometers are smaller than those of EEG (Irimia et al., 2012), primarily because EEG is smeared by the skull and cranial tissues whereas these structures are mostly transparent to MEG (Hämäläinen and Ilmoniemi, 1994), especially when

comparing bipolar MEG gradiometers to distantly referenced scalp EEG. Consequently, MEG is relatively more sensitive to focal sources whereas EEG to distributed (Irimia et al., 2012; Lopes da Silva, 2013). The core and matrix thalamo-cortical systems correspond to this pattern, with the core pathway terminating focally in layer 4 and the matrix more diffusely in superficial layers (Jones, 2002, 2001), leading to the hypothesis that core spindles would be relatively more prominent in MEG and matrix in EEG (Dehghani et al., 2010). We modeled the differential projections and terminations of the core and matrix systems and found support for this hypothesis.

Rotating ECoG wavefronts have been observed during sleep spindles and hypothesized to be a result of conduction delays in long range corticocortical connections (Muller er al., 2016). Our revised model was able to replicate the spatiotemporal dynamics of these waves but surprisingly found that excitatory corticocortical connectivity was not necessary to observe these patterns. They in fact appear to be primally driven by thalamic circuits whose activity is propagated to the cortex and perhaps modified by local inhibition. The limited role of corticocortical connections in the generation of sleep spindle spiral waves in the model may be due the simplified map-based neurons used in the cortex, as opposed to the detailed Hodgkin-Huxley neurons used the thalamus. In any case, our observations provide an alternative mechanism for how this phenomenon may arise.

In addition to the differing spatial extent of core and matrix spindles, their differing laminar distributions may also have an effect on their respective M/EEG signals. Laminar recordings in humans show that spindles can be dichotomized depending upon whether their LFP gradients are maximal in the middle versus superficial cortical layers, possibly corresponding to the core and matrix terminations of thalamocortical fibers (Hagler et al., 2018). The CSD calculated from the middle layer spindles produced a typical dipolar pattern with a current source and sink of approximately equal magnitude. However the superficial layer spindles consisted of a concentrated current sink and distributed or absent sources, yielding an

effectively monopolar current distribution. Apparent monopoles are often found when analyzing CSD but it is controversial whether these represent an experimental or analytic artifact or a physiological phenomenon, such as accumulated charge (Bedard and Destexhe, 2013; Destexhe and Bedard, 2012; Gratiy et al., 2013; Riera et al., 2012). Most commonly, spindles are a mixture of middle and superficial layer waves (Hagler et al., 2018), and we did not distinguish between them when calculating the current dipole moment densities, which therefore mainly reflected middle layer spindles. Static ion concentrations produce an EEG but no MEG signal, and thus accounting for them in the matrix spindles in our model would have accentuated the difference between MEG and EEG in the predicted direction (i.e., producing a better correspondence between model and empirical results). Furthermore, the EEG signal produced by monopolar or unbalanced dipole decreases with distance less quickly than that produced by ideal dipoles, and this would tend to increase the similarity of the modeled to the empirical EEG spindle topography at midline sites.

Our model can be easily extended to other M/EEG phenomena such as K-complexes (Mak-McCully et al., 2014), slow oscillations (Krishnan et al., 2018a ; Komarov et al., 2017; Wei et al., 2016) and theta bursts (Gonzalez et al., 2018) by marrying their neural computational models to the biophysical model described here. Using the same neural model to generate multiple M/EEG phenomena would provide a strong constraint on model parameters. Intracranial recordings may inform additional constraints, especially for the distribution, synchrony, and phase of cortical spindles (Halgren et al., 2018). Because the average spatial distribution of all spindles is much broader than that of individual spindles, the large-scale folding patterns of the cortex have a disproportionate impact on average spindle topographies. If simultaneous extra- and intra-cranial recordings are obtained, then the extracranial topography of individual spindles can be predicted by informing the model of the (limited) intracranial measures. This would permit predictions from individual spindles to be tested, rather than their grand average as was tested in the current paper.

A more comprehensive understanding of the relationship between neurobiology, local field potentials, and non-invasive M/EEG might plausibly improve the diagnostic power of the latter techniques. Here we have presented a framework that unifies detailed neural models with the measurement theory of M/EEG. Understanding the forward model that relates ion channel dynamics to M/EEG is the first step towards developing a principled inverse solution that maps M/EEG responses to clinically and physiologically relevant human *in vivo* molecular measures.

Acknowledgements

This work was supported by National Institute of Mental Health Grants 1RF1MH117155 and 5T32MH020002, and the National Institute of Neurological Disorders and Stroke Grant 1R01NS109553. We thank Nima Dehghani, Donald Hagler, and Sergey Gratiy for their contributions to the empirical data, as well as our human subjects for their participation. Data were provided, in part, by the Human Connectome Project, WU-Minn Consortium (Principal Investigators: David Van Essen and Kamil Ugurbil; 1U54MH091657) funded by the 16 National Institutes of Health (NIH) Institutes and Centers that support the NIH Blueprint for Neuroscience Research and by the McDonnell Center for Systems Neuroscience at Washington University.

Chapter 3, in part, is a reprint of the material as it appears in Rosen BQ, Krishnan GP, Sanda P, Komarov M, Sejnowski TJ, Rulkov N, Ulbert I, Eross L, Madsen J, Devinsky O, Doyle W, Fabo D, Cash S, Bazhenov M, Halgren E. 2019. Simulating human sleep spindle MEG and EEG from ion channel and circuit level dynamics. *J. Neurosci. Methods*, 316 46-57. The dissertation author was the primary investigator and author of this paper. In addition, chapter 3, in part, contains unpublished material coauthored with Yuri Sokolov, Jean Erik Delonois, Oscar Gonzalez, Giri Krisnan, and Maksim Bazhenov. The dissertation author was the primary author of this chapter.

References

Ahlfors SP, Han J, Belliveau JW, Hämäläinen MS. 2010a. Sensitivity of MEG and EEG to source orientation. Brain Topogr 23:227–232.
Ahlfors SP, Han J, Lin FH, Witzel T, Belliveau JW, Hämäläinen MS, Halgren E. 2010b. Cancellation of EEG and MEG signals generated by extended and distributed sources. Hum Brain Mapp 31:140–149.

Akalin Acar Z, Makeig S. 2013. Effects of forward model errors on EEG source localization. Brain Topogr 26:378–396.

Andrillon T, Nir Y, Staba RJ, Ferrarelli F, Cirelli C, Tononi G, Fried I. 2011. Sleep Spindles in Humans: Insights from Intracranial EEG and Unit Recordings. J Neurosci 31:17821–17834.

Awada K a, Jackson DR, Baumann SB, Williams JT, Wilton DR, Fink PW, Prasky BR. 1998. Effect of conductivity uncertainties and modeling errors on EEG source localization using a 2-D model. IEEE Trans Biomed Eng 45:1135–45.

Balasubramanian M, Polimeni JR, Schwartz EL. 2009. Exact geodesics and shortest paths on polyhedral surfaces. IEEE Trans Pattern Anal Mach Intell 31:1006–1016.

Bazhenov M, Rulkov NF, Timofeev I. 2008. Effect of synaptic connectivity on long-range synchronization of fast cortical oscillations. J Neurophysiol 100:1562–1575.

Bazhenov M, Timofeev I, Steriade M, Sejnowski T. 2000. Spiking-bursting activity in the thalamic reticular nucleus initiates sequences of spindle oscillations in thalamic networks. J Neurophysiol 84:1076–1087.

Bazhenov M, Timofeev I, Steriade M, Sejnowski TJ. 2002. Model of thalamocortical slow-wave sleep oscillations and transitions to activated States. J Neurosci 22:8691–8704.

Bedard C, Destexhe A. 2013. Reply to Gratiy et al. J Neurophysiol 109:1683–1683.

Bonjean M, Baker T, Bazhenov M, Cash S, Halgren E, Sejnowski T. 2012. Interactions between Core and Matrix Thalamocortical Projections in Human Sleep Spindle Synchronization. J Neurosci 32:5250–5263.

Bonjean M, Baker T, Lemieux M, Timofeev I, Sejnowski TJ, Bazhenov M. 2011. Corticothalamic Feedback Controls Sleep Spindle Duration In Vivo. J Neurosci 31:9124–9134.

Burt JB, Demirtaş M, Eckner WJ, Navejar NM, Ji JL, Martin WJ, Bernacchia A,
Anticevic A, Murray JD. 2018. Hierarchy of transcriptomic specialization across human cortex captured by structural neuroimaging topography. Nat Neurosci 21.

Chen J-Y, Chauvette S, Skorheim S, Timofeev I, Bazhenov M. 2012. Interneuron-mediated inhibition synchronizes neuronal activity during slow oscillation. J Physiol 590:3987–4010.

Cohen MX. 2017. Where Does EEG Come From and What Does It Mean? Trends Neurosci 40:208–218.

Cohen MX, Cavanagh JF, Slagter HA. 2011. Event-related potential activity in the basal ganglia differentiates rewards from nonrewards: Temporospatial principal components analysis and source localization of the feedback negativity: Commentary. Hum Brain Mapp 32:2270–2271.

Contreras D, Destexhe A, Sejnowski TJ, Steriade M. 1996. Control of spatiotemporal coherence of a thalamic oscillation by corticothalamic feedback. Science 274:771–774.

Costa MS, Weigenand A, Ngo HV V, Marshall L, Born J, Martinetz T, Claussen JC. 2016. A Thalamocortical Neural Mass Model of the EEG during NREM Sleep and Its Response to Auditory Stimulation. PLoS Comput Biol 12:1–20.

Dale AM, Fischl B, Sereno MI. 1999. Cortical surface-based analysis. I. Segmentation and surface reconstruction. Neuroimage 9:179–94.

Dehghani N, Cash SS, Halgren E. 2011a. Emergence of synchronous EEG spindles from asynchronous MEG spindles. Hum Brain Mapp 32:2217–2227.

Dehghani N, Cash SS, Halgren E. 2011b. Topographical frequency dynamics within EEG and MEG sleep spindles. Clin Neurophysiol 122:229–235.

Dehghani N, Cash SS, Rossetti AO, Chen CC, Halgren E. 2010. Magnetoencephalography Demonstrates Multiple Asynchronous Generators During Human Sleep Spindles. J Neurophysiol 104:179–188.

Delorme A, Makeig S. 2004. EEGLAB: an open source toolbox for analysis of single-trial EEG dynamics including independent component analysis. J Neurosci Methods 134:9–21.

Destexhe A., Bal T, McCormick DA, Sejnowski TJ. 1996. Ionic mechanisms underlying synchronized oscillations and propagating waves in a model of ferret thalamic slices. J Neurophysiol.

Destexhe A, Bedard C. 2012. Do neurons generate monopolar current sources? J Neurophysiol 108:953–955.

Destexhe A, Contreras D, Steriade M. 1998. Mechanisms underlying the synchronizing action of corticothalamic feedback through inhibition of thalamic relay cells. Am Physiol Soc.

Destexhe Alain, Contreras D, Steriade M, Sejnowski TJ, Huguenard JR. 1996. In vivo, in vitro, and computational analysis of dendritic calcium currents in thalamic reticular neurons. J Neurosci 16:169–85.

Diekelmann S, Born J. 2010. The memory function of sleep. Nat Rev Neurosci 11:114–126.

Einevoll GT, Kayser C, Logothetis NK, Panzeri S. 2013. Modelling and analysis of local field potentials for studying the function of cortical circuits. Nat Rev Neurosci 14:770–785.

Fischl B. 2012. FreeSurfer. Neuroimage.

Fischl B, Sereno MI, Tootell RBH, Dale AM. 1999. High-resolution intersubject averaging and a coordinate system for the cortical surface. Hum Brain Mapp 8:272–284.

Fisher NI. 1995. Statistical analysis of circular data. Cambridge University Press.

Frauscher B, von Ellenrieder N, Dubeau F, Gotman J. 2015. Scalp spindles are associated with widespread intracranial activity with unexpectedly low synchrony. Neuroimage 105:1–12.

Glasser MF, Coalson TS, Robinson EC, Hacker CD, Harwell J, Yacoub E, Ugurbil K, Andersson J, Beckmann CF, Jenkinson M, Smith SM, Van Essen DC. 2016. A multi-modal parcellation of human cerebral cortex. Nature 536:171–8.

Glasser MF, Van Essen DC. 2011. Mapping Human Cortical Areas In Vivo Based on Myelin Content as Revealed by T1- and T2-Weighted MRI. J Neurosci 31:11597–11616.

Gonzalez CE, Mak-McCully RA, Rosen BQ, Cash SS, Chauvel PY, Bastuji H, Rey M, Halgren E. 2018. Theta bursts precede, and spindles follow, cortical and thalamic downstates in human NREM sleep. *J Neurosci*, 38 (46) 9989-10001.

Gramfort A, Papadopoulo T, Olivi E, Clerc M. 2010. OpenMEEG: opensource software for quasistatic bioelectromagnetics. Biomed Eng Online 9:45.

Gratiy SL, Pettersen KH, Einevoll GT, Dale AM. 2013. Pitfalls in the interpretation of multielectrode data: on the infeasibility of the neuronal current-source monopoles. J Neurophysiol 109:1681–1682.

Hagler DJ, Ulbert I, Wittner L, Erőss L, Madsen JR, Devinsky O, Doyle W, Fabo D, Cash SS, Halgren E. 2018. Heterogeneous origins of human sleep spindles in different cortical layers. J Neurosci 38:2241–17.

Halgren M, Fabó D, Ulbert I, Madsen JR, Erőss L, Doyle WK, Devinsky O, Schomer D, Cash SS, Halgren E. 2018. Superficial Slow Rhythms Integrate Cortical Processing in Humans. Sci Rep 8:2055.

Hallez H, Vanrumste B, Grech R, Muscat J, De Clercq W, Vergult A, D'Asseler Y, Camilleri KP, Fabri SG, Van Huffel S, Lemahieu I. 2007. Review on solving the forward problem in EEG source analysis. J Neuroeng Rehabil 4:46.

Hämäläinen MS, Hari R, Ilmoniemi RJ, Knuutila J, Lounasmaa O V. 1993. Magnetoencephalography - theory, instrumentation, and applications to noninvasivee studies of the working human brain. Rev Mod Phys.

Hämäläinen MS, Ilmoniemi RJ. 1994. Interpreting magnetic fields of the brain: minimum norm estimates. Med Biol Eng Comput 32:35–42.

Huguenard JR, McCormick DA. 1992. Simulation of the currents involved in rhythmic oscillations in thalamic relay neurons. J Neurophysiol 68:1373–1383.
Huguenard JR, Prince DA. 1992. A novel T-type current underlies prolonged Ca2+-dependent burst firing in GABAergic neurons of rat thalamic reticular nucleus. J Neurosci 12:3804–3817.

Iber C, Ancoli-Israel S, Chesson A, Quan S. 2007. The AASM Manual for the Scoring of Sleep and Associates Events: Rules, Terminology and Technical Specifications, Sleep (Rochester).

Irimia A, Van Horn JD, Halgren E. 2012. Source cancellation profiles of electroencephalography and magnetoencephalography. Neuroimage 59:2464–2474.

Jammalamadaka SR, Sengupta A. 2001. Topics in circular statistics. World Scientific.

Jones EG. 2002. Thalamic circuitry and thalamocortical synchrony. Philos Trans R Soc B Biol Sci 357:1659–1673.

Jones EG. 2001. The thalamic matrix and thalamocortical synchrony. Trends Neurosci.

Klopp J, Marinkovic K, Chauvel P, Nenov V, Halgren E. 2000. Early widespread cortical distribution of coherent fusiform face selective activity. Hum Brain Mapp 11:286–293.

Komarov M, Krishnan G, Chauvette S, Rulkov N, Timofeev I, Bazhenov M. 2017. New class of reduced computationally efficient neuronal models for large-scale simulations of brain dynamics. J Comput Neurosci 1–24.

Krishnan GP, Chauvette S, Shamie I, Soltani S, Timofeev I, Cash SS, Halgren E, Bazhenov M. 2016. Cellular and neurochemical basis of sleep stages in the thalamocortical network. Elife 5:1–29.

Krishnan GP, González OC, Bazhenov M. 2018a. Origin of slow spontaneous resting-state neuronal fluctuations in brain networks. Proc Natl Acad Sci 201715841.

Krishnan GP, Rosen BQ, Chen J-Y, Muller L, Sejnowski TJ, Cash SS, Halgren E, Bazhenov M. 2018b. Thalamocortical and intracortical laminar connectivity determines sleep spindle properties. PLoS Comput Biol 14:1–22.

Kybic J, Clerc M, Abboud T, Faugeras O, Keriven R, Papadopoulo T. 2005. A common formalism for the integral formulations of the forward EEG problem. IEEE Trans Med Imaging 24:12–28.

Lindén H, Hagen E, Łęski S, Norheim ES, Pettersen KH, Einevoll GT. 2014. LFPy: a tool for biophysical simulation of extracellular potentials generated by detailed model neurons. Front Neuroinform.

Lindén H, Tetzlaff T, Potjans TC, Pettersen KH, Grun S, Diesmann M, Einevoll GT. 2011. Modeling the spatial reach of the LFP. Neuron 72:859–872.

Lopes da Silva F. 2013. EEG and MEG: Relevance to neuroscience. Neuron 80:1112–1128.

Lopes Da Silva F. 2004. Functional localization of brain sources using EEG and/or MEG data: Volume conductor and source modelsMagnetic Resonance Imaging. pp. 1533–1538. Lutkenhoner B. 2003. Magnetoencephalography and its Achilles' heelJournal of Physiology Paris. pp. 641–658.

Mak-McCully R a, Rosen BQ, Rolland M, Régis J, Bartolomei F, Rey M, Chauvel P, Cash SS, Halgren E. 2015. Distribution, Amplitude, Incidence, Co-Occurrence, and Propagation of Human K-Complexes in Focal Transcortical Recordings. eNeuro 2.

Mak-McCully RA, Deiss SR, Rosen BQ, Jung KY, Sejnowski TJ, Bastuji H, Rey M, Cash SS, Bazhenov M, Halgren E. 2014. Synchronization of Isolated Downstates (K-Complexes) May Be Caused by Cortically-Induced Disruption of Thalamic Spindling. PLoS Comput Biol 10.

Mak-Mccully RA, Rolland M, Sargsyan A, Gonzalez C, Magnin M, Chauvel P, Rey M, Bastuji H, Halgren E. 2017. Coordination of cortical and thalamic activity during non-REM sleep in humans. Nat Commun 8.

Manoach DS, Pan JQ, Purcell SM, Stickgold R. 2016. Reduced Sleep Spindles in Schizophrenia: A Treatable Endophenotype That Links Risk Genes to Impaired Cognition? Biol Psychiatry 80:599–608.

Manshanden I, De Munck JC, Simon NR, Lopes da Silva FH. 2002. Source localization of MEG sleep spindles and the relation to sources of alpha band rhythms. Clin Neurophysiol 113:1937–1947.

Markov NT, Vezoli J, Chameau P, Falchier A, Quilodran R, Huissoud C, Lamy C, Misery P, Giroud P, Ullman S, Barone P, Dehay C, Knoblauch K, Kennedy H. 2014. Anatomy of hierarchy: Feedforward and feedback pathways in macaque visual cortex. J Comp Neurol 522:225–259.

Markram H. 2006. The Blue Brain Project. Nat Rev Neurosci.

McCormick DA, Pape HC. 1990. Properties of a hyperpolarization-activated cation current and its role in rhythmic oscillation in thalamic relay neurones. J Physiol 431:291–318.

Meyer M, Desbrun M, Schröder P, Barr AH. 2003. Discrete Differential-Geometry Operators for Triangulated 2-Manifolds. pp. 35–57.

Muller L, Piantoni G, Koller D, Cash SS, Halgren E, Sejnowski TJ. 2016. Rotating waves during human sleep spindles organize global patterns of activity that repeat precisely through the night. Elife 5:1–16.

Murakami S, Okada Y. 2015. Invariance in current dipole moment density across brain structures and species: Physiological constraint for neuroimaging. Neuroimage 111:49–58.

Nunez PL, Srinivasan R. 2009. Electric Fields of the Brain: The neurophysics of EEG, Electric Fields of the Brain: The neurophysics of EEG.

Oostenveld R, Fries P, Maris E, Schoffelen J-M. 2011. FieldTrip: Open source software for advanced analysis of MEG, EEG, and invasive electrophysiological data. Comput Intell Neurosci 2011:156869.

Pettersen KH, Devor A, Ulbert I, Dale AM, Einevoll GT. 2006. Current-source density estimation based on inversion of electrostatic forward solution: Effects of finite extent of neuronal activity and conductivity discontinuities. J Neurosci Methods 154:116–133.

Piantoni G, Halgren E, Cash SS. 2016. Spatiotemporal Characteristics of Sleep Spindles Depend on Cortical Location. Neuroimage 146:236–245.

Riera JJ, Ogawa T, Goto T, Sumiyoshi A, Nonaka H, Evans A, Miyakawa H, Kawashima R. 2012. Pitfalls in the dipolar model for the neocortical EEG sources. J Neurophysiol 108:956–975.

Ripke S, Neale BM, Corvin A, Walters JTR, Farh K-H, Holmans PA, Lee P, Bulik-Sullivan B, Collier DA, Huang H. 2014. Biological insights from 108 schizophrenia-associated genetic loci. Nature 511:421.

Ritter P, Schirner M, McIntosh AR, Jirsa VK. 2013. The virtual brain integrates computational modeling and multimodal neuroimaging. Brain Connect 3:121–145.

Rockland KS. 2019. What do we know about laminar connectivity?. Neuroimage 197:772-784.

Rosen BQ, Halgren E. 2021. A whole-cortex probabilistic tractography connectome. eNeuro 8 (1).

Rulkov NF, Bazhenov M. 2008. Oscillations and synchrony in large-scale cortical network models. J Biol Phys 34:279–299.

Rulkov NF, Timofeev I, Bazhenov M. 2004. Oscillations in Large-Scale Cortical Networks : Map-Based Model. J Comput Neurosci 17:203–223.

Sejnowski TJ, Destexhe A. 2000. Why do we sleep? Brain Res 886:208–223.
Smith SM, Beckmann CF, Andersson J, Auerbach EJ, Bijsterbosch J, Douaud G, Duff E,

Feinberg DA, Griffanti L, Harms MP, Kelly M, Laumann T, Miller KL, Moeller S, Petersen S, Power J, Salimi-Khorshidi G, Snyder AZ, Vu AT, Woolrich MW, Xu J, Yacoub E, Uğurbil K, Van Essen DC, Glasser MF. 2013. Resting-state fMRI in the Human Connectome Project. Neuroimage 80:144–168.

Steriade M, McCormick D, Sejnowski T. 1993. Thalamocortical oscillations in the sleeping and aroused brain. Science 262:679–685.

Stevens CF. 1993. Quantal release of neurotransmitter and long-term potentiation. Cell.

Timofeev I, Bazhenov M, Sejnowski TJ, Steriade M. 2001. Contribution of intrinsic and synaptic factors in the desynchronization of thalamic oscillatory activity. Thalamus Relat Syst 1:53–69.

Timofeev I, F. G, Bazhenov M, Sejnowski TJ, Steriade M. 2000. Origin of Slow Cortical Oscillations in Deafferented Cortical Slabs. Cereb Cortex 10:1185–1199.

Tsodyks M V, Markram H. 1997. The neural code between neocortical pyramidal neurons depends on neurotransmitter release probability. Proc Natl Acad Sci 94:719–723.

Ulbert I, Halgren E, Heit G, Karmos G. 2001. Multiple microelectrode-recording system for human intracortical applications. J Neurosci Methods 106:69–79.

Uutela K, Taulu S, Hämäläinen M. 2001. Detecting and correcting for head movements in neuromagnetic measurements. Neuroimage 14:1424–1431.

Van den Heuvel MP, Sporns O. 2013. An Anatomical Substrate for Integration among Functional Networks in Human Cortex. J Neurosci 33:14489–14500.

Wamsley EJ, Tucker MA, Shinn AK, Ono KE, McKinley SK, Ely A V., Goff DC, Stickgold R, Manoach DS. 2012. Reduced sleep spindles and spindle coherence in schizophrenia: Mechanisms of impaired memory consolidation? Biol Psychiatry 71:154–161.

Wei Y, Krishnan GP, Bazhenov M. 2016. Synaptic Mechanisms of Memory Consolidation during Sleep Slow Oscillations. J Neurosci 36:4231–4247.

CHAPTER 4: FREQUENCY-RESOLVED FALLOFF OF SPONTANEOUS CORTICAL COHERENCE WITH DISTANCE IN HUMAN COMPOSITE SEEG

Abstract

A map of cortical functional connectivity with high temporal and spatial resolution remains an elusive goal in human neuroscience. Functional magnetic resonance imaging (fMRI) is only sensitive to low frequency activity, Magneto- and electro-encephalography (M/EEG) sensors have significant spurious correlation due to overlapping sensor lead fields and the localization of these signals' sources relies on assumptions about spatial correlativity that have little experimental validation. In contrast, human stereo-electro-encephalographic depth-electrode recordings (SEEG) provide focal, true-scale measurements of transcortical potentials. However, due to limited implant coverage, standard SEEG analyses can miss the larger-scale cortical patterns integral to commonly observed cognitive and neural phenomena. To address this limitation, SEEG data during randomly sampled periods of wake and non-REM sleep from more than 200 patients from seven clinical sites was integrated in a model of frequency-resolved spontaneous coherence as a function of the white matter fiber distance between implanted cortical parcels. We find that within-patient coherence rapidly reaches a steady state, and that inter-electrode coherence decays exponentially with fiber-tract distance. Coherence below ~15Hz is higher and decays more slowly with distance in NREM sleep compared to waking. Coherence decays more slowly at lower frequencies, and for the characteristic frequency bands of sleep graphoelements. We find furthermore, that at all frequencies and distances, spontaneous coherence is greater than would be expected by chance and that its rate of decays is less than that of anatomical connectivity. Lasty, we present a case study showing that the assumed rate of falloff in synchrony between cortical sources with distance has dramatic effects on the source localization of extracranial recordings. While the scope of these estimates may be limited by the brain states and patient population explored, the empirical characterizations of neural correlativity as a function of distance presented here, being

frequency-resolved, volume-conduction-insensitive, and having broad spatial coverage, offer a unique view of human neural activity.

Introduction

As the neuroscience community has been able to record from more and more neural elements simultaneously there has been commensurately increased interest in how these signals covary among elements and more generally across space. Modeling the brain as a network of connections is a foundational framework for understanding its meso- and macro-scale neurobiology (Sporns et al., 2005). Functional connectivity, or physiological correlativity, while necessarily constrained by anatomical connectivity, cannot be fully predicted by it and may be more relevant for behavior (Honey et al., 2009). As a practicality, most human studies of neural correlativity rely on non-invasive methodologies, which introduce particular confounds when assessing multivariate covariability as opposed to more common univariate measures, e.g., amplitude and frequency. In this report we present an analysis of spontaneous corticocortical coherence as a function of distance as measured with intracranial transcortical stereo-electroencephalography (SEEG).

The post-synaptic currents of oriented cortical pyramidal neurons result in electromagnetic fields which are instantaneously conducted through the media of the head to distant locations. Sensors far from cortical generators, such as scalp EEG or magnetoencephalography (MEG) have broad leadfields, which is to say that the activity in relatively large area of cortex has a non-negligible contribution to each sensor's signal. Much sensor covariability is therefore spurious, being the result of the same generator being recorded simultaneously by multiple sensors (Nolte et al., 2004; Nunez and Srinivasan, 2009). Even in intracranial electrocorticography, or ECoG, where electrodes lie directly on the cortex, a degree of spurious correlativity is introduced via the common reference electrode. This can be ameliorated with common average referencing, but this procedure distorts the signal in other

ways, such as by assuming implausible zero-sum amplitude across channels. In this study we used a depth SEEG arrays with transcortical bipolar referencing, resulting in unambiguously focal recordings with minimum spurious correlation between sensors (Arnulfo et al., 2015; Mak-McCully et al., 2014). The disadvantage of transcortical SEEG is that spatial coverage is sparse and wholly clinically determined, but we have lessened that drawback by compositing recordings from more than 200 patients across multiple clinical sites. Alternatively, functional magnetic resonance imaging (fMRI) while having near-complete cortical coverage and high spatial resolution, is related only indirectly to neural activity and is in any case not temporally precise enough to measure spectral differences in most biologically relevant frequencies.

As the cortex of each intracranial EEG patient is sparsely but variably sampled, compositing data from many patients is a logical avenue to produce a more wholistic picture. Studies of this type typically relate univariate metrics, such as peak frequencies in continuous spontaneous recordings (Frauscher et al., 2018) or the characteristics of sleep graphoelements (Dickey et al., 2022; Gonzalez et al., 2022; von Ellenrieder et al., 2020), rather than bi- or multi-variate metrics which depend on the correlativity between sensors or ultimately brain areas. Achieving substantial bivariate coverage requires a very large patient sample, as the number of cortical region pairs scales with the square of the number of defined regions, and these pairs must be observed in the same patients to estimate correlative metrics.

In this study we principally use magnitude squared coherence as a measure of functional connectivity between cortical signals. The measure is simple, computationally efficient, robust to transients, and frequency specific. More fundamentally, it has a deep relationship to a Bayesian understanding of neural activity. Coherence is the normalized modulus of the complex cross-spectrum between two signals, which itself is the frequency domain extension of covariance. From a practical perspective, an assumed prior variance-covariance matrix (Dale and Sereno, 1993) or autospectral-cross-spectral matrix (Frei et al., 2001) of neural generators may be used with of the equivalent matrix for extracranial sensors (M/EEG)

to constrain the inversion of the linear volume conduction operator and thus predict the neural activity that causes the observed recording to arise. This maximum a posteriori probability estimate is the essence of a family of commonly used linear methods of source localization (López et al., 2014; Wipf and Nagarajan, 2009). More theoretically, covariance matrix or cross-spectral matrices form a key parameter that defines the multivariate mixed Gaussian probability distributions that make up proposed internal generative models in the Bayesian brain framework (Friston, 2012).

For reasons of wiring minimization and modularity, one would expect that the degree of functional connectivity between neural elements would decrease with the distance between them. The density of corticocortical structural connections falls off rapidly with distance, with exponential distance rules observed for meso-scale histological tracings in monkeys (Ercsey-Ravasz et al., 2013; Nikola T. Markov et al., 2013) and diffusion MRI (dMRI) tractography in monkeys and humans (Donahue et al., 2016; Rosen and Halgren, 2021). At the microscale (< 0.3 mm) in humans, there is some elevated local connectively before the rapid decline, resulting in a Gaussian falloff in projections (Campagnola et al., 2022). Quantitatively, direct comparisons of fit parameters are complicated by the differing definitions of distance used in each study. Ideally, the length of the fiber trajectories is preferrable because that is the distance that action-potentials need to traverse between cortical locations at the mesoscale. However, complete distance-connectomes (i.e., streamline lengths between cortical locations) have only recently become available (Rosen and Halgren, 2021), and then only between cortical parcel centroids, which distorts shorter distances. Alternatively, while Euclidean distances are simple to calculate, they become implausible at longer distances. In this study we have elected to use the fiber distances between the parcels the transcortical electrodes occupy.

This report presents an estimation of the falloff in coherence with distance and frequency using a composite SEEG approach with bipolar transcortical referencing to ensure truly focal recordings. We find that coherence decreases exponentially with fiber distance and that rate of

falloff is frequency dependent. We report reduced distance-related decay in the frequencies that are characteristic of sleep grapholements (spindles, theta bursts, and slow oscillations). We also observe synchrony greater than would be expected by chance even at long distances and high frequencies. Lastly, we briefly demonstrate that the assumed rate of falloff can meaningfully alter M/EEG source localization estimates.

Materials and Methods

Patients and intracranial recordings

Continuous spontaneous stereo-electroencephalography telemetry and structural imaging were obtained for 298 patients undergoing pre-resection intracranial monitoring for phamaco-resistant focal epilepsy at University of California, San Diego Medical Center, La Jolla CA, the Cleveland Clinic, Cleveland OH, Oregon Health and Science University Hospital, Portland OR, Massachusetts General Hospital, Boston MA, Brigham and Women's Hospital, Boston MA, the Hospital of the University of Pennsylvania, Philadelphia PA, and The University of Alabama Birmingham Hospital, Birmingham AL. These clinical data are recorded as standard of care and written informed consent, approved by each institution's review board, was obtained from each patient before the data were used for research purposes. Recordings were collected with a Nihon Kohen Neurofax (the Cleveland Clinic), Cadwell Arc (Oregon Health and Science University Hospital), or Natus Quantum amplifier (all other clinical sites) and acquired with a sampling frequency of at least 500 Hz. After preliminary inspection, 27 patients with prior resections, highly abnormal sleep patterns, or whose data were over-contaminated with excessive epileptiform activity or technical artifacts were excluded from analysis. A further 35 patients were excluded from further analysis after channel selection and quality control procedures, described below, resulted in them having with fewer than two clean bipolar channel pairs. After quality control, 236 patients (126 female, 101 male, 9 unknown, 36.5 ± 13.3 (mean ± stdev.) years old, 22 unknown age) were included in the final analysis.

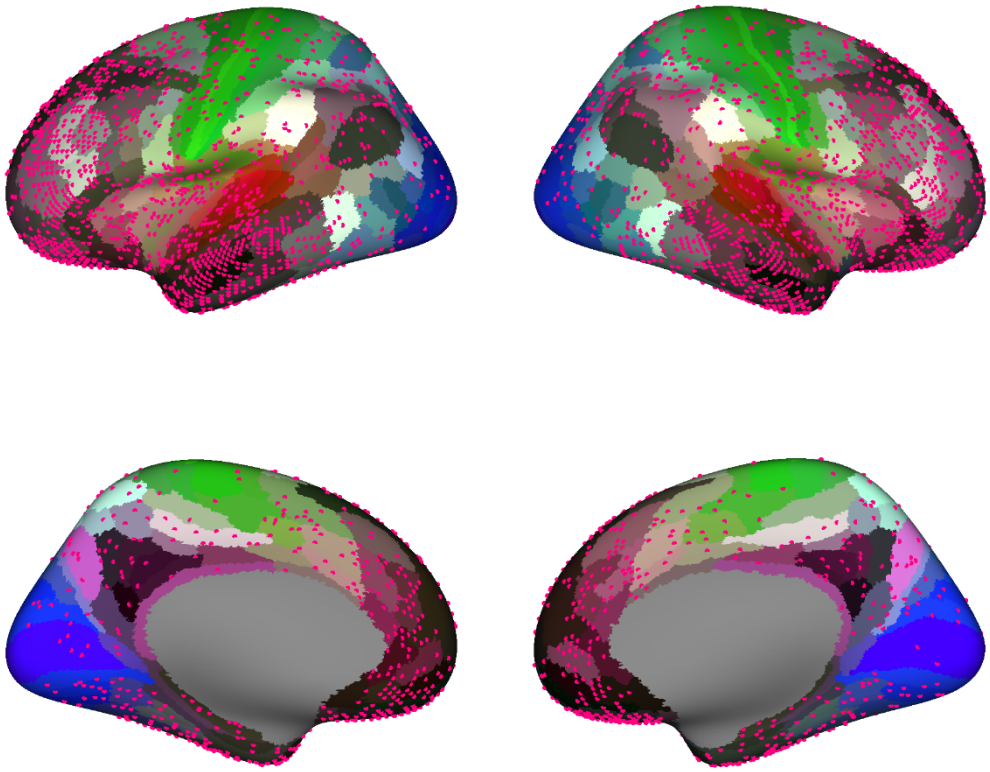

Figure 4.1 Electrode positions. Locations of 3,588 bipolar electrodes displayed on the inflated fsaverage template surface with the HCP-MMP parcellation scheme overlayed in color.

Channel localization and inter-channel distance

For each patient a pre-operative T1-weighted high-resolution structural MRI and inter-operative CT scan were obtained as standard of care. SEEG contacts were localized analogously to (Yang et al., 2012). The post-implant CT volume was co-registered to the pre-implant MR volume in standardized 1mm isotropic FreeSurfer space with the general registration module (Johnson et al., 2007) in 3D Slicer (Fedorov et al., 2012) and each contact's position was determined by manually marking the contact centroid as visualized in the co-registered CT volume. Cortical surfaces were reconstructed from the MR volume with the FreeSurfer recon-all pipeline (Fischl, 2012). Each transcortical bipolar channel was assigned to the white-gray surface

vertex nearest to the midpoint of the adjacent contacts. Spherical surface registration (Fischl et al., 1999) was used to map the individual subjects' bipolar channel vertices to the standardized fsaverage ico7 (Fischl, 2012) and 32k_FS_LR grayordinate (Marcus et al., 2013) atlases as well as to parcels of the HCP-MMP parcellation scheme (Glasser et al., 2016). The HCP-MMP parcel assignments of each channel were used to determine the approximate white matter fiber length of the connection between them, using the mean values for a cohort of 1,065 healthy subjects we have previously reported (Rosen and Halgren, 2021).

Telemetry preprocessing and channel selection

On average a total of 185.3 ± 112.0 hours of raw telemetry were analyzed for each patient. Data were anti-aliased at 250 Hz and resampled to 500 Hz. To remove line noise, a notch filter was applied at 60, 120, 180, and 240 Hz. On each electrode shaft, data were re-referenced to a bipolar scheme by taking the difference of potentials in adjacent contacts, yielding 30,769 total channels. Contact pairs were selected such that no two pairs shared a contact in order to ensure that bipolar channels were independent, eliminating just under half of all channels from further consideration. Peaks in the delta band (0.5-2 Hz) signal during high-delta periods were identified and the peri-delta-peak high-gamma band (70-190 Hz) envelope obtained. Transcortical contact pairs were identified by (1) having a midpoint close to the gray-matter–white-matter interface (<5 mm), (2) having a high anticorrelation between the delta-band amplitude and the high gamma band (70-190 Hz) envelope during delta-band peaks, indicative of non-pathological downstates with a surface-negative LFP deflection that quieted spiking, and (3) having high delta-band amplitude with and average delta peak of at least 40 μV, indicative of robust inversion in adjacent contacts. Only contacts with 5 mm pitch were analyzed in order to standardize absolute bipolar amplitudes and contact pairs located deep in the white matter or in subcortical gray matter were excluded from analysis. All channels were visually inspected to ensure they contained broadly normal non-pathological waveforms. This

procedure yielded 4,903 candidate channels which underwent wake and NREM scoring, described below, yielding 64.5 ± 51.6 hours of putatively clean scored wake and 9.2 ± 7.8 hours of putatively clean scored NREM sleep. After scoring, which excluded continuous periods of artifactual or pathological signals, remaining epileptogenic activity was detected with spike template convolution and gross artifacts, with amplitudes > 300 μV. Channels which contained persistent automatically detected interictal spikes or gross artifacts were removed from further analysis, yielding 3,665 channels. Periods containing interictal spikes or gross artifacts in any channel were excluded from analysis in all channels which removed < 30 seconds on average of wake and NREM from consideration in channels with rare interictal activity. Finally, after cross-spectral matrices were obtained for each subject as described below, channels with autospectral power more than 3 standard deviations above the pooled channelwise mean in any examined frequency were excluded, leaving 3,588 channels and 37,123 within-patient bivariate channel pairs in the final analysis.

Wake and NREM selection

For each patient, clean periods of sleep and wake were first manually classified based on ultradian delta power. Within manually-identified nightly periods of sleep, NREM sleep was automatically identified by the presences of slow oscillations (SOs) in a manner derived from standard clinical procedures (Iber et al., 2007). In 30-second frames, the density of SOs was ascertained in each 30-second frame and NREM marked for the frame if at least 35% of the frame contained SOs in at least one bipolar channel. The reduction in the number of channels and increase in the % of frame threshold relative to the clinical standard of 20% of the frame across scalp channels was to accommodate the increased spatial heterogeneity of sleep graphoelements observed intracranially, relative to the scalp (Mak-Mccully et al., 2017). For this purpose, slow waves were automatically detected with the method described in (Mak-Mccully et al., 2017), briefly, consecutive delta-band zero-crossings occurring within 0.23-3 s were detected and the top 20% of peaks were retained as SOs. Only wake and NREM periods without

detected interictal spikes or gross artifacts in any bipolar channel were included in subsequent analysis.

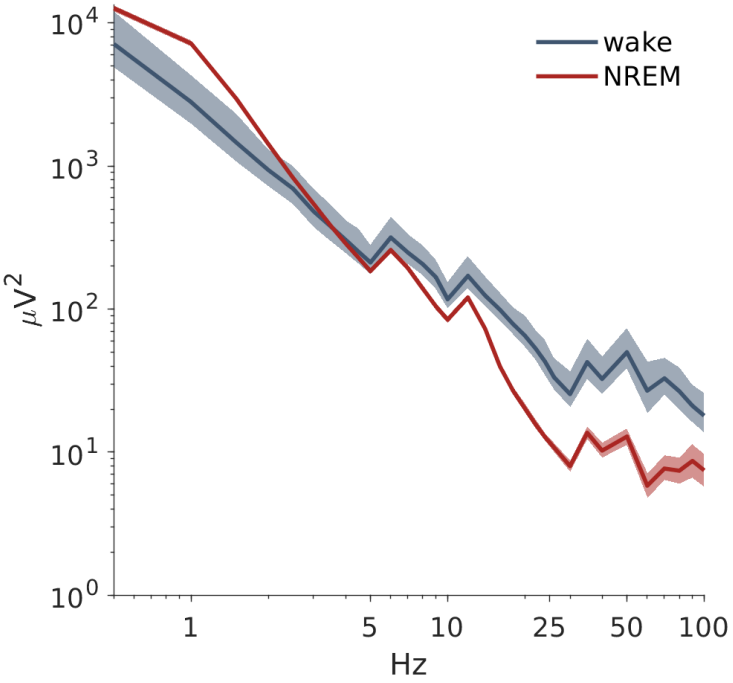

Figure 4.2 Grand average power spectra. Bootstrapped 95% confidence intervals across all pooled channels are overlayed.

Signal processing and epoch sampling

A frequency resolved map of each patient's neural covariability was achieved by estimating the complex cross-spectral matrix among bipolar SEEG channels. Narrow-band signals were extracted with a series of second-order resonator filters (matlab's iirpeak) with peaks and 3 dB attenuation bandwidths shown in Tables 4.1 and 4.2. For each narrowband frequency the complex analytic signal was extracted via the Hilbert transform. Calculating the variance-covariance matrix of analytic signals yields the cross-spectral matrix for each frequency. Cross-spectral matrices were normalized into magnitude-squared coherence by squaring the complex modulus of each cross-pairwise cross-spectrum and dividing by the product of the constituent autospectra.

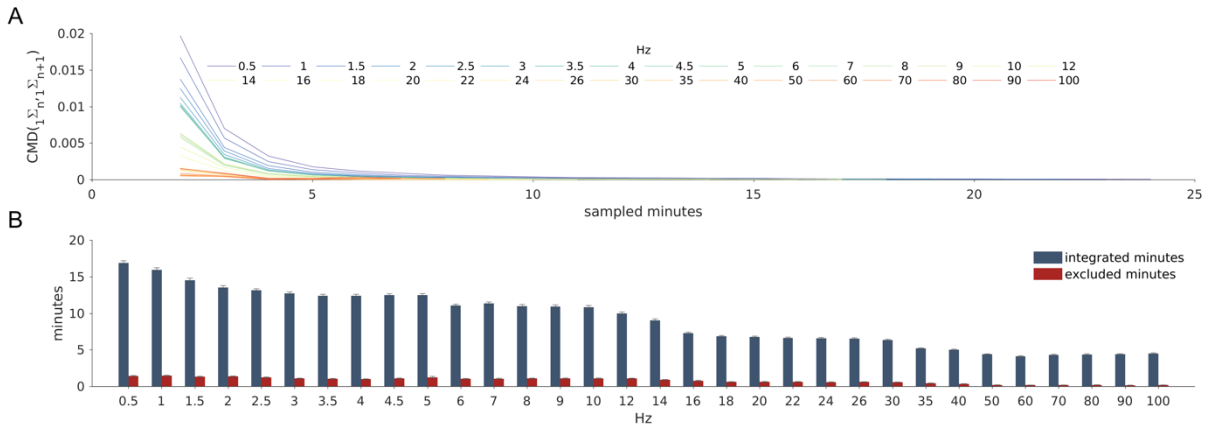

Figure 4.3 Convergence of coherence matrices. (A) Average correlation matrix distance between cumulative coherence matrix with n sampled minutes and n+1 sample minutes. Traces end at minute totals where 95% of patients' matrices have converged. Cool colors indicate lower frequencies and warm colors higher frequencies. (B) average integrated to convergence per frequency. Mean totals of minutes rejected as out outliers are also shown. Error bars indicate standard error of the mean. Data shown are for NREM sleep.

An adaptive procedure was used in order to obtain stable representative estimates of spontaneous covariability for each patient. Continuous minutes of telemetry were iteratively sampled at random, without replacement, from artifact-free wake and NREM sleep. Sampled minutes of telemetry were appended and prepended with 1.5 seconds of data for filtering and analytic signal extraction. These data were removed prior to covariance estimation to avoid edge artifacts. For each frequency, the coherence matrices were obtained as described above for the incoming minute, ${}_{n+1}\Sigma_{n+1}$, the cumulatively sampled telemetry, ${}_{1}\Sigma_{n+1}$, and, for the second sampled minute onward, the prior cumulatively sampled telemetry, ${}_{1}\Sigma_{n}$. The correlation matrix distance (CMD) (Herdin et al., 2005), was calculated between ${}_{1}\Sigma_{n}$ and ${}_{1}\Sigma_{n+1}$, and between ${}_{1}\Sigma_{n}$ and ${}_{n+1}\Sigma_{n+1}$. Starting with the third sampled minute, incoming minutes were rejected if the CMD between ${}_{1}\Sigma_{n}$ and ${}_{n+1}\Sigma_{n+1}$, was more than 3 standard deviations greater than average CMD between ${}_{1}\Sigma_{n}$ and ${}_{n+1}\Sigma_{n+1}$ for all previously sampled minutes. The coherence matrix was considered to have converged when the CMD between ${}_{1}\Sigma_{n}$ and ${}_{1}\Sigma_{n+1}$ was less than $1x10^{-5}$ and the cumulative cross-spectral matrix was then retained. The average duration of data integrated for each frequency before reaching convergence is shown in Tables 4.1 and 4.2. In

order to dilute the influence of the first sampled minute, this procedure was repeated ten times and the mean of the resulting cross-spectral matrices was used for subsequent analyses.

Statistical analyses and model fitting

As controls we estimated, for each frequency and state, the degree of coherence that could be expected by chance, with and without preserving the autocorrelational properties of the data. A Monte Carlo permutation procedure was used to estimate the degree of coherence resulting from shared autocorrelational properties between channels and that expected by chance. For the estimate of shared autocorrelation derived coherence, 100 random sets of lags were introduced to the channels for each data sampling iteration, for 1000 total lag permutation iterations. The resulting cross-spectral and coherence matrices for each iteration were then calculated. Introducing random lags to each channel preserves each channels univariate properties (e.g., variance, kurtosis), as well as it's autocorrelational properties but abolishes the covariance between channels that is due to true synchrony. For the estimate of coherence expected by chance when autocorrelation is not in play, the order of time samples in each channel was randomly permuted in each iteration, still preserving each channels univariate statistics but abolishing coherence due to both shared autocorrelational properties and true synchrony. For both shuffling methods the resulting cross-spectral and coherence matrices for each iteration were calculated to form null distributions which are shown in Figures 4.6 and 4.7. These procedures were repeated for each patient, narrowband frequency and behavioral state.

The effect of inter-electrode white matter fiber distance was assessed by fitting a linear mixed-effects model: log(coherence) ~ distance + 1 + (1 | patient), taking into account the fixed effects of the predictor variable distance and an intercept term, as well the random effect intercept term grouped by individual. Because of the natural log transformation of the response variable coherence, the linear model is equivalent to an exponential model for the untransformed distance predictor. Therefore, we report the modeled slopes and intercepts as

length constants (λ) and scaling terms (maximum coherence), respectively. Separate fits were made for each narrowband frequency and behavioral state (wake and NREM). Because the parameters of the exponential trend appeared to change at distances greater that 100 mm, especially for higher frequencies, separate models were fit to electrode pairs 0-100 mm distant, >100 mm, as well as to all pairs. Despite having twice as many parameters, the two-domain model was favored over the one-domain model by both Bayesian and Akaike information criteria for all frequencies and behavioral states. The parameter estimates of the models are reported in Tables 4.1 and 4.2 and shown in Figure 4.4. All mixed effects linear models were fitted with matlab's fitlme.

MEG and inverse modeling

In order to demonstrate the effects of covariability fall-off assumptions on the source localization of non-invasive recordings, a brief proof-of-concept MEG study was conducted. After provided written informed consent, one healthy 23-year-old female participant was scanned with an Elekta Neuromag 306 device while sleeping for several hours. The participant's head position within the dewar was recorded with transmitting coils fixed to the scalp. Subsequently, high-resolution T1-weighted structural MR images were obtained. As with the SEEG patients, her cortical surfaces were reconstructed from the MR volume with the FreeSurfer recon-all pipeline (Fischl, 2012) and Spherical surface registration (Fischl et al., 1999) was used to map the individual subjects' bipolar channel vertices to 32k_FS_LR grayordinate (Marcus et al., 2013) atlas as well as to parcels of the HCP-MMP parcellation scheme (Glasser et al., 2016). The participant's MR and MEG head position were manually registered using digitized fiducial points. Only the 204 planar gradiometers were examined, and 8 channels were manually excluded for being noisy or flat. Telemetry was acquired at 1000 Hz, resampled to 200 Hz and bandpass filtered between 0.5 and 15 Hz. A typical K-complex followed by a spindle during an artifact free period was manually selected and this source localization performed at the peak of this single trial K-complex.

The forward operator relating the gradient predicted in the sensors from all unit cortical dipolar sources was estimated using a 1-shell boundary element method with openmeeg (Gramfort et al., 2010; Kybic et al., 2005). Sources were placed at 59,412 32k_FS_LR grayordinate vertices, excluding those on the non-cortical medial wall. Sources were orientation constrained to the surface normal of the gray-matter — white-matter interface. The inverse operator was first estimated using the classical regularized minimum norm method (Dale and Sereno, 1993; Hämäläinen and Ilmoniemi, 1994):

Eq.1 $\mathbf{W} = \frac{\boldsymbol{RG}^{\mathrm{T}}}{(\mathbf{GRG}^{\mathrm{T}}+\boldsymbol{C})}$

where W is the inverse operator, G is the forward operator, or gain matrix, R is the assumed source covariance, equivalent to a Bayesian prior probability. In the minimum-norm formulation R is an identity matrix, meaning all sources are equal variance and uncorrelated. The regularization term C is scaled diagonal matrix of sensor noise variances. We assumed white noise and an SNR = 5 and defined C = $\frac{1}{SNR^2 diag(\mathbf{GRG}^{\mathrm{T}})}$. Multiplying the inverse operator by the sensor telemetry c yields the predicted source distribution, s = $\mathbf{W}$c. We then repeated the procedure, replacing the identity R with:

Eq. 2 $\mathbf{R} = \begin{cases} e^{\frac{-1}{\lambda}\mathbf{D}} & \mathbf{D}_{(i,j)} \leq 100 \text{ mm} \\ 0 & \mathbf{D}_{(i,j)} > 100 \text{ mm} \end{cases}$

where D is the distance matrix between all sources i and j, defined as inter-parcel fiber distances (Rosen and Halgren, 2021) for λ = 1, 10, 20, 40, 60, and 100 mm. For all inverse estimates, including the minimum-norm, a Gaussian smoothing kernel with a 2 mm standard deviation, defined in inter-source Euclidean distances, was applied to the resulting source distributions, in part to compensate for the boundary effects of the inter-parcel fiber distances used in defining the assumed source covariance.

All preprocessing and analyses were performed with custom scripts executed in matlab 2020b with the exception of the openmeeg c++ package (Gramfort et al., 2010; Kybic et al., 2005). Some matlab source code from FieldTrip (Oostenveld et al., 2011) was incorporated.

Results

Coherence stabilizes in less than 20 minutes of integrated data

Within each patient, the pattern of coherence among clean, transcortical bipolar SEEG channels converges rapidly to a steady state at very similar rates in both wake and NREM sleep, requiring no more than 15.0 ± 4.1 (mean ± stdev.) integrated minutes for wake and 16.9 ± 4.7 minutes for NREM sleep at the 0.5 Hz, the lowest examined narrowband frequency. The integration time decreases nearly monotonically with frequency, to 4.6 ± 1.5 minute and 4.5 ± 1.7 minutes for wake and NREM sleep repetitively. Values for all examined frequencies are shown in tables 4.1 and 4.2. Thus, coherence is a stable characteristic of cortical LFP, for a given frequency and state.

Coherence decays rapidly with frequency and distance

As expected, inter-electrode coherence is generally higher at short distances and low frequencies and lower at long distances and high frequencies, see Figure 4.3. However, during NREM sleep The characteristic frequency bands of sleep graphoelements, including slow oscillations (0.5-2 Hz), theta bursts (5-8 Hz) (Gonzalez et al., 2018), and sleep spindles (10-16 Hz) have elevated coherence. The increase inter-channel synchrony in the latter two bands in NREM is particularly notable as the average univariate spectral power in these band is actually higher during wake (Figure 4.1), indicative of strong but relatively asynchronous theta and alpha band (8-12 Hz) power during wake.

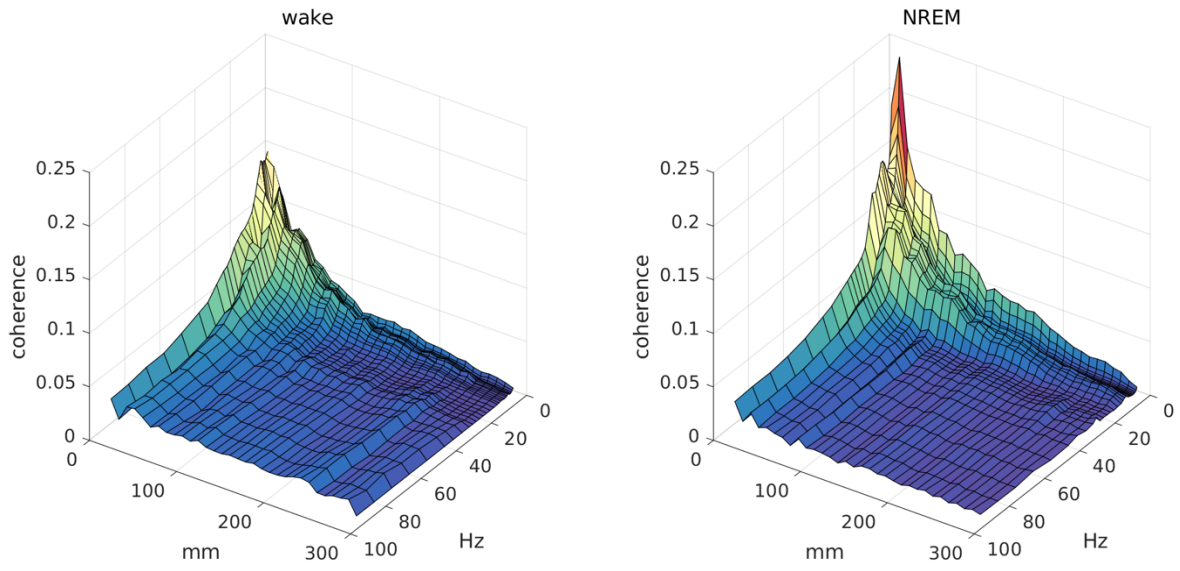

Figure 4.4 Coherence as a function of frequency and distance for wake and NREM sleep.

Coherence decays with exponential distance rules

As with anatomical connectivity (Ercsey-Ravasz et al., 2013; Rosen and Halgren, 2021), functional connectivity is reasonably well described as a decreasing exponential function of the white matter fiber length between areas. Figures 4.5 and 4.6 show exponential regression lines on 2-d histograms of observed coherence and distance. Because the parameters of the function appear to change for long-range connections greater than 100 mm distant, a piecewise regression was estimated and found to be more explanatory than the single domain model for all examined behavioral states and frequencies, with Bayesian and Akaike information criteria which penalize for overfitting. The length constant, λ, a measure of functional connectivity spread, or the (inverse) rate of fall-off with distance, varies between 64.0 and 28.9 mm for the 0-100 mm regressions depending on frequency, longer than the ~23.5 mm observed for anatomical connections (Rosen and Halgren, 2021). The parameters and variance explained by the piecewise regressions for all frequencies are listed in Tables 4.1 and 4.2 and plotted as a function of frequency for wake and NREM in Figure 4.7. Lower frequencies generally have a lower rate of falloff and higher frequencies a higher rate of falloff, though

this trend is highly non-monotonic. The amount of variance explained by the exponential rule increases with frequency, which we hypothesize may be due increase functionally modulated activity at lower frequencies which deviate from the more-strongly exponential anatomical pattern of connectivity.

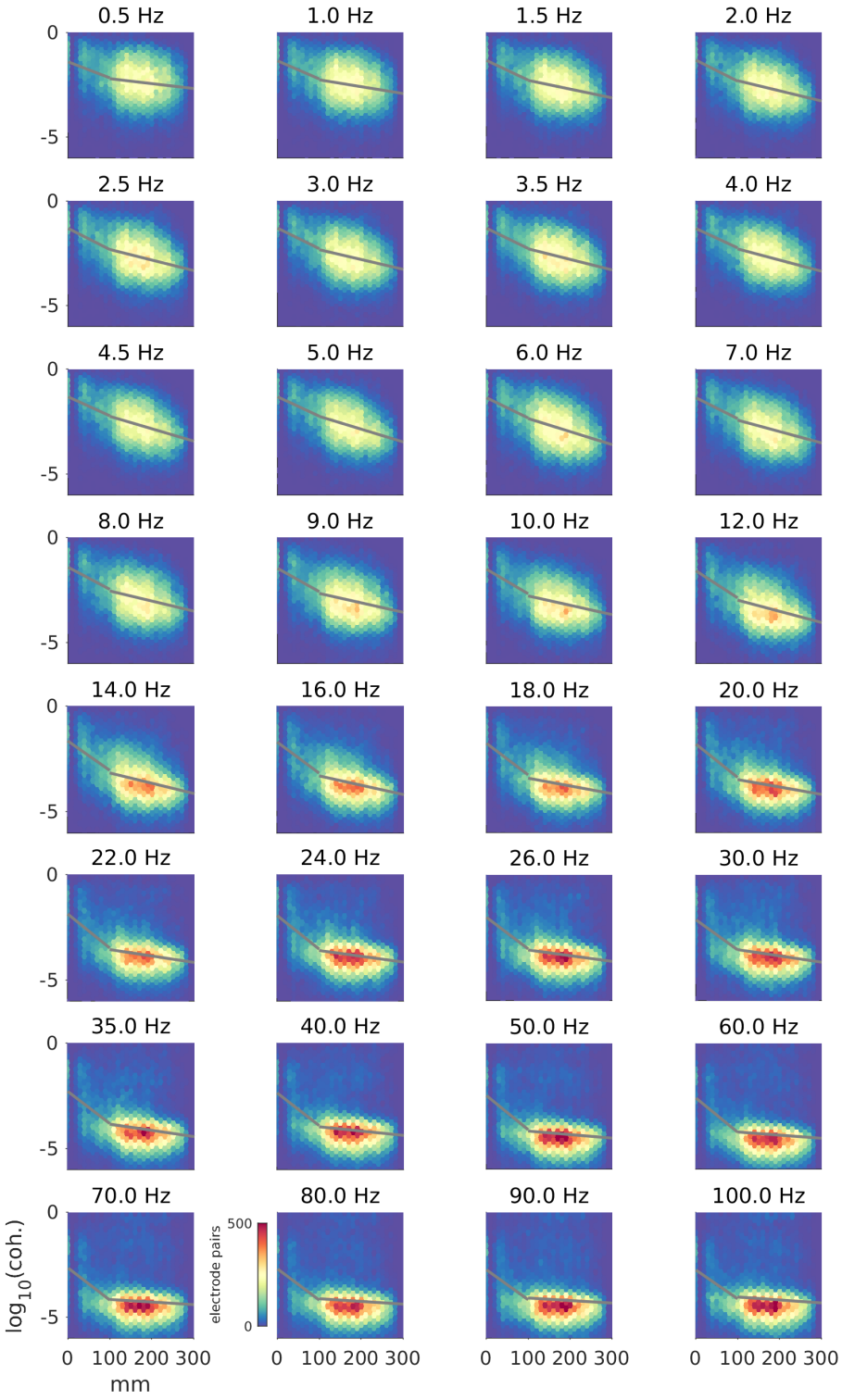

Figure 4.5 Piecewise mixed effects linear models of log(coherence) as a function of fiber distance during wake. Images show 2-d histograms of channel pairs on a plane of $\log_{10}$(coherence) and distance, where the number of channel pairs per 2-d bin is coded by color. Overlayed gray traces show model estimates of λ and scaling parameter as slope and intercept in semilog-y. Note that the regressions are quantified with natural log(coherence) then rendered in semilog$_{10}$-y.

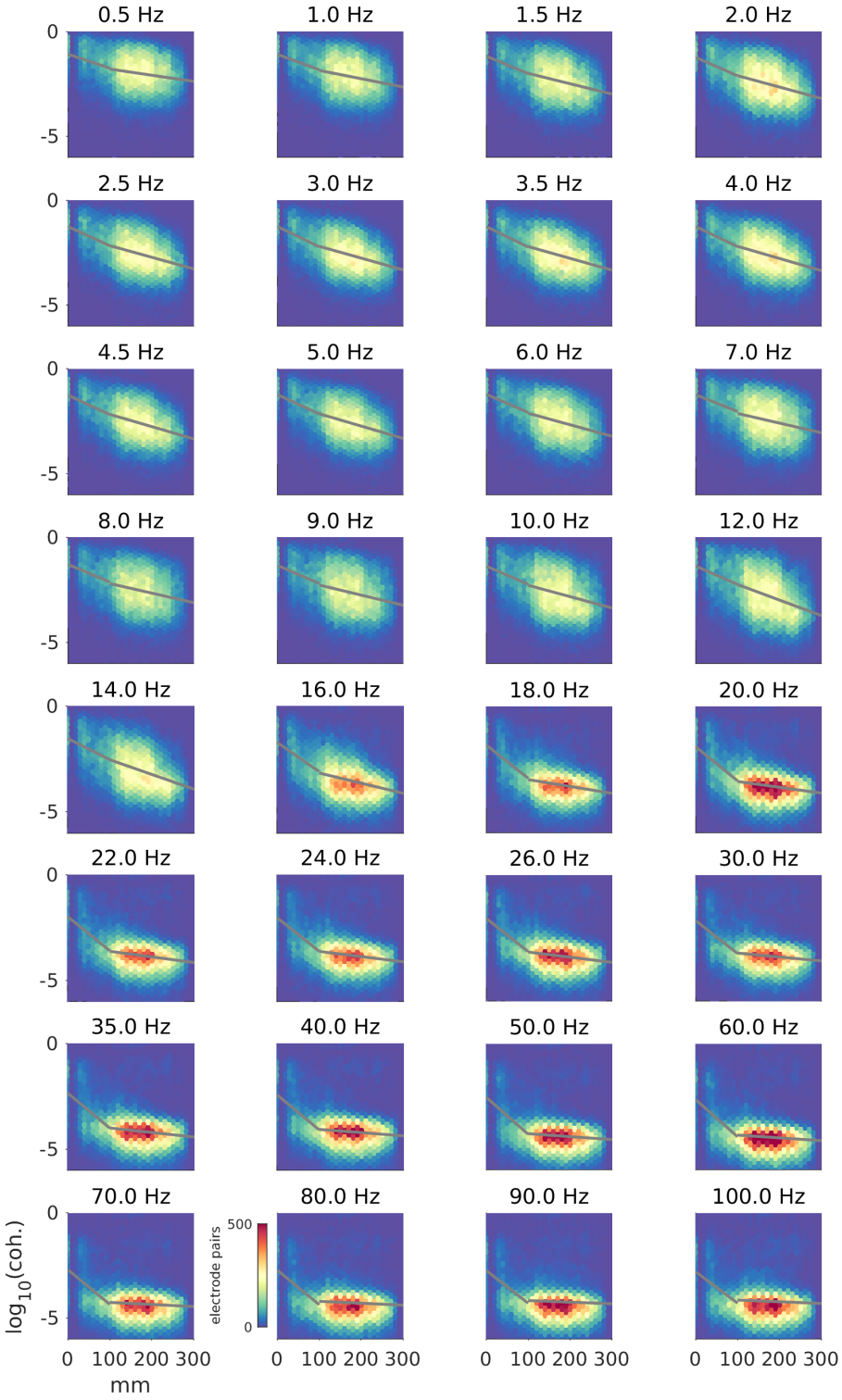

Figure 4.6 Piecewise mixed effects linear models of log(coherence) as a function of fiber distance during NREM sleep. Images show 2-d histograms of channel pairs on a plane of $\log_{10}$(coherence) and distance, where the number of channel pairs per 2-d bin is coded by color. Overlayed gray traces show model estimates of λ and scaling parameter as slope and intercept. Note that the regressions are quantified with natural log(coherence) then rendered in semi$\log_{10}$-y.

The spread of coherence is elevated in the characteristic bands of sleep graphoelements

While the length constant, λ, of the of estimated exponential decay function decreases with frequency overall, the spread of synchrony is significantly elevated above this trend at white matter fiber distances less that 100 mm in the characteristic frequency bands of slow oscillations (0.5-2 Hz), theta bursts (5-8 Hz), and sleep spindles (12-16 Hz) during NREM sleep as indicated by the non-overlapping NREM and wake 95% confidence intervals of those bands in the figure 4.5 A. The scaling parameter, or maximum coherence is also elevated, strikingly so for slow oscillation frequencies, though more marginally so for theta bursts and sleep spindle frequencies.

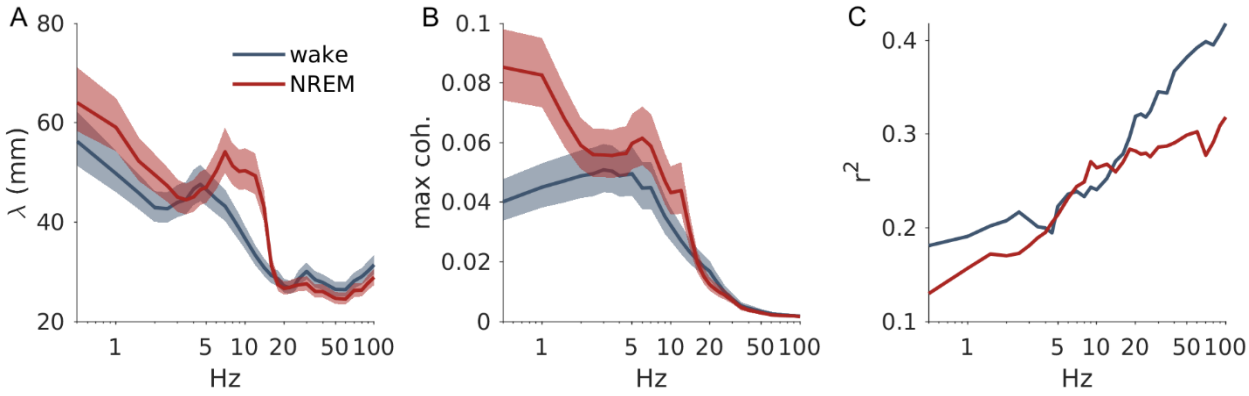

Figure. 4.7 Parameters and variance explained for 0-100 mm exponential model across frequency. (A) length constant, (B) scaling parameter, (C) variance explained. Overlays indicate 95% confidence intervals. All axes are semi-$\log_{10}$-x.

Table 4.1 Estimated coherence fall-off parameters for wake. The variance explained, average time to within-patient coherence matrix convergence and frequency decomposition parameters are also included.

frequency (Hz)	bandwidth (Hz)	mean cnvrg. dur. (m)	λ (mm) 0-100 mm	max coh. 0-100 mm	r^2 0-100 mm	λ (mm) >100 mm	max coh. >100 mm	r^2 >100 mm
0.5	0.5	14.99	56.25	4.02E-02	0.18	185.17	1.07E-02	0.16
1	0.5	13.77	49.77	4.50E-02	0.19	132.34	1.17E-02	0.17
1.5	0.5	13.47	45.88	4.72E-02	0.20	103.97	1.36E-02	0.19
2	0.5	13.23	42.93	4.88E-02	0.21	89.53	1.54E-02	0.20
2.5	0.5	13.14	42.70	4.96E-02	0.22	86.25	1.53E-02	0.22
3	0.5	13.04	44.00	5.09E-02	0.21	92.46	1.38E-02	0.22
3.5	0.5	12.87	44.56	5.05E-02	0.20	86.18	1.64E-02	0.23
4	0.5	12.87	46.71	4.88E-02	0.20	81.39	1.75E-02	0.24
4.5	0.5	12.80	47.60	4.92E-02	0.19	73.35	2.22E-02	0.24
5	0.5	12.84	46.57	4.96E-02	0.22	71.07	2.31E-02	0.27
6	1	11.27	44.62	4.48E-02	0.24	69.58	1.88E-02	0.31
7	1	10.96	43.22	4.49E-02	0.24	79.76	1.31E-02	0.31
8	1	10.72	40.87	3.96E-02	0.23	90.39	8.67E-03	0.31
9	1	10.09	38.73	3.52E-02	0.24	96.27	6.21E-03	0.31
10	1	9.64	36.72	3.22E-02	0.24	97.11	4.67E-03	0.30
12	2	7.78	33.34	2.71E-02	0.25	81.39	3.58E-03	0.34
14	2	7.49	30.91	2.33E-02	0.27	88.58	2.14E-03	0.35
16	2	7.23	29.26	2.06E-02	0.28	97.87	1.39E-03	0.36
18	2	6.99	28.59	1.84E-02	0.30	117.34	9.04E-04	0.39
20	2	6.83	27.15	1.68E-02	0.32	122.56	7.49E-04	0.43
22	2	6.64	26.82	1.41E-02	0.32	142.60	5.67E-04	0.44
24	2	6.57	27.09	1.19E-02	0.32	157.93	4.79E-04	0.44
26	2	6.53	28.61	9.89E-03	0.32	159.71	4.97E-04	0.49
30	2	6.41	30.09	7.55E-03	0.35	144.74	5.52E-04	0.50
35	5	5.13	28.38	5.27E-03	0.34	146.76	2.84E-04	0.52
40	5	4.95	27.86	4.48E-03	0.37	215.02	1.71E-04	0.54
50	10	4.45	26.47	3.36E-03	0.38	257.79	9.75E-05	0.56
60	10	4.22	26.42	2.58E-03	0.39	288.08	8.47E-05	0.59
70	10	4.37	28.17	2.28E-03	0.40	353.13	9.31E-05	0.59
80	10	4.34	29.02	2.06E-03	0.40	337.80	1.02E-04	0.59
90	10	4.55	30.19	1.88E-03	0.41	358.83	1.09E-04	0.61
100	10	4.62	31.42	1.83E-03	0.42	302.43	1.29E-04	0.60

Table 4.2 Estimated coherence fall-off parameters for NREM sleep. The variance explained, average time to within-patient coherence matrix convergence and frequency decomposition parameters are also included.

frequency (Hz)	bandwidth (Hz)	mean cnvrg. dur. (m)	λ (mm) 0-100 mm	max coh. 0-100 mm	r^2 0-100 mm	λ (mm) >100 mm	max coh. >100 mm	r^2 >100 mm
0.50	0.50	16.90	64.04	8.53E-02	0.13	147.68	3.21E-02	0.14
1.00	0.50	15.95	59.06	8.27E-02	0.16	109.54	3.52E-02	0.20
1.50	0.50	14.54	52.28	6.79E-02	0.17	87.71	3.20E-02	0.22
2.00	0.50	13.56	49.52	5.91E-02	0.17	79.97	2.77E-02	0.22
2.50	0.50	13.14	47.30	5.60E-02	0.17	78.51	2.44E-02	0.22
3.00	0.50	12.74	45.01	5.59E-02	0.18	77.35	2.31E-02	0.22
3.50	0.50	12.41	44.49	5.57E-02	0.19	77.09	2.27E-02	0.21
4.00	0.50	12.42	45.09	5.62E-02	0.19	74.74	2.42E-02	0.22
4.50	0.50	12.47	46.53	5.64E-02	0.21	74.33	2.60E-02	0.25
5.00	0.50	12.51	47.00	5.97E-02	0.21	73.87	2.80E-02	0.25
6.00	1.00	11.06	50.36	6.15E-02	0.23	79.22	2.70E-02	0.31
7.00	1.00	11.35	54.15	5.88E-02	0.24	94.22	2.16E-02	0.35
8.00	1.00	11.00	51.34	5.26E-02	0.25	95.32	1.82E-02	0.35
9.00	1.00	10.94	50.22	4.71E-02	0.27	90.13	1.65E-02	0.38
10.00	1.00	10.86	50.37	4.32E-02	0.26	80.08	1.84E-02	0.38
12.00	2.00	9.98	49.34	4.39E-02	0.27	58.55	3.15E-02	0.37
14.00	2.00	9.06	43.12	3.03E-02	0.26	62.14	1.47E-02	0.33
16.00	2.00	7.31	31.24	1.99E-02	0.27	89.99	2.10E-03	0.30
18.00	2.00	6.86	27.40	1.51E-02	0.28	132.39	7.13E-04	0.30
20.00	2.00	6.77	26.66	1.24E-02	0.28	156.57	5.15E-04	0.32
22.00	2.00	6.65	26.84	1.09E-02	0.28	163.17	4.47E-04	0.34
24.00	2.00	6.61	27.19	9.71E-03	0.28	175.62	4.23E-04	0.34
26.00	2.00	6.54	27.37	8.94E-03	0.28	176.11	3.89E-04	0.34
30.00	2.00	6.36	27.58	6.99E-03	0.29	231.12	3.04E-04	0.34
35.00	5.00	5.19	26.05	4.68E-03	0.29	203.30	1.64E-04	0.35
40.00	5.00	5.02	26.04	3.84E-03	0.29	286.26	1.22E-04	0.35
50.00	10.00	4.39	24.66	2.89E-03	0.30	307.08	7.31E-05	0.38
60.00	10.00	4.14	24.53	2.23E-03	0.30	322.32	6.21E-05	0.41
70.00	10.00	4.33	26.25	2.02E-03	0.28	442.65	6.95E-05	0.39
80.00	10.00	4.38	26.31	1.93E-03	0.29	472.23	7.74E-05	0.43
90.00	10.00	4.40	27.79	1.86E-03	0.31	567.73	8.11E-05	0.47
100.00	10.00	4.50	28.90	1.63E-03	0.32	534.67	8.66E-05	0.50

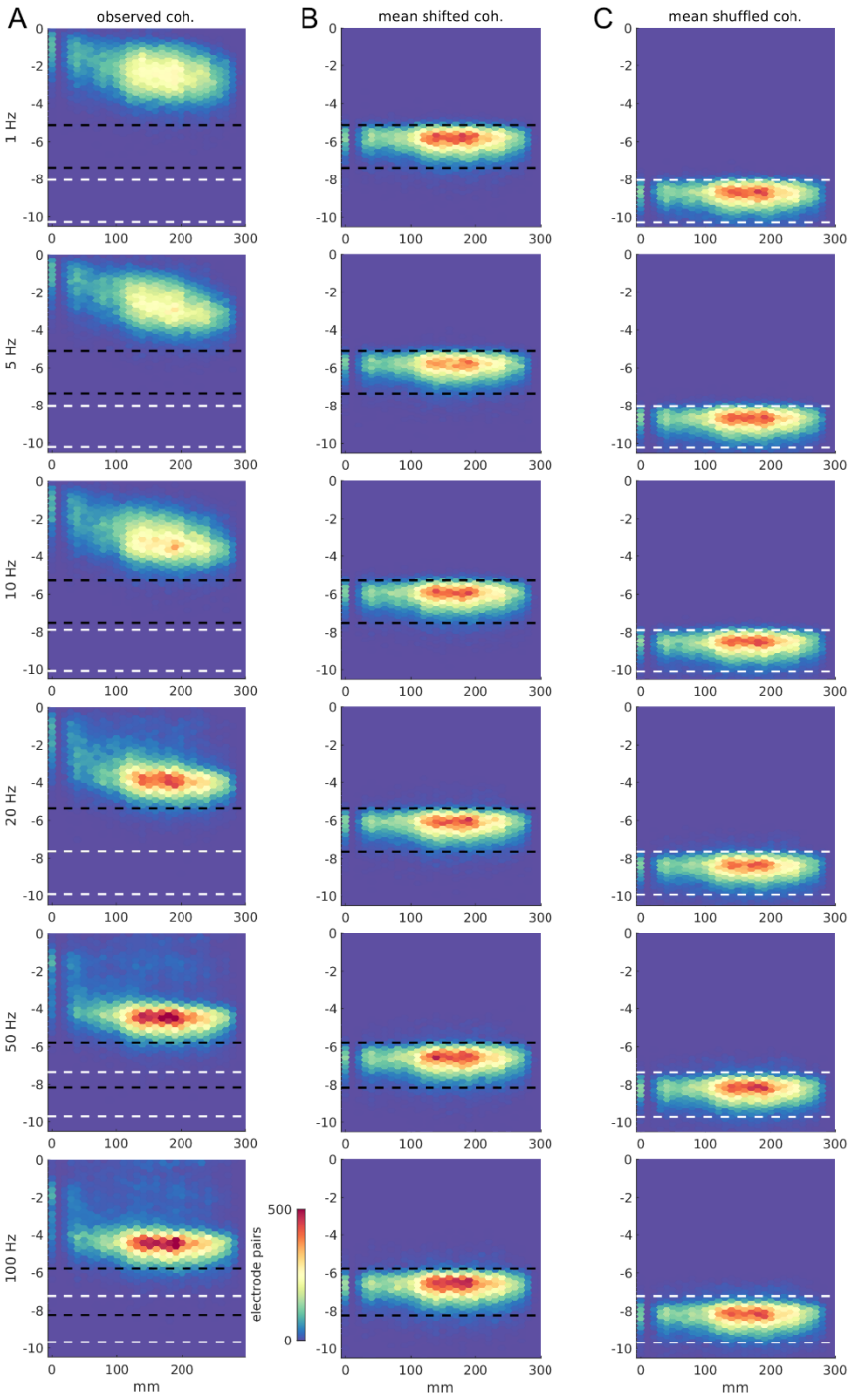

Figure 4.8 Coherence noise-floor for wake. Images show 2-d histograms of channel pairs on a plane of $\log_{10}$(coherence) and distance, where the number of channel pairs per 2-d bin is coded by color. (A) Observed coherence as a function of fiber distance. (B) Mean coherence of iterations of randomly time-lag shifted telemetry, in which the autocorrelations of the signals are preserved (C) Mean coherence of iterations of randomly time-shuffled telemetry, in which only the statistics of the time samples is preserved. The black and white dashed traces indicate the empirical 95% confidence intervals of coherence in (B) and (C), respectively.

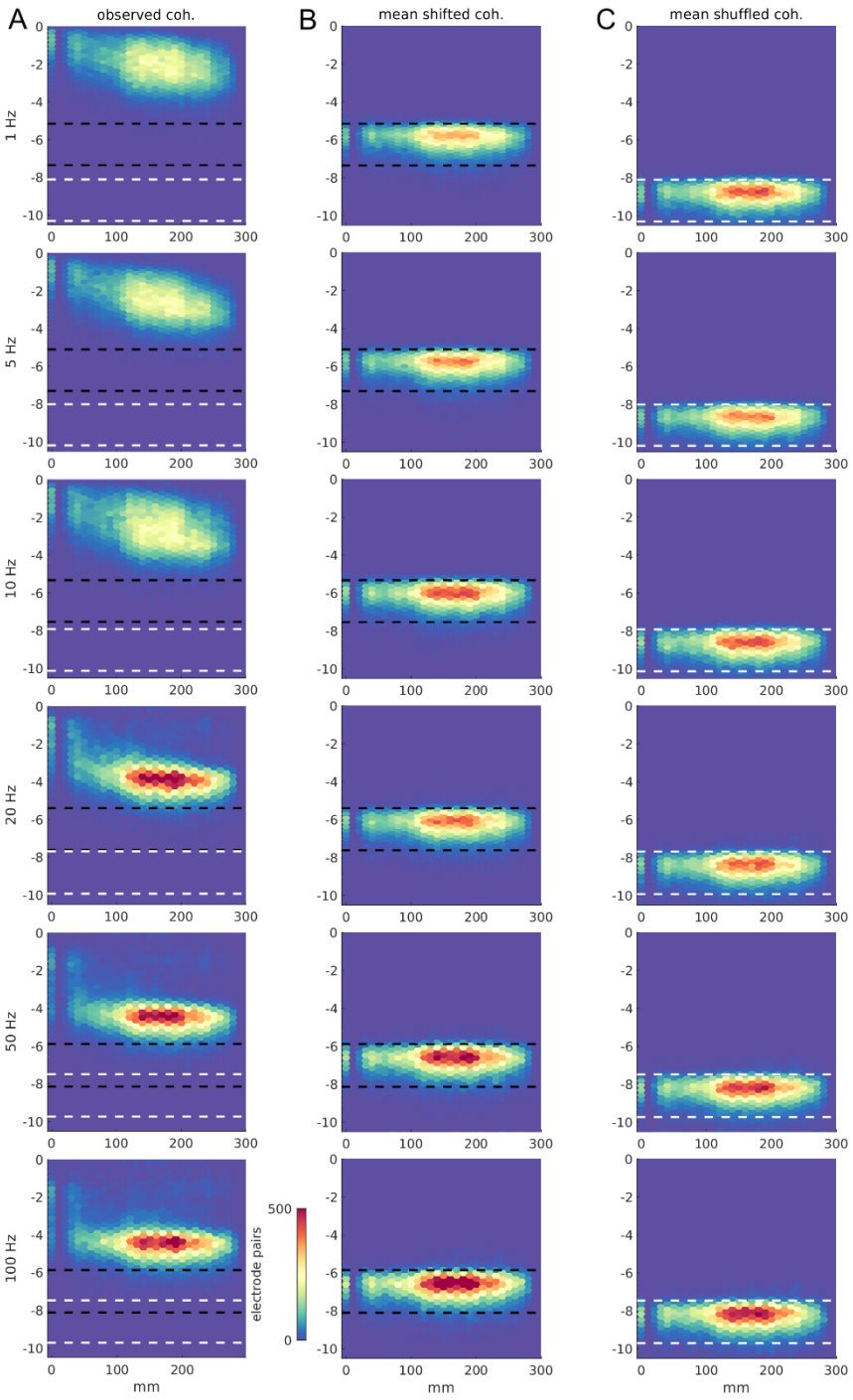

Figure 4.9 Coherence noise-floor for NREM sleep. Images show 2-d histograms of channel pairs on a plane of $\log_{10}$(coherence) and distance, where the number of channel pairs per 2-d bin is coded by color. (A) Observed coherence as a function of fiber distance. (B) Mean coherence of iterations of randomly time-lag shifted telemetry, in which the autocorrelations of the signals are preserved (C) Mean coherence of iterations of randomly time-shuffled telemetry, in which only the statistics of the time samples is preserved. The black and white dashed traces indicate the empirical 95% confidence intervals of coherence in (B) and (C), respectively.

There is a floor of minimum synchrony greater than would be expected by chance

At higher frequencies and longer distances, inter-channel coherence is low and less distance dependent, as is evident by regression lines for distances > 100 mm that approach the horizontal (i.e., low maximum coherences and very high estimated λ's) in Figures 4.5 and 4.6. This pattern begins to become evident at 12 Hz in waking and 16 Hz in NREM sleep and is the dominant pattern for both states at frequencies greater than 20 Hz at fiber distances greater than ~100 mm. To test the validity of this low relatively distance invariant synchrony, we estimated the coherence expected by chance using two Monte Carlo procedures, the first of which abolished inter-channel correlations but preserved within channel autocorrelation by independently shifting each channel at random before estimating coherence , and a second that abolished both but preserved the statistics of the individual telemetry samples by shuffling the time sample of each channel independently. 2-d Histograms of these controls are shown in Figures 4.8 B,C and 4.9 B,C for wake and NREM sleep, respectively. In all frequencies and neurobehavioral states examined, the floor of observed coherence values is much greater than the upper 95% confidence interval of the shuffled control, indicating that it is significantly above chance. Furthermore, the observed coherence in almost all cases exceeds the upper 95% confidence interval of the shifted control, indicating that this synchrony is due to truly communicative correlativity, rather than a byproduct of independent neural generators with similar autocorrelative properties. The confidence intervals of the shifted and shuffled controls are shown superimposed on the 2-d histogram of observed data in Figures 4.8 A and 4.9 A for wake and NREM sleep, respectively.

The rate of SEEG-derived functional connectively decays differently than other connectivity modalities

*For comparison, w*e estimated analogous falloff rates for corticocortical evoked potentials (CCEPs), probabilistic diffusion fMRI tractography , and resting-state functional MRI (re-fMRI) for connections with fiber distances ≤ 100 mm using results from our prior report (Rosen and Halgren, 2021), which sourced data from publicly available datasets (David et al., 2013; Trebaul et al., 2018; Van

Essen et al., 2013). The same dMRI-based fiber distances were used for all connectivity modalities. Fixed effects linear models of the log-transformed connectivity data were estimated and 2-d histograms and regression lines are shown in Figure 4.10. CCEPs and dMRI connectivity clearly show an exponential distance rule, and were found to have λ = 84.28 [78.74 90.66] mm, mean [95% ci], r^2 = 0.18, and λ = 19.63 [19.33 19.94] mm, r^2 = 0.77, respectively. An exponential poorly described relationship between rs-fMRI and distances (r^2 = 0.06) as synchrony is far more distributed. The CCEP falloff rate (λ = 84.28) was significantly lower than lowest observed composite SEEG rate, λ = 64.04 [58.24 71.13] mm for 0.5 Hz NREM and the dMRI falloff (λ = 19.63) was significantly higher than the highest lowest observed composite SEEG rate, λ = 24.53 [23.36 25.84] mm for 60 Hz NREM. The intercept terms, or maximum connectivity cannot be directly compared between modalities due to the disparate units of these estimated parameters.

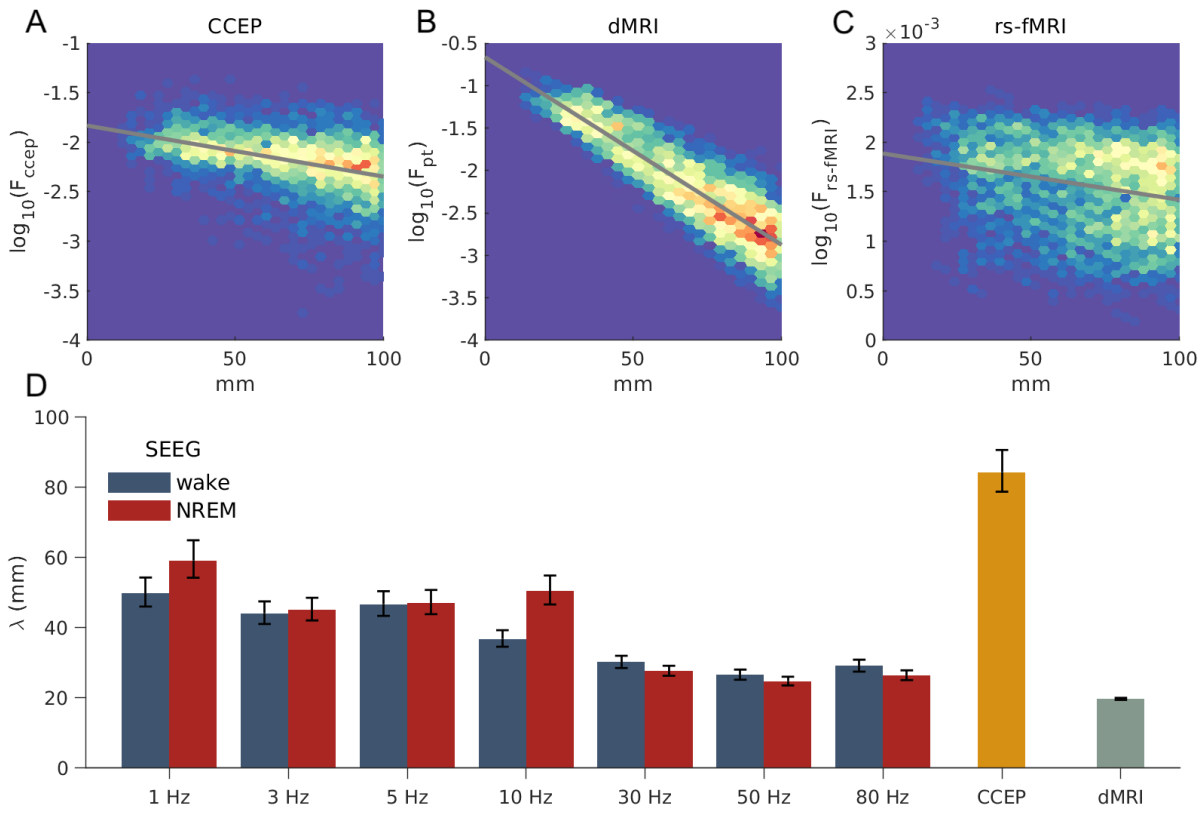

Figure 4.10 Connectivity falloff across modalities. Linear regressions of log(connectivity) as a function of fiber distance for distances ≤ 100 mm for (A) CCEP (B) dMRI (C) rs-fMRI. Images show 2-d histograms of channel pairs on a plane of $\log_{10}$(connectivity) and distance, where the number of channel pairs per 2-d bin is coded by color. Overlayed gray traces show model estimates of λ and scaling parameter as slope and intercept. Note that the regressions are quantified with natural log(connectivity) then rendered in semilog$_{10}$-y. (D) λ estimates for a subset of SEEG frequencies, CCEP, and dMRI. Error bars show 95% confidence intervals.

Falloff assumptions can affect the source localization of extracranial recordings

In a brief proof-of-concept experiment MEG was recorded from one healthy participant while they slept. Figure 4.11A shows the gradiometer topography at the peak of slow oscillation. Figures 4.11B-H all show source localization estimates of this single sensor topography, each using different assumptions about the rate of covariance fall-off among the dipolar cortical generators. Figure 4.11B shows the classical minimum-norm estimate (Dale and Sereno, 1993; Hämäläinen and Ilmoniemi, 1994) which assumes zero covariance among sources. In panels C-H, the inverse estimate was calculated using an identical mathematical framework, except that an exponential falloff of covariance

with fiber tract distance for distances below 100 mm and zero otherwise was assumed. Each panel assumes a different length constant. The spatial distribution and amplitudes of the estimated source distribution are materially affected by the different assumptions. For slow oscillation band activity, our composite SEEG results suggest that panel 4.11G with λ = 60 is the most accurate source reconstruction. While the scaling parameter estimated from coherence cannot be directly used in the minimum-norm formulation due to being unitless, future studies may use a composite unnormalized cross-spectral matrix directly (Frei et al., 2001).

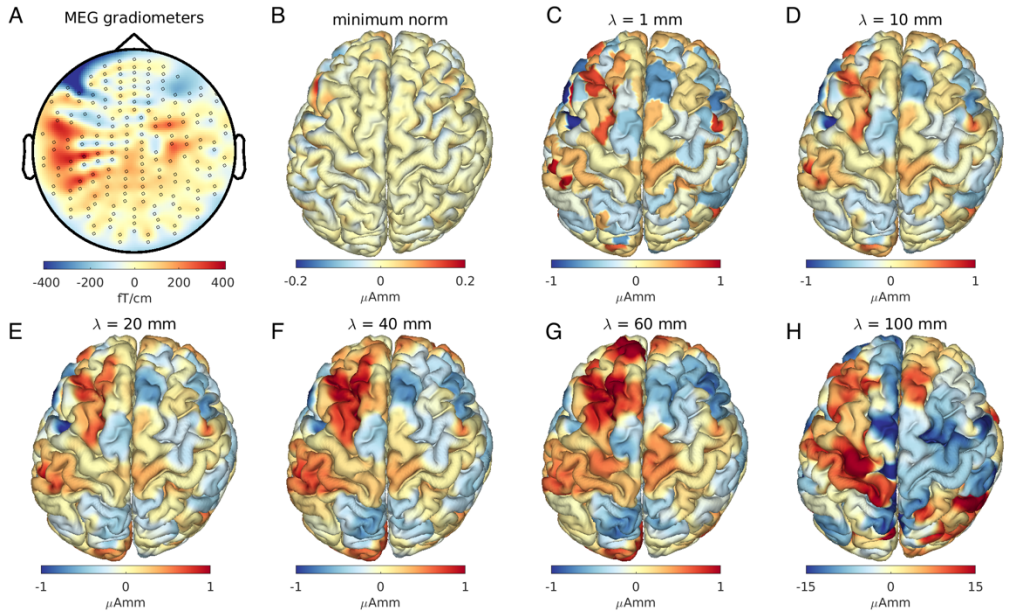

Figure 4.11 Effects of assumed source correlational fall off on MEG source localization. (A) Sensor Topography of MEG gradiometers during the peak of a k-complex during NREM sleep. (B) The minimum-norm inverse estimate of the corresponding dipolar source distribution which assumes no source correlativity. (D-H) inverse estimate of the corresponding dipolar source distribution assuming exponential falloff of source covariance at distance < 100 mm with length constants λ = 1, 10, 20, 40, 60, and 100 mm.

Discussion

In this composite SEEG study, data was pooled from hundreds of patients and thousands of focal transcortically referenced channels with the goal of getting a better view of how spontaneous corticocortical correlativity varies of with distance and frequency. We show that

functional connectivity, like structural connectivity hews to exponential distance rules and that the rate of falloff is dependent on frequency and neurobehavioral state. Higher frequencies generally have a greater rate of falloff, but during NREM sleep the frequencies characteristic of sleep graphoelements have an elevated spatial spread of synchrony in excess of this trend. A low but greater than expected by chance degree of synchrony was observed even at high frequency and long distances., and lastly the effects of assumed rates of falloff on the source localization of extracranial signals was demonstrated in an MEG case study.

One of the key limitations of SEEG recordings is that the spatial sampling in any single patient is quite sparse. While we have partially addressed this limitation by compositing data from over 200 patients and several clinical sites, the problem is amplified when investigating the bivariate relationships of channel pairs, as we have done here. Unfortunately, the sampling space of bivariate correlations scales with the square of the number of examined areas. Thus, while our dataset has at least one channel in 348/360 or 97% of HCP-MMP (Glasser et al., 2016) parcels, only 37,123/64,980 or 23% total possible parcel pairs (including pairs in the same parcel) are sampled at least once. If only pairs with at least 20 observations are considered, the bivariate coverage drops to 5% of possible parcel pairs. This issue is not unique to our study. For example, the Functional Brain Tractography project (F-TRACT) (David et al., 2013; Trebaul et al., 2018) dataset of cortico-cortico evoked potentials also examines intracranial EEG channel pair relationships maps onto the HCP-MMP parcellation atlas. The v1903 release, which has 315 patients has at least one observation in 17% of parcel pairs, dropping to 10% for 20 observations. Because so few parcel pairs are sampled with enough repetitions to enable sufficient statistical power, we do not make claims about the correlational strength of any particular pair of areas and have instead opted to report distance-coherence relationships which are well sampled.

Phamaco-resistant epilepsy patients are an imperfect model of healthy, normative brain function as they clearly exhibit significant neuropathology. However, the use of these data are justified for several reasons. First, patients selected for surgical monitoring must be diagnosed

with focal seizures rather than generalized epilepsy, which indicates that the pathological activity affects a limited extent of the overall cortex. Furthermore, considerable efforts were made to ensure that only non-epileptogenic recordings were considered in the final analysis, with multi-stage quality control resulting in only the least pathological 79% of patients, 47% of the continuously recorded duration, and 12% of possible bipolar channels being examined in the final analysis. In addition, only intracranial recordings can simultaneously provide the necessary focality and temporal resolution that our analysis requires. Lastly, the cortex, more than most other structures, has unique properties in humans, including greatly enhanced size and gyrification (Hofman, 2014), which limit the quantitative applicability of analogous investigations of in other model organisms, especially with regard to distance-based relationships.

Defining the relevant distance between electrode pairs is not straightforward. While Euclidean distances are trivial to calculate and universally defined, they clearly underestimate axonal trajectories, especially when they cut across sulci, and become increasingly inaccurate between more distant areas. Geodesic distances across the cortical ribbon suffer from the opposite problem, circumnavigating gyri rather than more plausibly traveling across the white matter between a pair of sulcal walls. Geodesic distances are also difficult to define for interhemispheric electrode pairs, as the two hemispheres form distinct surfaces. The optimal distance would be the length of a high-resolution trace, of white matter projections connecting the two locations, either with histology or diffusion MRI (dMRI), as this is most relevant to neural communication. These trajectories could be reconstructed in the implanted individuals or more likely in an alternative sample registered to a standard surface template (Fischl et al., 1999; Glasser et al., 2013). Unfortunately, despite being proposed (Van Essen et al., 2013), such high-resolution cortical connectomes have to our knowledge not yet been reported. This is likely due the substantial technical challenges involved, including the availability of human tissue in the case of histology and the computational burden, limited resolution, and gyral bias (Van Essen et al., 2014) of diffusion MRI. We have elected to use the lower resolution inter-parcel length of

dMRI tractography trajectories which we have previously reported (Rosen and Halgren, 2022, 2021). This compromise approach is in keeping with that applied in earlier dMRI (Donahue et al., 2016; van den Heuvel et al., 2015) and histological (Bakker et al., 2012; Ercsey-Ravasz et al., 2013; N. T. Markov et al., 2013) studies in non-human primates. However, inter-parcel white matter distances are inaccurate for short distances, particularly for those between electrodes in the same parcels which are considered to be at 0 mm, though these form <2% of our dataset. While this distortion is partially ameliorated by using a dense parcellation atlas like the HCP-MMP scheme (Glasser et al., 2016), future studies may estimate high-resolution white matter trajectories or alternatively employ a hybrid scheme of differently defined inter-electrode distances within nearby and distant domains.

The exponential trends for functional connectivity we observe are consistent with similar exponential rules for anatomical connectivity as determined by histological tracing (Ercsey-Ravasz et al., 2013; Nikola T. Markov et al., 2013) and diffusion MRI (Donahue et al., 2016; Rosen and Halgren, 2021). Quantitatively, it is notable that the highest falloff rate (or lowest length constant λ) is higher than that for dMRI based structural connectivity (Rosen and Halgren, 2021). The λ estimates are directly comparable as distances were defined identically in both studies. We hypothesize that the spatial decay rate of direct white matter connections may serve as a lower bound for falloff of functional connectivity. If so, correlativity in excess of direct anatomical connectivity is enabled by the nearly infinite configurations of indirect connectivity among neural elements, including active modulation, especially for cortical graphoelements. Interestingly, the rate of corticocortical evoked potential connectivity falloff is less than observed for composite coherences, suggesting that stimulation pulse traverse a broader network of indirect pathways than spontaneous endogenous activity.

The related measures of covariance, cross-spectrum, and coherence are robust, but do assume a stationary underlying process, i.e., that its statistics of do not change over time. Clearly, neural activity cannot be truly stationary in a living organism, and there is increasing evidence

that spectrally prominent components of EEG such as alpha and sleep spindles may be, in part, a reflection of traveling waves, e.g., (Halgren et al., 2019; Muller et al., 2016; Zhang et al., 2018). That said, the rapid within-patient convergence to a stable coherence pattern as more recoded time is integrated is evidence of a significant stationary component to communication between neural elements. In our accumulative data sampling procedure relatively rare segments with an outlying coherence pattern were rejected from consideration. These may be due to technical artifacts, but could also be the result of strong transient modulation of synchrony among cortical areas. Transient modulation of synchrony during neurobehavioral events is expected and commonly observed. It is important to recognize that the observations and claims we report here are limited to the underlying sustained patterns of correlation that these transients disrupt or augment. Lastly, future studies may elect to use newer measures of synchrony that do not assume stationarity such as dynamical differential covariance (Chen et al., 2022), though relating and applying these novel measures to more conventional results in the bulk of the literature can be challenging.

In addition to a basic scientific interest in how neural correlativity falls off with distance within the human cortex, there are tangible biomedical applications to the length constant, λ, estimates we have reported. Extracranial MEG and EEG are common techniques used to examine neural activity in clinical and research contexts. Their investigative power is greatly amplified by using source localization techniques to estimate the distribution of cortical generators which produced the observed M/EEG sensor activity. All source localization techniques make assumptions about the underlying cortical activity in order to derive their estimates. For a family of linear techniques that use maximum a posteriori estimation, including minimum-norm (Dale and Sereno, 1993; Hämäläinen and Ilmoniemi, 1994), dSPM (Dale et al., 2000), LORETA (Pascual-Marqui et al., 1994), and Multiple Sparse Priors (Friston et al., 2008), a key assumption is the degree of correlativity among cortical sources, as expressed in the off-diagonals of the prior probability matrix representing the assumed covariance or cross-spectrum

(Frei et al., 2001)of the cortical sources. As we demonstrated, when combined with a distance matrix of sources, the length constants can be used to intuitively populate the assumed prior covariability matrix. Furthermore, different falloff assumptions yield very different source distribution estimates for the same sensor topography. One advantage of applying a rate of falloff as opposed to pair-wise correlativity directly is that it avoids overfitting. Applying estimated falloff rates for random samples of spontaneous data to the localization of event-related data may also be advantageous in this regard. However, there are two disadvantages of this approach. First, the estimate scaling parameter, or maximum coherence, cannot be used directly, as it is a unitless scalar, and the elements of the prior matrix have units of dipole moment squared, e.g., μA^2mm^2. Second, complex cross-spectral prior matrices (Frei et al., 2001), may contain phase information, but this cannot be inferred from the decay estimates. Future studies may use the pairwise cross-spectral estimates directly to populate the prior matrix which would address both limitations, encoding phase and absolute amplitude into the prior matrix. However, populating the entire prior matrix with this approach would require that all combinations of pairwise locations be sampled with electrodes, which, as noted above, is a significant methodological hurdle. Using dense surface electrode arrays would partially alleviate the issue of coverage, but the amplitude and focality of these signal is often hampered by an ambiguous reference (Arnulfo et al., 2015; Mak-McCully et al., 2014; Nunez and Srinivasan, 2009). Alternatively, the cross-spectra of unobserved pairs may be interpolated using other available data, analogously to (Chen et al., 2020).

In sum, we have here employed a composite SSEG approach to describe a previously poorly examined fundamental aspect of human functional connectivity: the rate of correlative decay between cortical generators as a function of the white matter fiber distance between them, during spontaneous waking and NREM sleep. By analogy, these patterns can be considered to be the rules that describe the steady state cosmic background radiation of cortical correlativity from which all transient behavioral or cognitive modulations must deviate.

Future developments in the source localization of extracranial recorded will be well served by incorporating the knowledge of these patterns into their assumptions.

Acknowledgements

This work was supported by National Institute of Mental Health grant RF1MH117155. We thank Xi Jiang, Jane Q. Deng, Hannah Kim, Adam Niese, Emilia Toth, Dan Soper, Jacqueline Boccanfuso, and Hao Tan for their contributions. Data were provided, in part, by the Human Connectome Project, WU-Minn Consortium (Principal Investigators: David Van Essen and Kamil Ugurbil; 1U54MH091657) funded by the 16 National Institutes of Health (NIH) Institutes and Centers that support the NIH Blueprint for Neuroscience Research; and by the McDonnell Center for Systems Neuroscience at Washington University. Data were provided, in part, by the Functional Brain Tractography Project, funded by the European Research council.

Chapter 4, in part, is currently being prepared for submission for publication of the material coauthored with Sophie Kajfez, Jacob Garret, Charles Dickey, Caleb Nerison, Brittany Stedelin, Ahmed Raslan, Sydney Cash, Kathryn Davis, Sandip Pati, Jorge Gonzalez-Martinez, Sharona Ben-Haim, Jerry Shih, and Eric Halgren. The dissertation author was the primary author of this chapter.

References

Arnulfo G, Hirvonen J, Nobili L, Palva S, Palva JM. 2015. Phase and amplitude correlations in resting-state activity in human stereotactical EEG recordings. Neuroimage 112:114–127.

Bakker R, Wachtler T, Diesmann M. 2012. CoCoMac 2.0 and the future of tract-tracing databases. Front Neuroinform 6:30.

Campagnola L, Seeman SC, Chartrand T, Kim L, Hoggarth A, Gamlin C, Ito S, Trinh J, Davoudian P, Radaelli C, Kim M-H, Hage T, Braun T, Alfiler L, Andrade J, Bohn P, Dalley R, Henry A, Kebede S, Alice M, Sandman D, Williams G, Larsen R, Teeter C, Daigle TL, Berry K, Dotson N, Enstrom R, Gorham M, Hupp M, Dingman Lee S, Ngo K, Nicovich PR, Potekhina L, Ransford S, Gary A, Goldy J, McMillen D, Pham T, Tieu M, Siverts L, Walker M, Farrell C, Schroedter M, Slaughterbeck C, Cobb C, Ellenbogen R, Gwinn RP, Keene CD, Ko AL, Ojemann JG, Silbergeld DL, Carey D, Casper T, Crichton K, Clark M, Dee N, Ellingwood L, Gloe J, Kroll M, Sulc J, Tung H, Wadhwani K, Brouner K, Egdorf T, Maxwell M, McGraw M, Pom CA, Ruiz A, Bomben J, Feng D, Hejazinia N, Shi S, Szafer A, Wakeman W, Phillips J, Bernard A, Esposito L, D'Orazi FD, Sunkin S, Smith K, Tasic B, Arkhipov A, Sorensen S, Lein E, Koch C, Murphy G, Zeng H, Jarsky T. 2022. Local connectivity and synaptic dynamics in mouse and human neocortex. Science 375.

Chen Y, Rosen BQ, Sejnowski TJ. 2022. Dynamical differential covariance recovers directional network structure in multiscale neural systems. Proc Natl Acad Sci 119:e2117234119.

Chen Y, Zhang Z-K, He Y, Zhou C. 2020. A Large-Scale High-Density Weighted Structural Connectome of the Macaque Brain Acquired by Predicting Missing Links. Cereb Cortex 30:4771–4789.

Dale AM, Liu AK, Fischl BR, Buckner RL, Belliveau JW, Lewine JD, Halgren E. 2000. Dynamic Statistical Parametric Mapping. Neuron 26:55–67.

Dale AM, Sereno MI. 1993. Improved Localization of Cortical Activity by Combining EEG and MEG with MRI Cortical Surface Reconstruction: A Linear Approach. J Cogn Neurosci.

David O, Job AS, De Palma L, Hoffmann D, Minotti L, Kahane P. 2013. Probabilistic functional tractography of the human cortex. Neuroimage 80:307–317.

Dickey CW, Verzhbinsky IA, Jiang X, Rosen BQ, Kajfez S, Eskandar EN, Gonzalez-Martinez J, Cash SS, Halgren E. 2022. Cortical Ripples during NREM Sleep and Waking in Humans. J Neurosci 42:7931 LP – 7946.

Donahue CJ, Sotiropoulos SN, Jbabdi S, Hernandez-Fernandez M, Behrens TE, Dyrby TB, Coalson T, Kennedy H, Knoblauch K, Van Essen DC, Glasser MF. 2016. Using Diffusion Tractography to Predict Cortical Connection Strength and Distance: A Quantitative Comparison with Tracers in the Monkey. J Neurosci 36:6758–6770.

Ercsey-Ravasz M, Markov NT, Lamy C, VanEssen DC, Knoblauch K, Toroczkai Z, Kennedy H. 2013. A Predictive Network Model of Cerebral Cortical Connectivity Based on a Distance Rule. Neuron 80:184–197.

Fedorov A, Beichel R, Kalpathy-Cramer J, Finet J, Fillion-Robin JC, Pujol S, Bauer C, Jennings D, Fennessy F, Sonka M, Buatti J, Aylward S, Miller J V., Pieper S, Kikinis R. 2012. 3D Slicer as an image computing platform for the Quantitative Imaging Network. Magn Reson Imaging 30:1323–1341.

Fischl B. 2012. FreeSurfer. Neuroimage 62:774–781.

Fischl B, Sereno MI, Tootell RBH, Dale AM. 1999. High-resolution intersubject averaging and a coordinate system for the cortical surface. Hum Brain Mapp 8:272–284.

Frauscher B, von Ellenrieder N, Zelmann R, Doležalová I, Minotti L, Olivier A, Hall J, Hoffmann D, Nguyen DK, Kahane P. 2018. Atlas of the normal intracranial electroencephalogram: neurophysiological awake activity in different cortical areas. Brain 141:1130–1144.

Frei E, Gamma A, Pascual R. 2001. Localization of MDMA -Induced brain activity in healthy volunteers using low resolution brain electromagnetic tomography. Hum Brain Mapp 14:152–162.

Friston K. 2012. The history of the future of the Bayesian brain. Neuroimage 62:1230–1233.

Friston K, Harrison L, Daunizeau J, Kiebel S, Phillips C, Trujillo-Barreto N, Henson R, Flandin G, Mattout J. 2008. Multiple sparse priors for the M/EEG inverse problem. Neuroimage 39:1104–1120.

Glasser MF, Coalson TS, Robinson EC, Hacker CD, Harwell J, Yacoub E, Ugurbil K, Andersson J, Beckmann CF, Jenkinson M, Smith SM, Van Essen DC. 2016. A multi-modal parcellation of human cerebral cortex. Nature 536:171–8.

Glasser MF, Sotiropoulos SN, Wilson JA, Coalson TS, Fischl B, Andersson JL, Xu J, Jbabdi S, Webster M, Polimeni JR. 2013. The minimal preprocessing pipelines for the Human Connectome Project. Neuroimage 80:105–124.

Gonzalez CE, Jiang X, Gonzalez-Martinez J, Halgren E. 2022. Human Spindle Variability. J Neurosci 42:4517 LP – 4537.

Gonzalez CE, Mak-McCully RA, Rosen BQ, Cash SS, Chauvel PY, Bastuji H, Rey M, Halgren E. 2018. Theta bursts precede, and spindles follow, cortical and thalamic downstates in human NREM sleep. J Neurosci 38:9989–10001.
Gramfort A, Papadopoulo T, Olivi E, Clerc M. 2010. OpenMEEG: opensource software for quasistatic bioelectromagnetics. Biomed Eng Online 9:45.

Halgren M, Ulbert I, Bastuji H, Fabó D, Erőss L, Rey M, Devinsky O, Doyle WK, Mak-McCully R, Halgren E, Wittner L, Chauvel P, Heit G, Eskandar E, Mandell A, Cash SS. 2019. The generation and propagation of the human alpha rhythm. Proc Natl Acad Sci 116:23772–23782.

Hämäläinen MS, Ilmoniemi RJ. 1994. Interpreting magnetic fields of the brain: minimum norm estimates. Med Biol Eng Comput 32:35–42.

Herdin M, Czink N, Ozcelik H, Bonek E. 2005. Correlation matrix distance, a meaningful measure for evaluation of non-stationary MIMO channels. Veh Technol Conf 2005 VTC 2005-Spring 2005 IEEE 61st 1:136-140 Vol. 1.

Hofman MA. 2014. Evolution of the human brain: when bigger is better. Front Neuroanat 8:15.

Honey CJ, Sporns O, Cammoun L, Gigandet X, Thiran JP, Meuli R, Hagmann P. 2009. Predicting human resting-state functional connectivity from structural connectivity. Proc Natl Acad Sci U S A 106:2035–2040.

Iber C, Ancoli-Israel S, Chesson A, Quan S. 2007. The AASM Manual for the Scoring of Sleep and Associates Events: Rules, Terminology and Technical Specifications, Sleep (Rochester).
Johnson H, Harris G, Williams K. 2007. BRAINSFit: mutual information rigid registrations of whole-brain 3D images, using the insight toolkit. Insight J.

Kybic J, Clerc M, Abboud T, Faugeras O, Keriven R, Papadopoulo T. 2005. A common formalism for the integral formulations of the forward EEG problem. IEEE Trans Med Imaging 24:12–28.

López JD, Litvak V, Espinosa JJ, Friston KJ, Barnes GR. 2014. Algorithmic procedures for Bayesian MEG/EEG source reconstruction in SPM. Neuroimage 84:476–487.

Mak-McCully RA, Deiss SR, Rosen BQ, Jung KY, Sejnowski TJ, Bastuji H, Rey M, Cash SS, Bazhenov M, Halgren E. 2014. Synchronization of Isolated Downstates (K-Complexes) May Be Caused by Cortically-Induced Disruption of Thalamic Spindling. PLoS Comput Biol 10.

Mak-Mccully RA, Rolland M, Sargsyan A, Gonzalez C, Magnin M, Chauvel P, Rey M, Bastuji H, Halgren E. 2017. Coordination of cortical and thalamic activity during non-REM sleep in humans. Nat Commun 8.

Marcus DS, Harms MP, Snyder AZ, Jenkinson M, Wilson JA, Glasser MF, Barch DM, Archie KA, Burgess GC, Ramaratnam M. 2013. Human Connectome Project informatics: quality control, database services, and data visualization. Neuroimage 80:202–219.

Markov Nikola T., Ercsey-Ravasz M, Van Essen DC, Knoblauch K, Toroczkai Z, Kennedy H. 2013. Cortical high-density counterstream architectures. Science.

Muller L, Piantoni G, Koller D, Cash SS, Halgren E, Sejnowski TJ. 2016. Rotating waves during human sleep spindles organize global patterns of activity that repeat precisely through the night. Elife 5:1–16.

Nolte G, Bai O, Wheaton L, Mari Z, Vorbach S, Hallett M. 2004. Identifying true brain interaction from EEG data using the imaginary part of coherency. Clin Neurophysiol 115:2292–2307.
Nunez PL, Srinivasan R. 2009. Electric Fields of the Brain: The neurophysics of EEG, Electric Fields of the Brain: The neurophysics of EEG.

Oostenveld R, Fries P, Maris E, Schoffelen J-M. 2011. FieldTrip: Open source software for advanced analysis of MEG, EEG, and invasive electrophysiological data. Comput Intell Neurosci 2011:156869.

Pascual-Marqui RD, Michel CM, Lehmann D. 1994. Low resolution electromagnetic tomography: a new method for localizing electrical activity in the brain. Int J Psychophysiol 18:49–65.

Rosen BQ, Halgren E. 2022. An estimation of the absolute number of axons indicates that human cortical areas are sparsely connected. PLOS Biol 20:e3001575.

Rosen BQ, Halgren E. 2021. A whole-cortex probabilistic diffusion tractography connectome. eNeuro 8.

Sporns O, Tononi G, Kötter R. 2005. The human connectome: A structural description of the human brain. PLoS Comput Biol 1:0245–0251.

Trebaul L, Deman P, Tuyisenge V, Jedynak M, Hugues E, Rudrauf D, Bhattacharjee M, Tadel F, Chanteloup-Foret B, Saubat C, Reyes Mejia GC, Adam C, Nica A, Pail M, Dubeau F, Rheims S, Trébuchon A, Wang H, Liu S, Blauwblomme T, Garcés M, De Palma L, Valentin A, Metsähonkala EL, Petrescu AM, Landré E, Szurhaj W, Hirsch E, Valton L, Rocamora R, Schulze-Bonhage A, Mindruta I, Francione S, Maillard L, Taussig D, Kahane P, David O. 2018. Probabilistic functional tractography of the human cortex revisited. Neuroimage 181:414–429.

van den Heuvel MP, de Reus MA, Feldman Barrett L, Scholtens LH, Coopmans FMT, Schmidt R, Preuss TM, Rilling JK, Li L. 2015. Comparison of diffusion tractography and tract-tracing measures of connectivity strength in rhesus macaque connectome. Hum Brain Mapp 36:3064–3075.

Van Essen DC, Jbabdi S, Sotiropoulos SN, Chen C, Dikranian K, Coalson T, Harwell J, Behrens TEJ, Glasser MF. 2014. Mapping Connections in Humans and Non-Human Primates: Aspirations and Challenges for Diffusion Imaging In: Johansen-Berg H, Behrens TEJBT-DMRI (Second E, editors. Diffusion MRI: From Quantitative Measurement to in Vivo Neuroanatomy. San Diego: Academic Press. pp. 337–358.

Van Essen DC, Smith SM, Barch DM, Behrens TEJ, Yacoub E, Ugurbil K. 2013. The WU-Minn Human Connectome Project: An overview. Neuroimage 80:62–79.

von Ellenrieder N, Gotman J, Zelmann R, Rogers C, Nguyen DK, Kahane P, Dubeau F, Frauscher B. 2020. How the human brain sleeps: direct cortical recordings of normal brain activity. Ann Neurol 87:289–301.

Wipf D, Nagarajan S. 2009. A unified Bayesian framework for MEG/EEG source imaging. Neuroimage 44:947–966.

Yang AI, Wang X, Doyle WK, Halgren E, Carlson C, Belcher TL, Cash SS, Devinsky O, Thesen T. 2012. Localization of dense intracranial electrode arrays using magnetic resonance imaging. Neuroimage 63:157–165.

Zhang H, Watrous AJ, Patel A, Jacobs J. 2018. Theta and alpha oscillations are traveling waves in the human neocortex. Neuron 98:1269–1281.

CONCLUSION

The human neocortex is an organ of unrivaled complexity. When considered in totality, the research presented in this dissertation consists of a series novel quantitative estimates of cortical structural and functional connectivity. These connections enable the coordination of neural elements whose synchrony is revealed in extracranial potentials as I have both observed and generatively modeled. The description and quantification of the principles which govern endogenous, mesoscale neural communication are a foundational element of a broader understanding of the cortical function and ultimately the human mind.